UNIVERSITAT DE BARCELONA

Nanoscale Tomography Based in Electrostatic Force Microscopy

Harishankar Balakrishnan

ADVERTIMENT. La consulta d'aquesta tesi queda condicionada a l'acceptació de les següents condicions d'ús: La difusió d'aquesta tesi per mitjà del servei TDX (**www.tdx.cat**) i a través del Dipòsit Digital de la UB (**diposit.ub.edu**) ha estat autoritzada pels titulars dels drets de propietat intel·lectual únicament per a usos privats emmarcats en activitats d'investigació i docència. No s'autoritza la seva reproducció amb finalitats de lucre ni la seva difusió i posada a disposició des d'un lloc aliè al servei TDX ni al Dipòsit Digital de la UB. No s'autoritza la presentació del seu contingut en una finestra o marc aliè a TDX o al Dipòsit Digital de la UB (framing). Aquesta reserva de drets afecta tant al resum de presentació de la tesi com als seus continguts. En la utilització o cita de parts de la tesi és obligat indicar el nom de la persona autora.

ADVERTENCIA. La consulta de esta tesis queda condicionada a la aceptación de las siguientes condiciones de uso: La difusión de esta tesis por medio del servicio TDR (**www.tdx.cat**) y a través del Repositorio Digital de la UB (**diposit.ub.edu**) ha sido autorizada por los titulares de los derechos de propiedad intelectual únicamente para usos privados enmarcados en actividades de investigación y docencia. No se autoriza su reproducción con finalidades de lucro ni su difusión y puesta a disposición desde un sitio ajeno al servicio TDR o al Repositorio Digital de la UB. No se autoriza la presentación de su contenido en una ventana o marco ajeno a TDR o al Repositorio Digital de la UB (framing). Esta reserva de derechos afecta tanto al resumen de presentación de la tesis como a sus contenidos. En la utilización o cita de partes de la tesis es obligado indicar el nombre de la persona autora.

WARNING. On having consulted this thesis you're accepting the following use conditions: Spreading this thesis by the TDX (**www.tdx.cat**) service and by the UB Digital Repository (**diposit.ub.edu**) has been authorized by the titular of the intellectual property rights only for private uses placed in investigation and teaching activities. Reproduction with lucrative aims is not authorized nor its spreading and availability from a site foreign to the TDX service or to the UB Digital Repository. Introducing its content in a window or frame foreign to the TDX service or to the UB Digital Repository is not authorized (framing). Those rights affect to the presentation summary of the thesis as well as to its contents. In the using or citation of parts of the thesis it's obliged to indicate the name of the author.

Doctoral Thesis

Nanoscale Tomography Based in Electrostatic Force Microscopy

Harishankar Balakrishnan

Thesis co-supervisor : Gabriel Gomila Lluch

Thesis co-supervisor : Lazaro Rene Izquierdo Fabregas

UNIVERSITAT DE BARCELONA

Universitat de Barcelona

Facultad de Física

Departamento de ingeniería electrónica y biomédica

Nanoscale Tomography Based in Electrostatic Force Microscopy

Autor:

Harishankar Balakrishnan

B. Harishankar.

Programa de Doctorado: Nanociencias

Línea de investigación: Nanobiotecnología

Codirector y tutor de tesis: Gabriel Gomila Lluch

Codirector de tesis: Lazaro Rene Izquierdo Fabregas

UNIVERSITAT DE BARCELONA

Barcelona, 2021

"The scientific man does not aim at an immediate result.

He does not expect that his advanced ideas will be readily taken up.

His work is like that of the planter — for the future.

His duty is to lay the foundation for those who are to come and point the way.

He lives and labors and hopes."

Nikola Tesla

Acknowledgement

The undertaking of this doctoral research has been an incredible experience that I will cherish in the years to come. Past few years in this PhD have been a goldmine of curiosity, opportunity, and a constant reminder to hold the unrelenting optimism. This work is not in any way an individual effort, but a teamwork interlaced with professional and personal encouragement from people around me.

I would like to whole-heartedly thank Prof. Gabriel Gomila for providing me the opportunity to be a part of his research group. Gabriel has been an excellent teacher, one of the best I have learnt from. His pacified listening and problem-solving capability have been a treat to be experienced firsthand. The freedom provided by him, made me self-reliant and improved my intellectual standards to compete with world-class colleagues. I am fortunate to be his doctoral student and I hope I have a learnt a thing or two. Thank you, Gabriel!

After my thesis supervisor, it is befitting to thank my co-supervisor Dr. Rene Fabregas who has made mathematics fun for me again. Rene is a marvelous human being and an excellent researcher. The first years of Ph.D. under Rene's tutelage have helped me heaps and bounds to understand the numerical analyses. His calm demeanor and cheery infectious personality would be a major void in my years to come. It was an honor to be your first doctoral student and I wish many people could experience what I experienced.

Ruben has been one of the pillars of the lab and rightfully so in my PhD as well. His application-oriented solutions and inquisitive hunger has inspired me to troubleshoot things that once I never could. His grasp on understanding physics, instruments and engineering is something to be coveted and I enjoyed working with him, especially in the last few grueling months.

My partner in science, crime, and PhD, Martina Di Muzio, has always been a wonderful colleague to share this experience with. Our SPM2.0 meetings and travels were unforgettable and boisterously fun. I am happy that we got to do this PhD together and to have learnt a lot from each other. The kindness exuberated by her is only paralleled to her cognitive intelligence and powerpoint skills.

I would also like to extend my warm gratitude to Marti Checa, with whom I have countless memories right from years my first days of work. Marti's drive to achieve things is high up on the list to make him a prominent person to look up to. Thanks for taking me in and making my friends circle wider. I would be making a grave mistake if I had not thanked Dr. Adrica Kyndiah whose counsel helped me numerous times. Her perseverance, care and looking after made us all a better person by setting an example for us to follow.

I would also like to express my appreciation to Helena Lozano for her jubilant presence and teachings throughout my PhD. Our professional, personal, and philosophical discussions helped me understand and

grow as a person. I wish her my deepest wishes for the future. Also, Ricardo Hidalgo has been a big influence in the first years of my PhD, both culturally and socially. The knowledge imparted would range from music to cognitive biases. Thank you, Ricardo!

Continuing in my Nanobioelec group, I thank the senior member Annalisa Calo for the helpful scientific discussions, and it has been a pleasure knowing you in the last period of PhD. Larissa Hutter, I like your steely resolve and empathetic heart. It is the rarest combination and I wish you don't lose it. Shubham Tanwar, thanks for bringing new energy to the group and I wish you all the best.

After my research group, it is time to thank my SPM 2.0 consortium colleagues – Sarah, Oscar, Daniel, Filipe, Maria Elena, Ivan, David, Jonas, Lars, Divya, Sofia, Simone. Representing SPM2.0 ESRs have been one of the highlights of my PhD career and our bi-annual meetings were always filled with good times, if not the best. Especially the times shared with Filipe and David in my first London secondment, was unforgettable with science, banter, food, and city explorations. I would also love to thank Maria Elena for being a phenomenal host and making my time in at Imperial college worthwhile. If the chances are presented again, I will not hesitate to work with anyone mentioned above.

Joining the PhD committee was one of the good decisions I made in IBEC. Weekly meetings and organizing the PhD retreat was thoroughly exciting. Being the Master of Ceremonies (MC) of both the retreats is something close to my heart and the connections made in the committee are something to treasure. Thank you Gerard, for being one of the good friends at IBEC and hanging out with you is always entertaining to say the least.

I would like to thank my IBEC friends and colleagues who made my PhD life infinite times better. Julia, Francina, Ana, Miriam, Mireia, Patricia, Adrianna, Claudia Di Gugliemo, Claudia Navarro for transforming the ordinary times into extraordinary. Thanking my college friends Abz, Gv, Srini, Sumo also due for their constant support and encouragement.

Finally, I thank my mother and father for their immense amount of trust placed on me while instilling me with courage and confidence. It takes a lifetime to repay your deeds and I am honored to do that. Also, I would like to thank my brother, Aravind Baradwaj for teaching me everything I know, and Sri Vidya Baradwaj for the constant encouragement and support.

For all that has been, thanks; For all that will be, yes.

- Hari

Table of Contents

1 Introduction, objectives, and structure of the thesis...……………………………......1

2 Need for nanoscale subsurface characterization……………………………………...7

3 Scanning Probe Microscopy for subsurface characterization………………………13

3.1. Scanning Probe Microscopy……………………….……………………………………………13

3.2. SPM subsurface characterization techniques……………………………………………….....22

3.3. EFM for Subsurface characterization……………………………………………………….....25

4 Silver nanowire nanocomposite materials……………………………………………29

5 Materials and methods I: Numerical theoretical modelling of EFM.....…...…………35

5.1. Basics of theoretical modelling and numerical analysis……………………………………......35

5.2. Modelling of EFM applied to single buried nanowires…………………………………………….50

6 Materials and methods II: Silver nanowire gelatin nanocomposite preparation.....59

7 Spatial resolution and capacitive coupling in nanowire nanocomposites characterized by scanning dielectric microscopy ……………………………...........81

8 Depth mapping of silver nanowire nanocomposites by SDM……………………....95

9 Conclusions…………………………………………………………………………117

10 Outlook and Future works……………………………………………………………..121

11 Summary………………………………………………………………………........127

11.1 Summary : English (ENG)……………………………………………………………………………..127

11.2 Resumen : Spanish (ESP)…………………………………………………….................................130

12 Appendix……………………………………………………………………….......135

12.1 List of publications and congress presentations…………………………….................................135

12.2 List of acronyms and abbreviations…………………………………………………………………..137

13 References…………………………………………………………………….........141

Chapter 1

Introduction, Objectives and Structure of the Thesis

Introduction :

Nanoscale tomography or sub-surface nanoscale characterization is an indispensable technique to identify buried (or) dispersed objects inside a matrix. The scope of its application covers a wide range of fields including drug delivery, tissue engineering, metal and semiconductor industry, polymer technology, packaging industry, solar cell applications, and wastewater treatment, to name a few. Studying the fate of the entities buried within a bulk material can help us in understanding the basic elemental processes and properties like electron transport, mobility of ions, intracellular communication, as well as, to tune the overall physical properties of the materials or their toxicity.

For instance, if we learn about the dispersion and aggregation level of nanoparticles, in a commercially available sunscreen with nanoparticles, we could address the debate on the nanotoxicity being caused by the nanoparticles. Similarly, if we identify the dispersion patterns of nanostructures inside the three-dimensional geometry of a nanocomposite, we could steer their physical properties (electrical, optical, magnetic, thermal) to tailor our desired applications.

The demand for nanoscale tomographic characterization has given rise to the development of different techniques and methods, mainly based on Electron, X-Ray and Optical Microscopies. Each of the techniques can provide us with the sub-surface information required, but all present certain limitations. For example, Electron Microscopy methods require extensive sample preparation, and so the sample is altered or destroyed in the characterization process. Fluorescence microscopy and two-photon microscopy require a fluorescence tag or two-photon dyes to be tagged/attached to identify the dispersed particles inside the matrix/composites. For this reason, additional nanotomographic microscopy techniques are still being investigated. Among them, nanotomographic Scanning Probe Microscopy (SPM) techniques have emerged and identified to possess a great potential in the recent years.

Scanning Probe Microscopies are the family of microscopies that *scans* the sample surface using a nanometric sharp *probe* and the acquired data is used to reconstruct the surface topography with nanometric resolution. In the last three decades after its inception, there are advanced SPM techniques developed, which in addition to the sample topography, are able to provide information also on the physical properties of the

material. Few advanced SPM techniques can use this capability to probe the subsurface properties of the sample. Among them, we find Electrostatic Force Microscopy. Electrostatic Force Microscopy (EFM) is a technique where a voltage bias is applied between the cantilever probe and the sample, and thereby a capacitance is created. When the probe is moved along the surface, the cantilever deflects, due to the capacitive force, an amount determined by the electrical properties of the material localized beneath the tip. When the probe is scanned along the sample surface, the change in the capacitive force is measured and recorded, and electrical images are built. The capacitive force is a long-range force and hence it can also probe the presence of entities below the surface. This quality has been utilized to study the tomography (sub-surface characteristics) of materials. Examples include the investigation of compositional modifications below some organic layers or imaging of carbon nanotubes, graphene networks and nanoparticles inside polymeric nanocomposites. Along with the qualitative analysis of the EFM images, recent advances proved that quantitative nanotomographic information could be obtained such as the depth of carbon nanotubes in polymeric films or the dielectric properties of water in buried nanochannels.

A field where there is a special need in the development of nanotomographic methods is the field of nanowire-based nanocomposite materials for electronic applications. Among them, silver nanowire nanocomposites play a central role. Silver nanowire nanocomposites have a barrage of applications to their credit ranging from solar cell applications, touch screens, LEDs to flexible wearable devices. Understanding the tomography of these nanocomposites could aid one in tuning them for our desired applications.

Objectives :

The overall objective of this work of thesis is to expand the capabilities of electrostatic force microscopy (EFM) as sub-surface imaging technique able to provide tomographic information on nanocomposite materials with nanoscale spatial resolution, with a special focus on the case of nanowire-based nanocomposites. Initially, we aim at determining the factors influencing the EFM signal in nanotomography studies on nanowire-based nanocomposites theoretically, studying both instrumental factors like the probe geometrical parameters and sample factors, like the dielectric constant and thickness of the burying matrix, or the geometry of the buried nanowires. To achieve it, we aim at developing advanced numerical models to mimic the experimental systems, including models with multiple nanowires, to explore aspects such as the spatial resolution or the electric interaction between nanowires. An additional objective of this study is to provide us with the best possible parameter combinations to address the experimental studies. Secondly, we aim at demonstrating the possibility to obtain nanotomographic information on

nanowire-based nanocomposites by means of EFM experimentally. In particular, we aim at demonstrating that the depth distribution of the nanowires in the nanocomposites can be obtained, in a non-destructive way, by combining EFM measurements with finite element numerical calculations.

To address our objectives, this work of thesis has been **structured** in the following chapters.

Chapter 2 further outlines the importance and the need for the nanoscale sub-surface characterization of materials with its dire necessity in a wide range of fields.

Chapter 3 introduces the family of Scanning Probe Microscopies by explaining their components, principles, and modes of operation with special importance provided to Electrostatic Force Microscopy. This chapter also covers the previous experiences of SPMs in sub-surface characterization, and specifically a section is dedicated to the successes of EFM in doing so.

Chapter 4 deals with the introduction of silver nanowire nanocomposite materials and their successful existing applications. This chapter also details the importance of extending beyond the surface barrier to advance in the development of these materials.

Chapter 5, our first materials and methods chapter, describes the theoretical framework used to interpret the sub-surface EFM images. *Section 5.1* explains the basics of theoretical models and numerical analysis required for the computational EFM modeling studies. This part is filled with introductory studies of finite element numerical analyses in the construction of primitive models. *Section 5.2*, advances in trudging to our object of interest, includes the analysis pertaining to a single metallic nanowire buried in a dielectric matrix. This study is carried out with special attention provided to the parameters that influence their signals thereby impacting the EFM contrast.

Chapter 6, our second materials and methods chapter, consists of the preparation of experimental gelatin-silver nanowire nanocomposites and the achievement of nanometric thicknesses suitable for efficient subsurface studies with EFM in the *section 6.1***.** In the *section 6.2*, characterization of the prepared nanoscale subsurface sample with AFM and SEM is shown. Along with the results of this chapter, an appendix contains a literature survey of subsurface sample preparation methods.

Chapter 7 contains the advanced numerical analysis part required for the nanotomographic studies on nanowire nanocomposite materials. There is a particular focus on the attainable spatial resolution subsurface and the possibility to identify the capacitive coupling between neighboring nanowires.

Chapter 8 deals with the sub-surface experimental analysis of nanocomposites using Scanning Dielectric Microscopy (SDM), the quantitative version of EFM. This chapter contains the EFM imaging of the nanocomposite sample and various analytical and numerical models used in the parameter extraction. Here, we show that Scanning Dielectric Microscopy (SDM) can image the nanowires buried in the gelatin matrix and map the depth distribution of the nanowires within the nanocomposite in a non-destructive way. The results also show that SDM can optimize these materials' properties for applications in fields such as wearable electronics, solar cell technologies, or printable electronics and can be a valuable non-destructive subsurface characterization technique for nanowire-based nanocomposite materials.

Chapter 9 summarizes our nanoscale tomography studies followed by the prospective future studies arising from this thesis and a scientific outlook on the existing research questions in **Chapter 10.**

Chapter 11 contains the summary of our thesis condensing our studies, wherein part *11.1* contains the summary in English followed by *resumen* in *11.2* in Spanish.

Chapter 12 contains the appendix with the dissemination of results attained from this thesis in publications, congress seminars and poster presentations. This chapter also contains abbreviations for acronyms for the ease of our readers.

Chapter 13 is composed of the bibliography used as our references during the experimental and writing part of this thesis.

Chapter 2

Need for nanoscale subsurface characterization

This chapter outlines the necessity of subsurface characterization in a wide range of fields from material sciences to biological sciences. The need for the tomographic studies has been explained with the help of examples, specifically in the fields of material sciences and technology, biological and medical sciences, and nanocomposites.

The study of the uppermost layer of a material with its surface features and characteristics are generally known as topography. The investigations beneath that exposed surface, in some cases extending to the whole material, is termed as tomography. Investigating the tomography or sub-surface would not only help us in understanding the three-dimensional structural aspects like the position of nanoscale objects in the geometry of the bulk volume, but also to aid us in tuning the functional properties of the material such as dielectric constant, conductivity, magnetic susceptibility and electric percolation levels[1]. Tomography investigation, especially nanoscale tomography, is complicated in investigational studies owing to the limited amount of imaging techniques available.

Despite the limitations in studying them, sub-surface characterizations have been an integral component in nanoelectronics, dielectrics, semiconductor fabrication, material science, thin-film technology, nanocomposites, and biological and medical sciences. Verbiest et.al.[2] noted that the ongoing process in the above-mentioned fields, has an increased demand to study the subsurface in a non-destructive way, thereby pushing the boundary in increasing the resolution. Depth-resolved information and three-dimensional sample analysis and reconstruction with nanoscale spatial resolution have been a farfetched goal that would benefit humungous research fields.

Some of the fields where the nanoscale subsurface characterization is predominantly necessary are:

Materials science and technology:

Nanoelectronics and the semiconductor industry are few of the top contenders to view the nanostructures beneath the surface[3]. Back in 1994, Yamanaka and Ogiso[4] stated that there is an increasing need to study the mechanical and electrical properties of devices down to the nanometric level. This may include sub-surface features which does not limit to lattice defects, groups of ions, clusters, and crystal gains.

It has been predicted that subsurface characterization would help in characterizing three-dimensional Integrated Circuits (ICs) and in back end of the line (BEOL)[5] Integrated circuit processes to understand the methodology and nano-electronics metrology[6].

Integrated circuits and silicon-based quantum devices are intended to contain nanostructures at precise geometrical positions. Gramse et.al.[7] claimed that "a technique capable of non-destructive, nanoscale measurements including quantitative electrical characterization would be valuable for both IC failure analysis and creation of quantum architectures". It is also known that the integrity of ICs is compromised when local dopant profiling is changed, thus resulting in implications of quality control. Integrated Semiconductor devices like transistors and sensors would also benefit from subsurface research[8]. Analysis of highly complex three-dimensional integration of transistors and their intercalated nanostructures is necessary for semiconductor fabrication lines[9].

Energy science research also requires subsurface studies to analyze their photovoltaic devices, supercapacitors, and batteries. Materials and alloys would also be a huge beneficiary for the tomography investigation as some rely on both deliberate particle inclusion for strengthening and, also for grain boundary embrittlement as weakening purposes[10,11]. In order to optimize their performance, catalytic industries require three-dimensional pore structure data with destruction and adhesion sites for active particles[12]. Few earlier studies like Pt and Au nanostructures inside a polymer matrix have been studied to provide feedback on catalyst fabrication design[13,14].

Nanocomposites:

The addition of nanostructures to an existing bulk material, can positively influence its physical and chemical properties, which is the underlying principle in the birth of nanocomposites.

For instance, polymer nanocomposites (polymer films with nanostructures in their matrix) have played a huge part in recent years in the field of electronics, material science, aviation, and transport industries[15]. Carbon Nanotubes (CNT) are widely used to improve the mechanical, thermal, optical, and electronic properties of polymer nanocomposites[15]. CNT nanocomposites were found to increase the thermal conductivity up to 70% [16]. CNTs in polymeric films were proved to increase their performance in thin-film technology[17]. Moreover, nanoparticle dispersion in nanocomposites is critical in determining its resultant properties such as mechanical, electrical along with transport of material properties[1].

Metallic nanowire nanocomposites have been widely used due to their influence in enhanced physical properties that the nanostructures provide to the polymer matrices. Silver nanowire nanocomposites (SNN) are widely used due to the simple fact that adding few percentages per weight would retain the properties of the polymer and help in the birth of new properties (e.g., electrical conductivity). Recently, SNNs are found in plenty of applications ranging from solar cell applications to touch screens (more about SNN in chapter 4).

Sub-surface characterization of these nanocomposites would assist in understanding their properties and functionality thereby elevating us to the position of influencing those properties. Aside from nanocomposites, heterogenous nanoparticles like multiphase nanoparticles and core-shell nanoparticles would require chemical mapping characterization for their applications[12].

Biological and Medical sciences:

In biology, the fundamental understanding between the cell structure and function is provided by imaging the structure of the cell[18]. There have been frequent calls for sub-surface imaging in cells to understand its functionality non-invasively. With every new instrumentational advance, newer undiscovered cellular features are identified. Breaking the barrier in tomographic analysis of cells, tissues, and extending to the whole organ and subsequently reconstructing them, would be the undeniable objective of the next decade. There have been few preliminary studies to map the subsurface at the cellular level[19–22]. Shekhawat et. al. have attempted to capture the subsurface features of cell including the nucleus using Scanning Near-Field Ultrasound Holography[23]. Recently, Garcia et.al investigated the mapping of sub-surface features with force microscopy based on stiffness measurements[24].

On the other hand, nanoparticle and nanomaterials have been used in the field of nanomedicine to aid in the research of cancer biology, tissue engineering and bio-engineering applications[25]. Sub-surface characterization would not only help in studying drug-delivery profiles and techniques, but also in investigating its toxicity in cells, tissues and surrounding extra cellular matrices[26]. The fate of a nanoparticle is decided by the amount of time it is actively present on the target region before it is cleared. With the help of sub-surface characterization techniques, it is possible to calculate the fate and uptake of nanoparticles in a healthy or cancerous target area. For instance, Tetard et al, have studied the effects of silica nanoparticles in mouse cells[26].

On the other hand, there is a growing debate about the local or global toxicity caused by nanoparticles used in cosmetic applications, like sunscreens[27]. The subsurface tools to study them in their native matrix are limited thereby denying our understanding to address the presence or absence of nanoparticle infiltration into skin layers. As the advent and applications of nanomedicine increases, the secondary effects of these treatment practices should be well-studied and cataloged. Sub-surface characterization can also help in this regard as it is a non-invasive technique and offers the possibility to image in its native biological medium.

These examples mentioned above are not an exhaustive list, but a small percentage of prospective fields where the known and recognized nanoscale sub-surface problems have been highlighted. These examples show us the integral need for nanoscale subsurface characterization in basic science and also in applied research. As we advance with our material, semiconductor, and biological research to the next decade, nanoscale subsurface characterization would be the order of the day and undeniably beneficial.

Chapter 3

Scanning Probe Microscopy for subsurface characterization

This chapter briefly explains the concept of scanning probe microscopes with special attention provided to Atomic Force Microscopy (AFM) and Electrostatic Force Microscopy (EFM). Chapter 3.1 discusses the working principles of AFM and EFM. Chapter 3.2 notes the use of SPMs in subsurface characterization with examples and discusses its advantages. Chapter 3.3 explains the advent of EFM in subsurface characterization and its applications in various samples.

3.1 Scanning Probe Microscopy

Scanning Probe Microscopes (SPM) constitutes a family of microscopy techniques that uses a probe to *sense* the sample with nanoscale spatial resolution. The first member of the SPM family was Scanning Tunnelling Microscopy[28], which was widely acclaimed and garnered the shared Nobel prize for its inventors Gerd Binning and Heinrich Rohrer in 1986. STM works by scanning a sharp metallic probe over the surface of a sample while recording the tunnelling current between tip and sample, thereby conferring the capability to study the material surface to the atomic level (Fig 3.1).

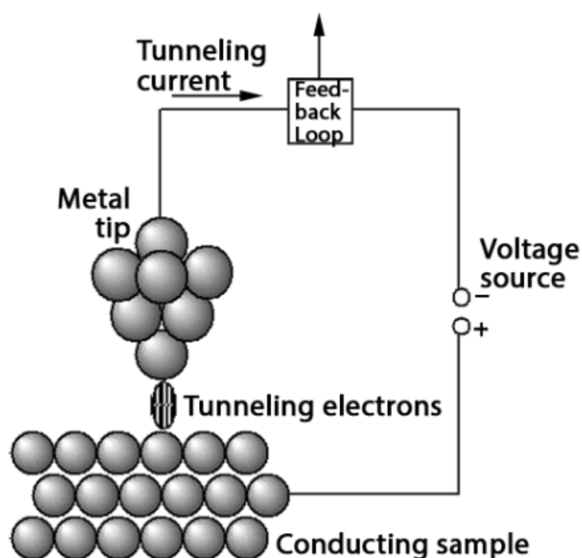

Fig 3.1. Scanning Tunnelling Microscopy with its electron tunnelling and the feedback loop (Image obtained from Nanoscience instruments webpage - https://www.nanoscience.com/techniques/scanning-tunneling-microscopy). STM works by recording the tunnelling current between tip and sample enables to study the surface to the atomic level.

Atomic Force Microscopy (AFM)[29] was released in the same year 1986, and overcame the limitation of STM to be only applicable to conductor or semiconductor materials.

Atomic Force Microscopy works by the same principle of scanning the surface of interest with the help of a nanometric probe, but this time the interaction force between tip and sample is measured. The probe consists of a cantilever with the sharp tip present at its end. Generally, the cantilever is a micrometric thin triangular or rectangular beam with the recent ones having a reflective coating on its upper surface. The interaction force of the tip with the surface is sensed with the help of a laser beam incident on the reflective part of the cantilever at the probe end, which measures the cantilever bending by using a four-quadrant photodiode upon which the reflected laser beam falls on. The probe is raster scanned along the surface by means of a piezoelectric X-Y scanner and moved up and down by means of a third piezoelectric Z scanner. A feedback loop controls the Z elongation ensuring a constant cantilever deflection (or other physical observables, depending on the imaging mode) during the scan. The variation in the Z elongation of the scanner at each position constitutes the topographic image. Ideally, an AFM measurement begins with the laser being deflected from the probe/cantilever to the intersection centre of the four-quadrant photodiode. When the tip moves as it interacts with the surface, the laser signal in the photodiode shifts. This incident signal is then used to regulate the feedback loop and act on the piezo elongation to restore the position of the laser beam on the photodiode. Using this information, the topographical map of the surface with unparalleled nanometric lateral and vertical resolution is obtained (Fig 3.2). AFM can be used for both conductive and dielectric sample, since the measured physical magnitude is the tip-sample interaction force instead of an electric current. For the same reason, it can also be operated in different environments (vacuum, air, or liquid).

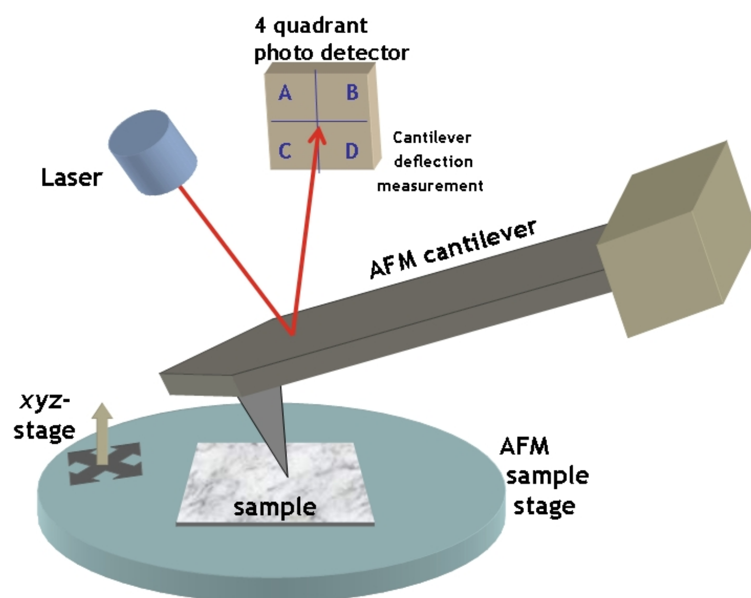

Figure 3.2. Schematic Atomic Force Microscopy setup with the essential components of cantilever/probe, laser and photodetector (Image adapted from [30]). The XYZ sample stage enables coarse movements of the sample with respect to the tip, for easier identification of the object of interest. When the tip moves as it interacts with the sample or vice versa, the laser signal in the photodiode shifts. This incident signal is then used to feed the feedback loop and act on the piezo elongation to restore the position of the laser beam on the photodiode, from where the topographical map of the surface with nanometric lateral resolution is obtained.

The atomic force microscope works in different modes, as shown in Fig 3.3, depending on our necessity. For example, i) contact mode, where the tip moves with a certain fixed deflection, ii) dynamic amplitude modulation, where the tip oscillates with a specific frequency f and amplitude A. When the oscillation amplitude is large the tip can tap the surface at the end of the oscillation cycle, and the mode is known as tapping mode or intermittent contact mode. When the oscillation amplitude is very small, this does not happen, and the mode is referred to as non-contact mode. These modes, in turn, depend upon the setpoint, which is a user defined value of the deflection or amplitude that the height feedback maintains during contact or tapping mode imaging (in the case of non-contact mode feedback is often made on the dephasing of the oscillation, due to the very small amplitudes involved). The change in deflection (contact mode) and the change in the amplitude of oscillation of the cantilever (tapping or non-contact mode) during the scan is used to control the feedback loop and enable the reconstruction of the surface topography.

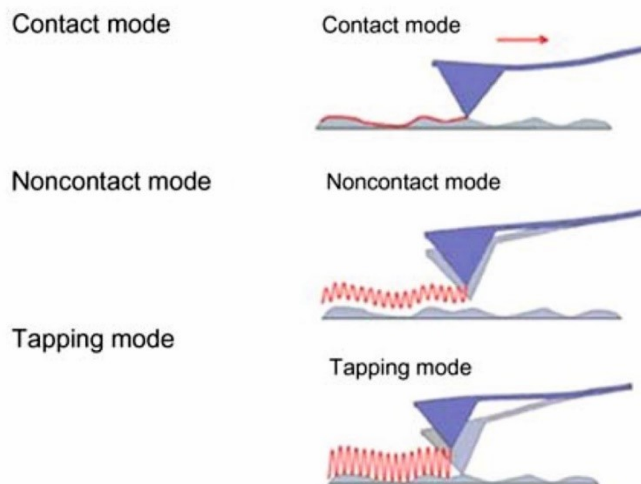

Figure 3.3. Different modes of AFM imaging : Contact mode, Non-contact mode and Intermittent contact mode [also known as Tapping mode] (Image from [30]). The change in deflection (contact mode) and the change in the amplitude of oscillation (or of the phase) of the cantilever (tapping or non-contact mode) during the scan is used to control the feedback loop and enable the reconstruction of the surface topography.

An example of an AFM topographic image obtained in contact mode corresponding to a SiO_2 pillar on a highly doped silicon substrate is shown in Fig 3.4. From the topographical profile extracted from the image, one can extract the height of the pillar with excellent precision (in this case, ~110 nm).

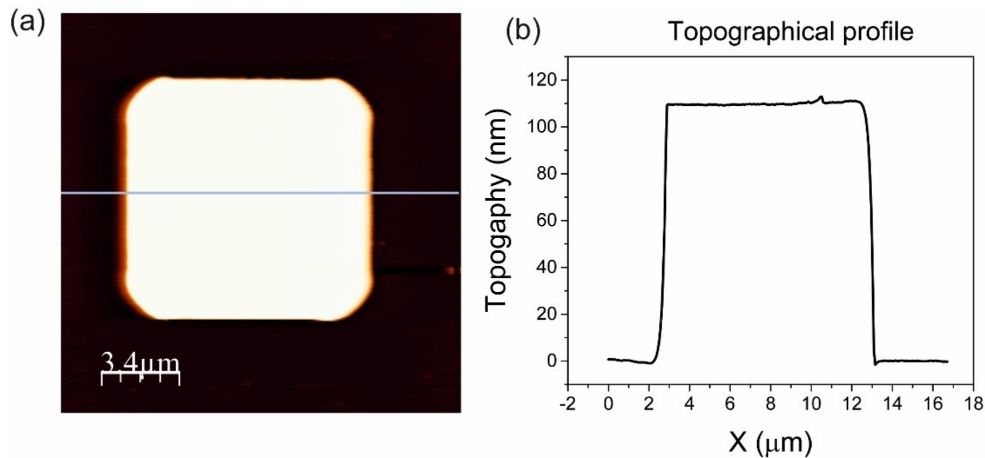

Figure 3.4. (a) AFM image of a SiO_2 pillar on a highly doped silicon substrate imaged with the help of EasyScan 2 Atomic Force Microscope (Nanosurf) (b) The corresponding topographic profile along the light blue line depicted in (a)

The force acting on the probe depends on the probe-sample distance. When the probe is far from the sample surface, there is no force acting on the probe and so there is no change in the laser deflection. Moving closer to the surface of the sample, the probe is influenced by an attractive force (e.g., van der Waals force) that makes the cantilever bend downwards with respect to the surface. When the probe/tip touches the sample, the repulsive forces enter into play, and the cantilever starts reducing its overall bending. Upon further approach to the surface the probe starts to bend upwards, due to the repulsive force experienced by it. Retraction of this cantilever causes the opposite effect, as the cantilever starts to bend inward due to the attractive force experienced by it. The initial cantilever state is obtained when the probe is retracted far away from the sample. A plot of the cantilever deflection versus piezo displacement is termed as approach/retraction curve (as visualized in Fig 3.5) and it can contain information also on the physical properties of the material such as mechanical properties or tip-sample adhesion.

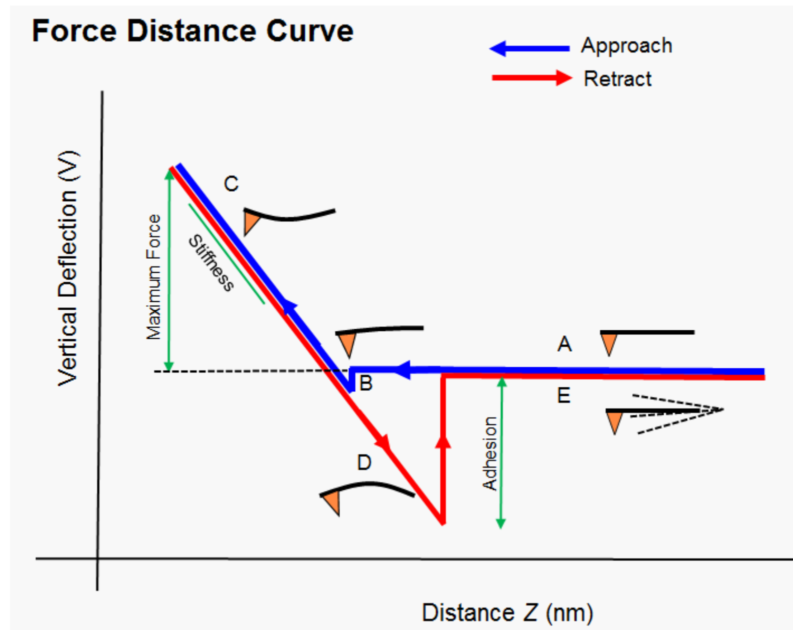

Fig 3.5. Schematic representation of a force-distance curve (Image obtained from Anton Paar instruments webpage) with the approach (blue) and retraction (red) curve of the probe showing the vertical deflection with respect to the piezo elongation distance(z). When the probe is far from the sample surface, there is no force acting on the probe and so there is no change in the vertical deflection and the probe remains in its initial state. When the probe moves closer to the surface of the sample, the probe is influenced by an attractive force) that makes the cantilever bend downwards. After the probe touches the sample, the repulsive forces enter into play, and the cantilever starts reducing its overall bending. Upon further approach to the surface the probe starts to bend upwards, due to the repulsive force experienced by it. Retraction of this cantilever causes the opposite effect, as the cantilever starts to bend inward due to the attractive force experienced by it. The initial cantilever state is obtained when the probe is retracted far away from the sample.

The advantage of AFM based instruments is that unique sample properties like conductive, magnetic, and electric characteristics can be also measured, by using suitable cantilever materials and additional instrumentation. So, maps of the physical properties like mechanical, thermal, electrical, chemical, and magnetic properties can be built along with the normal AFM topography. For instance, in the field of biology, over the years, numerous AFM inventions have been reported (Fig 3.6), able to address the chemical properties, the biological interactions or the mechanical properties at the nanoscale.

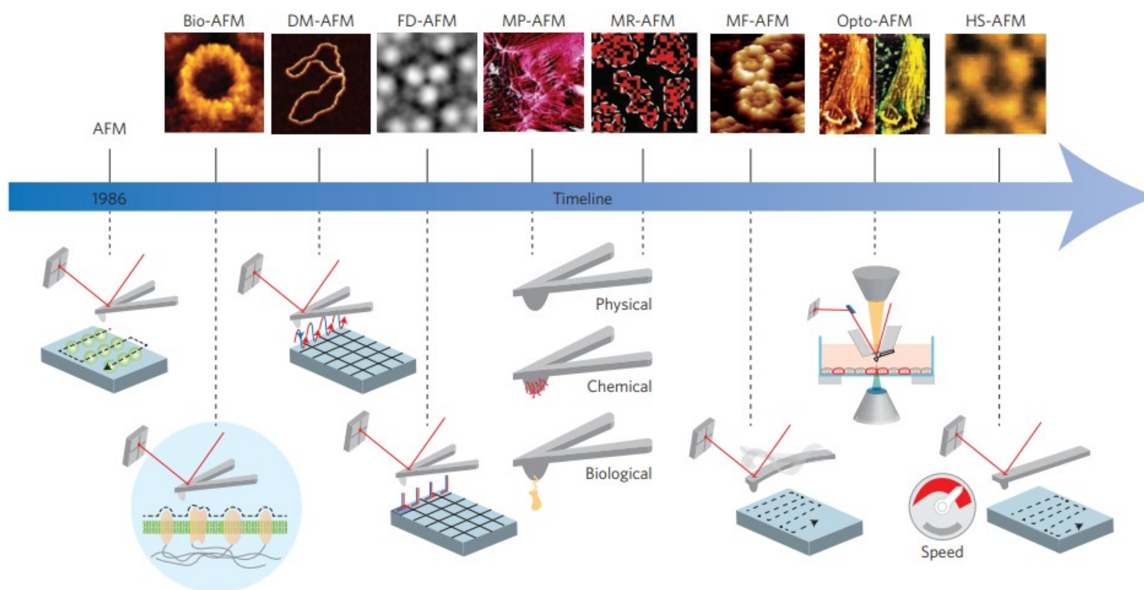

Fig 3.6. Advances in Scanning Probe microscopy over the years and their application abilities in biological sciences.
(Adapted from [31])

Electrostatic Force Microscope (EFM) is an electrical mode of AFM, where a voltage is applied between the probe and sample generating an electrostatic force between them which depends (among others) on the local dielectric properties of the sample. Normally EFM is used in two pass mode, where in a first pass the AFM topography is recorded (with no potential applied), while in a second pass the tip is lifted a certain distance, the voltage is applied, and the electrostatic force is recorded off-feedback through the cantilever deflection. An example of the same pillar used in Fig 3.4 for AFM measurements can be seen here in EFM measurement with its cantilever electric deflection profile in Fig 3.7.

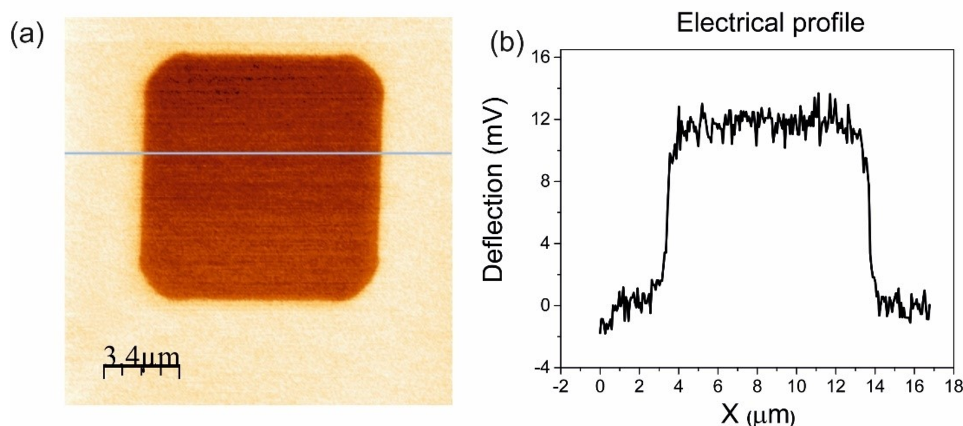

Fig 3.7. (a) Constant height DC-EFM image of a SiO_2 pillar on a highly doped silicon substrate at 5 V and at 150 nm distance from the substrate similar to the topography image in Fig 3.4. (b) The electrical deflection profile at the line depicted in the electrical image.

There are two different modes of working with EFM, DC-EFM[32] and AC-EFM, depending on whether the voltage applied is a dc or an ac voltage. Normally AC-EFM is most common as the signal to noise ratio is better. Among AC-EFM, two different detection schemes can be applied:

a) Amplitude modulation electrostatic force microscopy - AM-EFM[33–35]

b) Frequency modulation electrostatic force microscopy - FM-EFM[36]

Amplitude modulation is used throughout this thesis owing to its easier implementation and operation. In this mode, an alternating potential with frequency ω and amplitude V_{ac}

$$V = V_{dc} + V_{ac}\sin(\omega t) \tag{3.1}$$

is applied between the conductive probe and the conductive substrate (for generality we also included a dc potential used in some applications, like Kelvin Probe Force Microscopy). Thus, when the voltage is applied, an electric force acts in the tip. Due to the quadratic dependence of the electric force on the applied voltage, three distinctive force harmonics appear:

1) A static force, F_{dc}

$$F_{dc}(z) = -\frac{1}{2}\frac{\partial C_T(z)}{\partial z}\left[\frac{1}{2}V_{ac}^2 + \left(V_{dc} - V_{sp}\right)^2\right] \tag{3.1}$$

2) An oscillating force at the first harmonic of the applied frequency F_{ω}

$$F_{\omega}(z) = -\frac{\partial C_T(z)}{\partial z}\left(V_{dc} - V_{sp}\right)V_{ac}\sin(\omega t) \tag{2.3}$$

3) An oscillating force at double of the applied frequency $F_{2\omega}$:

$$F_{2\omega}(z) = \frac{1}{4}\frac{\partial C_T(z)}{\partial z}V_{ac}^2\cos(2\omega t) \tag{3.4}$$

Here, $\partial C_T(z)/\partial z$ is the derivative of the capacitance with respect to the vertical direction, referred to as capacitance gradient. Of the three harmonics, $F_{2\omega}$ depends solely on the tip-sample capacitance gradient, and therefore it can be used as a quantitative measure to evaluate the dielectric properties of the sample (e.g., its dielectric constant, ε_r).

In practical implementations, a lock-in amplifier applies the ac-voltage at frequency ω (much lower than the mechanical resonance frequency of the cantilever) to the tip and tracks the cantilever oscillation at the second harmonic ($A(2\omega)$) of the excitation frequency. The advantage of using the lock-in amplifier is that it can separate the different frequency contributions from the total collected signal easily. Calibrating the spring constant (k) of the cantilever, and measuring $A(2\omega)$, the capacitance gradient (dC/dz) can be obtained (using Eq 3.4), paving the way to gather the local dielectric information.

Scanning Dielectric Microscopy (SDM) is the technique involving the combination of the experimental EFM results with numerical and theoretical models to retrieve the local dielectric properties of the material. This technique has been used in the thesis and can be seen in further chapters.

Also , Scanning Dielectric Force Volume Microscopy (SDFVM) is an EFM mode devised recently[37] which allows to obtain deflection and oscillation amplitude EFM approach curves at every single pixel of the image simultaneously. It is based in the classic force-volume approach, where a full approach and retraction curve is measured at each pixel (Fig 3.8(a)). Fig. 3.8(b) shows an example of deflection and oscillation amplitude EFM approach curves acquired at the same time. The deflection curve can be used to build the sample topography, like in conventional force volume AFM imaging, while the oscillation amplitude curves can be used to extract the local dielectric properties of the sample at each pixel. The voluminous multidimensional data set obtained provides us with the full information set needed to study topography and dielectric constant simultaneously in a reasonable time. For example, an image with 128x128 pixels provides us with 16,384 curves of both mechanical and electrical curves (as seen in Fig 3.8 (c-d)) in less than 40 minutes.

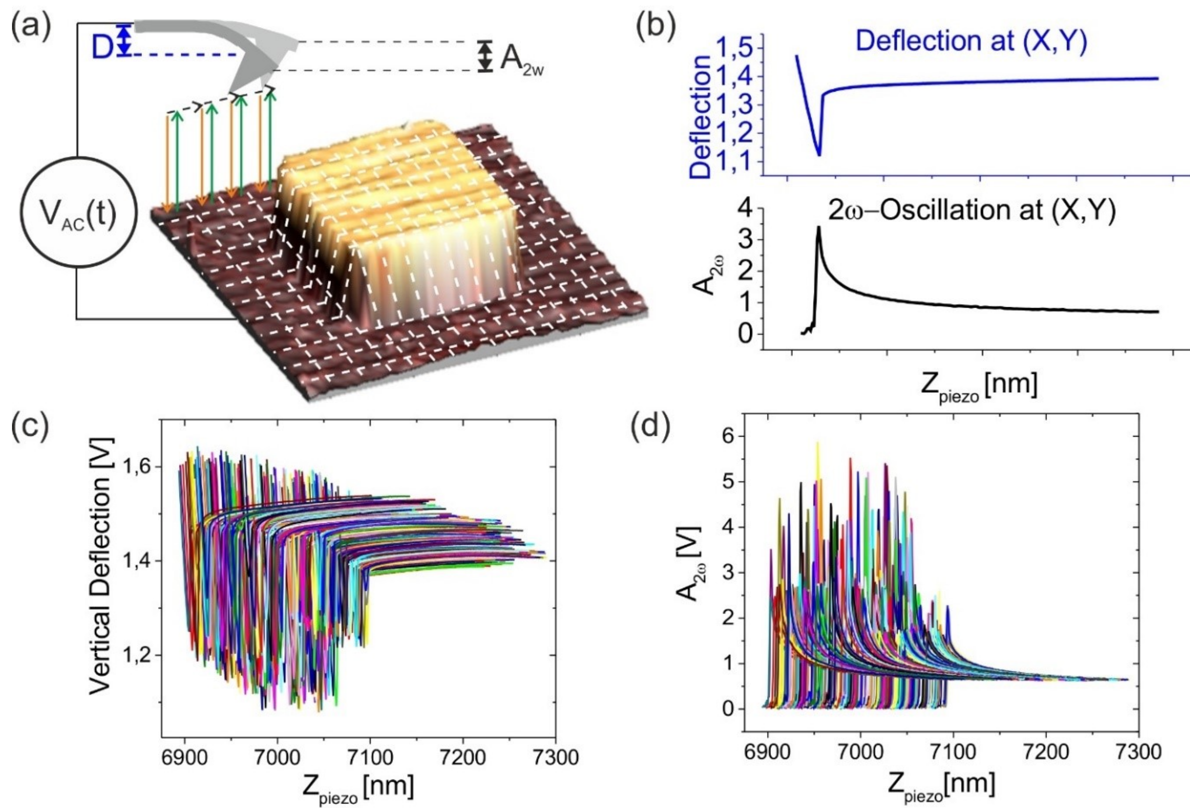

Fig 3.8. (a) Schematics of Scanning Dielectric Force Volume Microscopy (SDFM) setup developed recently in our group. Both the vertical deflection and A(2w) oscillation curves (shown in (b)) are measured in each pixel of the image. An image of 128 x 128 pixels would have 16384 vertical deflection and A(2w) oscillation curves as shown in (c-d) and would provide us with an full data set needed for dielectric characterization.(Obtained with permission from Checa et.al.[37])

This thesis uses the concept of EFM and of SDFVM to implement nanotomography methods as it is further touched upon in *Chapter 3.3*.

3. 2 SPM subsurface characterization techniques

As noted in Chapter 2, the uses and applications of subsurface SPM characterization has a great range of applications right from tracking electron transfer at atomic level to investigating macromolecular vesicles in living cells. Prior to SPM methods, optical and Electron Microscopy (EM) methods were used for these types of research. However, these techniques possess their own set of limitations. For example, conventional optical microscopy is dependent on diffraction which limits the spatial resolution with respect to the wavelength of the light used (in the visible range, typically in ~500 nm). Electron Microscopy (EM: SEM, TEM), even if still limited by diffraction and other factors, enables higher spatial resolution by using electrons as waves, which have a much smaller wavelength (>1 nm). However, the sample gets damaged both during sample preparation and imaging procedures, specifically for soft and insulating materials, and particularly in life sciences. These demerits leave us in want of alternative techniques for nanoscale subsurface characterization[38].

SPM methods are used in subsurface nanoscale characterization, due to their exceptional ability to probe magnitudes with long-range information. Since the measurements can be carried out in soft and rigid samples, conducting, and insulating and in a variety of environmental conditions, tomography based on SPMs is becoming a good contender. The advantages of SPMs in subsurface characterization would include.

- It is a non-invasive and non-destructive technique,
- The samples do not necessarily include elaborate/time-consuming sample preparation,
- The sample does not require to be sliced, milled, or processed,
- The measurements can also be extended to biologically alive samples like cells, tissues etc.
- They could be carried out in water media or any other physiological environment,
- Measurements can be carried out in any type of environment: inert, ambient, vacuum etc.
- During imaging, the sample also could be used to image dynamic processes, which include the transports, motion, or diffusion paths in real-time.

Different types of Scanning Probe Microscopies have been used in tomographic studies. Apart from Electrostatic Force Microscopy (EFM) which would be covered in the succeeding portion of this chapter *(Section 3.3),* other SPMs are covered in this part.

Ultrasonic waves can be used to explore the bulk volume of a sample and provide the tomography information. Acoustic excitation combined with near-field detection proved to be a good source in obtaining subsurface data[4]. Using this method, various nanoscale and microscale studies have been carried out to investigate subsurface contaminations[23], defects below the surface[39,40], cracks or gaps[23,41,42], to study the structures below the surface[26,43,44] and any other compliant or stiff material in the below the surface[13,45–49]. Heterodyne is the term for the frequency that combines or mixes two frequencies. Scanning Near-Field Ultrasound holography, which relays the above idea with the ultrasound frequency was also used to detect nanoparticles in polymer matrix[23,50] (shown here in Fig 3.9(I)) and also in macrophages[44].

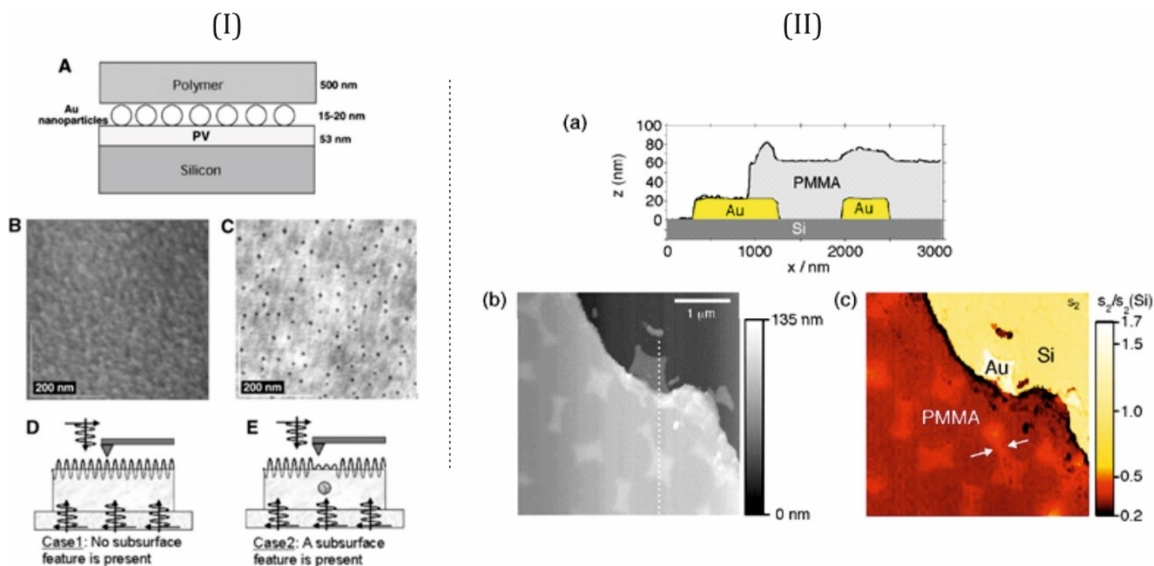

Figure 3.9. (I) An example of subsurface characterization using Scanning near-field ultrasound holography (SNFUH) applied to find the gold nanoparticles in the polymer nanocomposites. The difference can be seen in B and C of the image compares sample with and without subsurface features, respectively. (II) Near-field Scanning Optical Microscopy have also been used in subsurface investigations as seen by the characterization of gold (Au) islands under polymer (PMMA) matrix. In the image C, we can see the Au islands under dark PMMA layer [Obtained with permission from G.S. Shekhawat et.al.[23] and from Taubner. et.al.[51]]

The multimodal frequency AFM (MF-AFM) has also branched into subsurface detection with several bimodal and trimodal frequency methods. In the Bimodal AFM technique, the first mode collects the topographical information and the further mode obtains the nanomechanical information. Bimodal AFM technique were used to characterize iron oxide nanoparticles[52] and to image the amorphous and crystalline regions in polymers[53]. Trimodal AFM, a recent technique developed to acquire topography, phase and frequency shift information simultaneously, was able to image the silver nanowire buried beneath PDMS[52] and also glass nanoparticles buried under thin polymer films[54]. Mode-synthesizing AFM (MSAFM) which

combines all the multi-frequency signals into unified notations have also had some success in sub-surface characterization[55–58].

Scanning Microwave Microscopy (SMM) also uses electrical properties like the Electrostatic Force Microscopy (EFM) whereby the difference between them is a microwave sent and reflected back provides the information. SMM has been used in numerous subsurface applications like finding the metal lines in dielectrics[5], different chemical compositions[59], defects[60], and biological systems such as bacteria[61]. Scanning Near-field Optical Microscopy (SNOM) has also been used to view beneath the transparent layers using visible or mid infrared wavelength and was able to image the gold (Au) islands under PMMA layer[51] (Fig 3.9(II)). Further examples of subsurface imaging using EFM is covered in the succeeding subsection.

3.3 EFM for subsurface characterization

Electrostatic Force Microscopy (EFM), among the different SPM sub-surface techniques, have had plenty of developments out in recent years, thus supporting its candidacy to become a widely used subsurface nanocharacterization technique. The long-range electrostatic force between the tip and the sample extends to the subsurface of the sample, from where sub-surface information can be extracted. Experimental approaches combined with analytical and numerical simulations have provided the necessary progress for the EFM in nanotomography studies. EFM, in turn, has already been applied to a wide range of studies and investigations and the prominent ones that are related to our thesis are mentioned below.

Nanocomposites (NCs) turned out to be the prime benefactor of EFM in subsurface characterization since the technique is non-destructive and provide 3-dimensional information of the bulk matrix with relatively better nanometric resolution than existing techniques. Nanocomposites are widely used in a broad range of applications in the last few years (more about them in chapter 4).

Jespersen et al[62] have studied the mapping of carbon nanotubes in a polymethylmethacrylate – carbon nanotube (PMMA-SWCNT) matrix with the help of EFM. Zhao et. al.[17] have also mapped single-walled carbon nanotube (SWCNTs) in a polyimide nanocomposite thin film. These PI-SWCNTs were studied again using EFM in the work of Cadena et al.[15] . These films were also studied in Castenada-Uribe et. al.[63] using second harmonic KPFM which is functionally identical to EFM. The polymer nanocomposites have also been studied with EFM with Polystyrene-Graphene composite studied by Alekseev et al[64] to observe the graphene networks inside the composite and PVDF-CNT composite was researched by S. Patel et. al [65] to image the latex-carbon nanotube composite. Nanoparticles in the polymer matrix have also been studied by Peng et al[66] for the local dielectric property detection in the interface of TiO_2 nanoparticles-polyethylene matrix for nanodielectrics applications and resonance enhanced subsurface detection by Cadena at al[67].

Our *Nanoscale Bioelectrical Characterization group* at IBEC possesses prior experience in characterization beneath the surface with the help of EFM. In L. Fumagalli et al in 2012[33], the presence and absence of DNA inside a virus particle, provided the first quantitative measurement of the dielectric constant (ε_r) of DNA (Fig 3.10(I)). In the 2015 work published in ACS Nano by van der Hofstad et al.[68], the presence of relative humidity in bacterial cells has been identified by electrical measurements, which may have provided the solution to how the bacterial endospores survive in the extreme conditions. In the recent

collaborative effort with Dr. L. Fumagalli at Manchester University[69], the confined water in nanochannels has been identified to possess different dielectric properties than the bulk water, thus opening the doors in understanding the trapped water systems (Fig 3.10(II)).

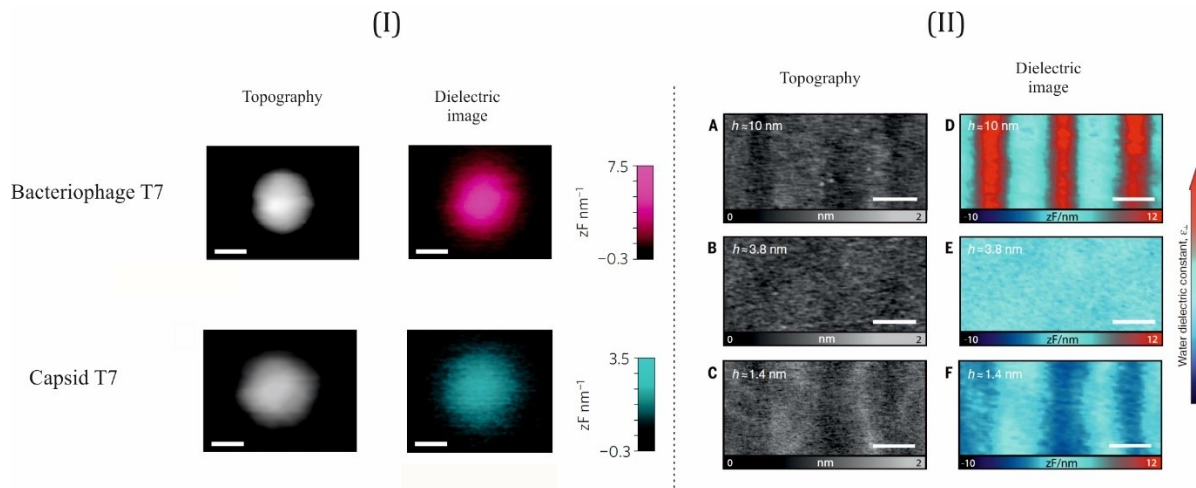

Figure 3.10 (I) The electrical images of viruses with and without the presence of DNA (top and bottom respectively) have been imaged and can be differentiated with the help of EFM (dielectric images). (II) In the nanochannels, confined water has been found to exhibit different electrical properties than bulk water. This can be seen from the topography images on the left with minimal or no difference and the dielectric images on the right show the varied ε_r of water buried in nanochannels for different channel thicknesses [Obtained with permission from Refs. [33] and [69]]

In these earlier studies, the nanotomographic information sought was the dielectric constant of materials buried below the surface, rather than its position (that was known beforehand). Dielectric constant (or) relative permittivity (ε_r) is an intrinsic response of any material to an applied electric field. This property also depends on the composition, phase, and structure of materials. ε_r is an unique number pertaining to the electrical property of the material, that provides the material fingerprint [33]. This property could be immensely useful in subsurface characterization and the exploration of EFM in subsurface characterization.

The combination of Electrostatic Force Microscopy with quantitative theoretical analysis to obtain the dielectric constant is grouped into the technique called Scanning Dielectric Microscopy (SDM). SDM has been widely applied in the research group to find the dielectric constant of not only buried objects but also of singe bacteria[35,68], viruses[33,70], DNA[70] and ultrathin thin nanometric layers[71,72].

The procedure to obtain the dielectric constant of an unknown sample is carried out as follows[33]

- Tip parameters, such as radius and half cone angle, are calibrated by taking an EFM approach curve on a bare part of the substrate and comparing it to theoretically calculated ones.

- The sample geometrical parameters such as size, thickness or height are obtained from the AFM topographic image.
- Then an EFM approach curve is taken on the sample with unknown dielectric properties and compared with theoretically calculated ones for the dielectric constant as the single unknown.

This procedure was successfully applied to various samples to identify their dielectric constant[32–34,72–77], which in turn provided one with a sneak peek into their properties and functionalities. Evaluation of the dielectric constant would also assist a great deal in sub-surface characterization, as the conducting nanostructure in a dielectric matrix would provide us with heterogenous ε_r mapping. Since the ε_r is unique to the material even though they have similar structural properties, the buried material could be identified from the dielectric response.

The SDM technique has been recently extended to mapping the dielectric constant of a whole bacterial cell[37] by using Scanning Dielectric Force Volume Microscopy, described in *Section 3.1*. This thesis makes use of the SDFVM technique for identifying the subsurface elements due to its operational efficiency. The advantage of using a force volume technique in subsurface studies is that it adapts better to non-planar samples than the conventional direct constant plane EFM imaging. In SDFVM, one has the topographic, electrical, and mechanical data from each squared pixel of the sample. This obtained information contains all the data required to address the properties of subsurface features. The usage of SDM in this thesis is in the line of determining geometrical properties by assuming the dielectric constant to be known, in line with what reported for non-buried nanoobjects in Lozano et al.[78] by our research group.

Further details on the specific implementation used in these techniques is given in the forthcoming chapters. Chapter 5 & Chapter 7 describes the numerical modelling and approaches carried out for studying silver nanowire nanocomposites using EFM and Chapter 8 contains the results of experimental studies with silver nanowire nanocomposites, their imaging and analyses and the coupling of numerical approach to obtain the subsurface depth information of the silver nanowire nanocomposites.

Chapter 4

Silver nanowire nanocomposite materials

This chapter outlines the importance of silver nanowire nanocomposites along with its applications in various fields. This chapter also discusses the present characterization methods and the need for subsurface characterization to understand and improve the performance of silver nanowire nanocomposites.

Nanocomposites, one of the most successfully applied nanotechnology research products of the last two decades, consists of a conventional bulk matrix with nanostructures dispersed within it. Depending on the application, the nanostructures are varied to be nanowire, nanoparticles, nanodots etc., and the choice of the bulk matrix to be polymeric, semiconductor, biological etc.. The addition of nanostructures in the existing composite matrix is observed to increase or enhance some physical and chemical properties of the matrix, so that a new material emerges from the combination, with mixed properties.

There is a broad range of nanocomposites with a wide versatility, containing numerous benefits and so incorporated into various applications. Some of the noteworthy applications include the nanocomposite used for biosensors, electrochemical sensors, drug delivery platforms, wastewater treatment, material sciences and a huge boost in the polymer technology[79].

Among the plethora of nanocomposites, Silver Nanowire Nanocomposites (SNN) have their own set of undeniable applications. Silver nanowires (AgNWs) are cylindrical metallic nanowires that are generally tens to hundreds of nm in diameter and few µm in length (see a SEM image of AgNWs in Fig 4.1). The optimal aspect ratio of the silver nanowires (AgNWs) and its density enables to modulate the electrical properties of the material, such as the conductivity[80,81] and electrical permittivity[82], or the thermal properties[83] of the composite matrices. Due to their broad range of electrical, optical and mechanical advantages, AgNWs nanocomposites have been used as functional materials in solar cells[84,85], supercapacitors[86], sensors[87,88], photodetectors[89,90], Organic Light-Emitting Diodes(OLED)[91], Polymer LEDs[92], Flexible thin-film transistors[93], EMI shielding materials[94], electrochromic devices[95] and touch panels[96].

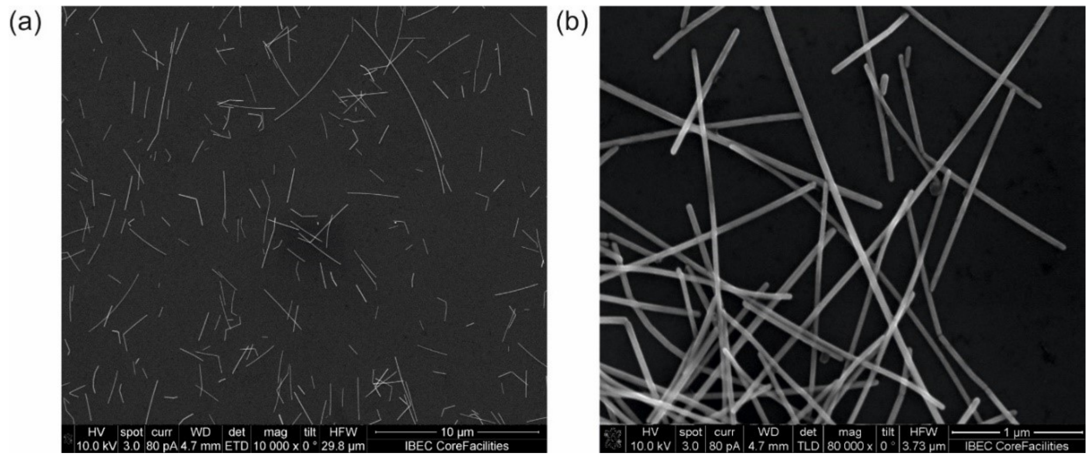

Figure 4.1. (a) Large scale SEM image of silver nanowires ~50 nm in diameter on a highly doped silicon substrate. (b) Zoomed in SEM image depicting their geometrical dimensions.

It is worth noting that the influence of AgNWs in the properties of the composites can be brought by only adding few percent (% in weight) of AgNWs[97]. This addition (schematically represented in Fig 4.2), interestingly, does not influence the physical properties of matrices (e.g., elasticity) but adds on the desired properties to the composites. For example, adding AgNWs to a polymer film will not impact its polymer's native properties like stretchability, transparency and flexibility and additionally would provide an increase in its conductivity. These make AgNWs a convenient addition to the application of flexible and transparent electrodes for wearable applications[98,99], solar cell applications[100,101], stretchable dielectrics[97,102] (few examples can be seen in Fig 4.3). In addition to this, some AgNW composites also offer the feature of being solution-processable[103,104] (or) printable[105,106]. AgNWs also provide the ease of dispersion in many experimental solution and polymers[80] .

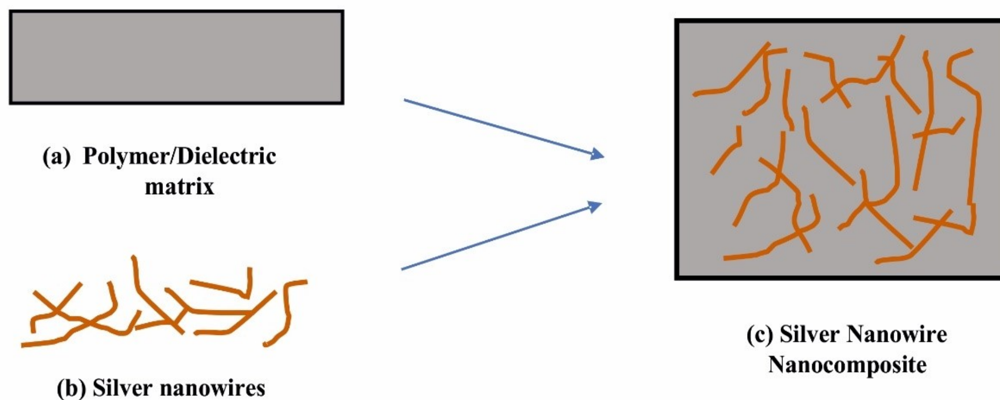

Figure 4.2. Schematic representation of silver nanowire nanostructures dispersed in the bulk matrix to obtain the silver nanowire nanocomposites.

As the scarcity of indium resources increases by the day[103] and the deficient properties like toxicity, expensiveness and brittleness[106] are being addressed, huge efforts are made to develop new age flexible transparent electrode to replace Indium Tin Oxides (ITO) in touch screens. AgNW composites exhibit optoelectronic properties much similar to ITO[107–109] and have been predicted to be a competent successor to ITO[110].

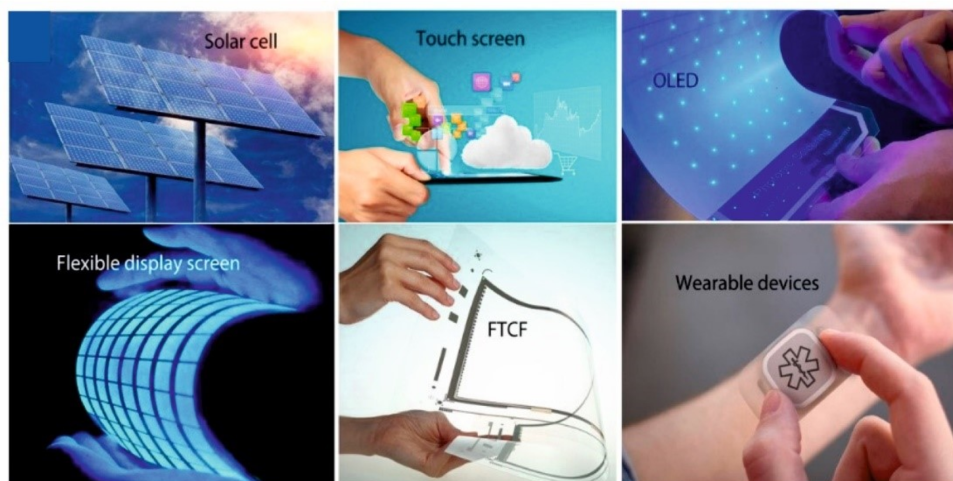

Figure 4.3. Prevalent applications of silver nanowire nanocomposites in the recent advancements right from solar cells to wearable devices (Obtained from Xiaoli et. al. [106])

Silver Nanowire Nanocomposites (SNNs) acquire their modified and enhanced physical properties from the structural properties like the size, aspect ratio and dimensions of the nanowires and also from their position in the bulk volume, their geometry, alignment, concentration, and network formation. To understand how the structural properties of nanowires impact the functional properties of nanowires and to further increase their efficiency in the above-mentioned application, sub-surface characterization is required.

Characterization of SNNs is basically done with the help of Scanning Electronic Microscope (SEM) [with inherent difficulties in the case of polymeric matrices due to their insulating nature] or Atomic Force Microscopy, since the protrusions induced by the buried nanowires on the nanocomposite are identifiable in the topography. These above-mentioned methods offer, in the best of the cases, a 2D projection image of the distribution of the nanowires. In order to obtain the three-dimensional distribution, nanoscale tomographic techniques should be sought after.

The current benchmark for the characterization of materials are electron microscopies (EM), as mentioned before, albeit few studies on AgNW composites have been reported. Applying these techniques to polymeric nanocomposites brings about specific complications including specific sample preparation

protocols like sectioning of the bulk sample, milling, or imaging under high vacuum conditions. The characterizations are also carried out in large scale instruments which are in turn large and expensive, in addition to above mentioned problems involving EM and polymeric matrices.

Our understanding of SNNs is, then, limited by the tools we possess. These practical challenges could be addressed with the recent advancement of nanoscale SPM tomographic techniques. The advantage provided by the subsurface SPMs is unparalleled. The main merits include the characterization of virtually any sample [conductive, polymeric, dielectric] in any environmental conditions [inert, ambient, vacuum] on intact samples. Having said that, true nanotomographic methods that are able to provide depth sensitive information-based on the SPM subsurface methods are scarce.

As we saw in *Section 3.3*, Electrostatic Force Microscopy (EFM) among the parent SPM family has achieved considerable progress in implementing nano-tomographical techniques. Detection of depth of nanotubes in polymeric matrices has been carried out as a beneficial nanotomographic application[62,63], in addition to the determination of the dielectric properties of confined water on the buried nanometric channels[69]. In our research group of Nanoscale Bioelectrical characterization under Dr. Gabriel Gomila and Dr. Rene Fabregas, the capability of Electrostatic Force Microscopies has been theoretically analyzed[38]. It was shown that the size of the nanostructures, the permittivity of the structure and the depth can be found with good accuracy if the other two parameters are known.

In Chapter 8 of this thesis, we could find this exact phenomenon in SNNs where the size and relative permittivity of the AgNWs is known, and hence the depth distribution of the buried nanowires could be addressed.

Chapter 5

Materials and Methods I: Numerical theoretical modelling of EFM

This chapter contains the materials and methods followed in numerical theoretical analysis. This chapter provides the basic framework of theoretical analysis while outlining the procedures in geometry, meshing, analysis and verification. The section 5.1 contains the basics of theoretical modelling and numerical analysis followed by section 5.2 where the numerical modelling of EFM applied to single buried nanowires is studied. The COMSOL models in section 5.1 have been designed by me and the model in section 5.2 has been designed by Dr. R. Fabregas. The simulations and the analysis have been carried out by me with the support of Dr. R. Fabregas and Dr. G. Gomila. Further application of the numerical analysis can be seen in chapter 7.

5.1. Basics of theoretical modelling and numerical analysis

Introduction:

Complex experimental samples like the subsurface samples analyzed in this thesis, require better understanding and alternate modes of verification. For this reason, our research group specialized in comparing both experimental and computational results to provide better accuracy and precision. Before plunging into the computational designing a full Electrostatic Force Microscopy with functional probe and subsurface sample, initial studies were carried out, to understand the working and efficiency of the computational models. This process involved designing simple models that resemble the probe (a sphere) and metal substrate and calculating the electrical force as the different parameters were varied[111]. Below we present the main results obtained, which complement earlier results obtained with 2D and 3D calculation in the thesis of Dr. Daniel Esteban-Ferrer[111] from our research group.

Theoretical simulation and mathematical modelling have evolved to be an integral component in the validation of the experimental methods and results. One of the important constraints that has been faced until now, is that most of modelling efforts were done in two-dimensional (2D) axially symmetric geometries, as opposed to the experimental conditions, which most often are 3D in nature. This present thesis has overcome this drawback by extrapolating the existing 2D modelling capabilities to the more general three-dimensional (3D) geometries, building upon earlier developments in the group, pioneered by Dr. D. Esteban-Ferrer and largely developed by Dr. R. Fabregas. The advantage lies in the close resemblance of the setup to the experimental methods.

Numerical analysis:

COMSOL Multiphysics 5.3 is a multiphysics simulation software that acts as a finite element analyzer and solver. The software functions by coupling systems of partial differential equations and pairing them with physics-based program interfaces. COMSOL is used in this thesis owing to its ease in modelling process such as choosing the physics, building the geometry, and meshing the built specimen with respect to its sensitivity and in processing the simulations.

The data are acquired from COMSOL and are, then, plotted into graphs with the help of Origin Pro 6.3. The analytical formulae values are calculated with the help of MathCAD 2015 which are again plotted with the help of Origin Pro 6.3.

The building of a model in COMSOL works in the following steps: A model wizard is chosen with a 3D design geometry. Then the parameters of the desired geometry are entered, which can also be assigned using already set parameters, through a declaration or equation. After the model is built, the material properties can be defined with pre-set material database [like air (ε_r=1), water (ε_r=80) or other metals (ε_r >> 100)] or a special material can be customized with our desired properties.

Following this, the important step of designing the mesh is addressed. The higher density of the mesh, the more accurate the results. However, high density meshing leads to numerous finite elements, which causes longer simulation times. A trade-off between the finer mesh size and the simulation time is achieved for efficient and effective simulations. Then the physics is set as electrostatics for the domain, terminal and each geometry can be assigned a unique value based on our necessities. Once the model is computed, data plots & derived values can be extracted from the computed data results.

The calculation of the electric force is carried out through the surface integration of Maxwell's upward electric surface stress tensor *(es.un.Tez* in the COMSOL notation*)*. Then, the capacitance gradient is calculated from the relation,

$$\frac{dC}{dz} = \frac{-2 * \mathrm{es.un.Tez}}{\mathrm{V}^2}, \mathrm{Units}\, \frac{\mathrm{F}}{\mathrm{m}} \tag{5.1}$$

where V is the potential applied (usually 1V).

5.1.1. Sphere over an infinite conducting substrate

Geometry & Meshing:

The simulation domain consists of a cylinder that is 10 μm tall (h_c) and 20 μm wide (R_c). The cylinder top layer and the side layers are considered to be an infinite element domain, in the COMSOL terminology (as seen in schematic Fig 5.1). This is done to simulate a large system, without the need to effectively model all the volume. The dimensions are selected so that they do not play any role in the electric force calculation (which is further explained in Fig 5.4). A sphere is placed inside the cylinder domain close to the bottom layer of the cylinder from the inside (Fig. 5.2(a)). The large-scale wireframe of the model can be noticed in Fig 5.2(b) and the zoomed in sphere with the bottom layer is seen in Fig 5.2(c).

The distance between the bottom layer and the sphere is known as the tip-sample distance (z) and is varied throughout our experiments. The radius of the sphere (R) and the tip-sample distance (z) are varied by sweeping those parameters to find the dependence on them of the capacitance (C) and capacitance gradient (change in capacitance, dC/dz). Initially, the geometry is defined separately by forming composite structures (explicit, complement, edges and boundaries) for the ease of applying the physics and boundary conditions (as shown in the schematic Fig 5.1 and in Fig 5.2(a)).

As noted before, meshing density becomes an important parameter as it influences the number of finite elements that can be averaged/integrated to provide a unique solution. Meshing is done separately for different edges, boundaries, and defined geometries with free tetrahedral, triangular, and customized meshing. To improve the meshing, scale geometries can also be changed in all three axes. In order to eliminate the low-quality noise and achieve high sensitivity, a smaller cylinder is constructed in the large basal cylinder closer to the sphere, with ultra-fine meshing (as seen in Fig 5.2(d)). This improves the quality of the results as it improves the number of finite elements closer to the sphere, which provide the noise-free average of results in our target area. Setting the appropriate tolerance level is also important, with the default setting being $10^{-15.}$

For our electrostatics force calculation, the inner sphere is assigned to an arbitrary 1 Volt (V =1V) and the substrate/ground is considered as 0 Volts (V = 0V). The electrical potential distribution around the whole model can be seen in Fig 5.2(e).

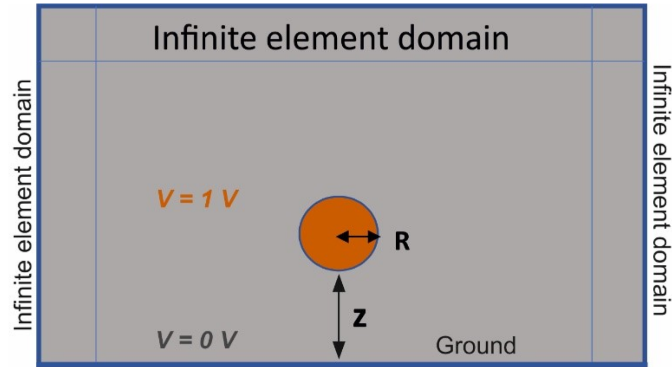

Figure 5.1. Schematic diagram representing the cross-section of the 3-D geometry of a sphere over an infinite conducting substrate. The sphere is enclosed in a cylindrical domain in which the top and side layers are set as infinite element domain which plays a minimal role in calculations similar to experimental models. The distance between the sphere-bottom ground layer (which is similar to EFM tip-sample distance) is denoted as z and R indicates the radius of the sphere. For electrostatics calculation, the sphere is assigned V =1 V and the ground is assigned V =0 V. When the sphere is moved, the change in capacitance and thereby the capacitance gradient is calculated.

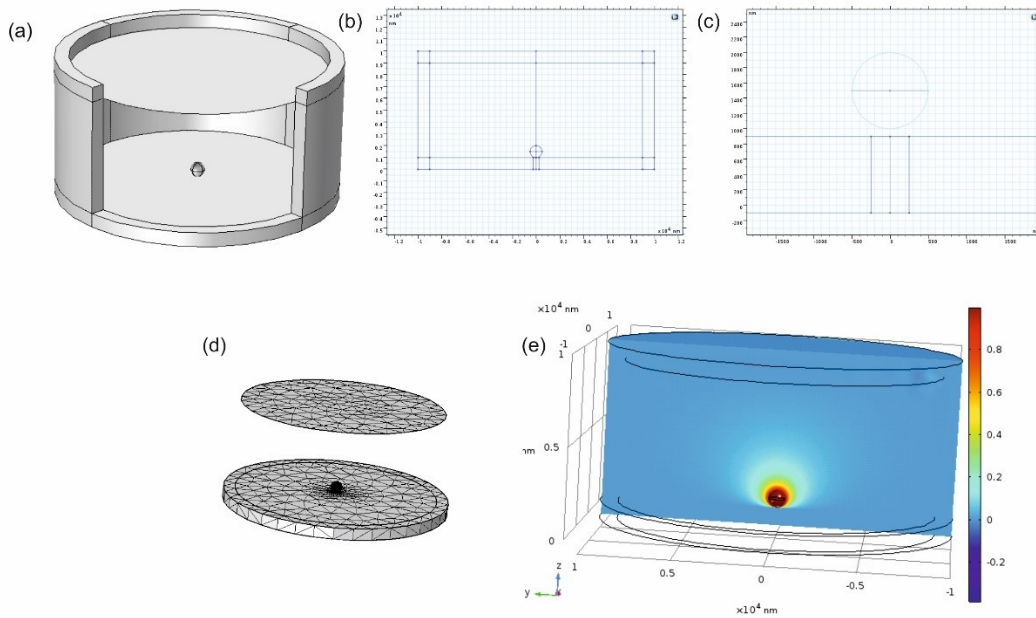

Figure 5.2. (a) The geometry represents the construction of a metallic sphere separated by a distance (z) ranging in nm from the metallic substrate (as visible in (b) & (c)). The upper and sides of the cylinder are considered as infinite layer domain and they will be playing minimal role in the calculations similar to the experimental models. The meshing (d) elucidates the geometry breaking into numerous finite elements. As we can deduct from (d) higher amount of meshing is present on the sphere and the places closer to the sphere on the substrate. This is specifically carried out to ensure higher precision that will be obtained due to the averaging of numerous finite element analysis. Finally, (e) shows the electric potential distribution during the calculation, portraying the voltage applied to the sphere and its interaction contours with the surrounding geometry.

Convergence:

In order to find the best possible meshing parameters for the designed geometry, mesh convergence is of prime importance. Mesh convergence is calculated by increasing the meshing (thereby increasing the number of domain elements), to check for the change in value of the capacitance gradient (dC/dz). The mesh convergence occurs after a point where changing the number of domain elements will not change the dC/dz significantly (as we see in Fig 5.3). The meshing (with the number of domain elements/ degrees of freedom) where the values are relatively constant is taken for further simulations and the results obtained are verified with analytical formula to verify their convergence.

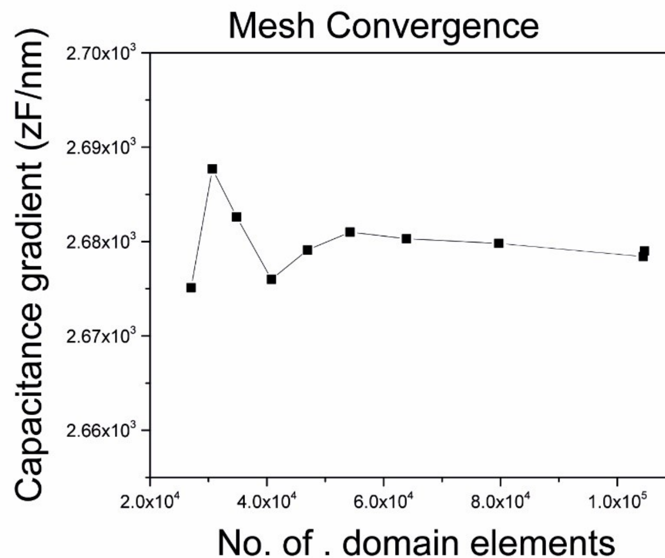

Figure 5.3. Graph depicting the change in capacitance gradient over the variation of domain elements. At the far end of the graph, we could infer that the change has slowed down and is minimally responsive to the change in the number of finite elements. Mesh convergence is believed to be achieved at this point and it is considered for further numerical simulations.

Calculations have also been carried out to observe the effects of the side layers of cylinders and the top layer of the cylinder. This is carried out to observe their influence on the surface of the sphere and to confirm that they play a negligible role in the simulated values. For example, the force experienced by the sphere is observed as a function of the sphere-substrate distance for different values of the height (h_c) in Fig.5.4(a). The radius (R_c) of the cylinder is set to 10 μm. It is observed that varying the height of the cylinder did not provide any change in the force exerted or experienced. Varying the radius provided the same result as well confirming that the side and top layers do not influence the forces on surface of the calculated sphere.

In Fig. 5.4(b) we verified by moving laterally the sphere (scanning) no effects of the lateral walls was detected. It is worth noting that these calculations are carried out for wide range of sphere movement, significantly larger than the movement that is used in our experiments,

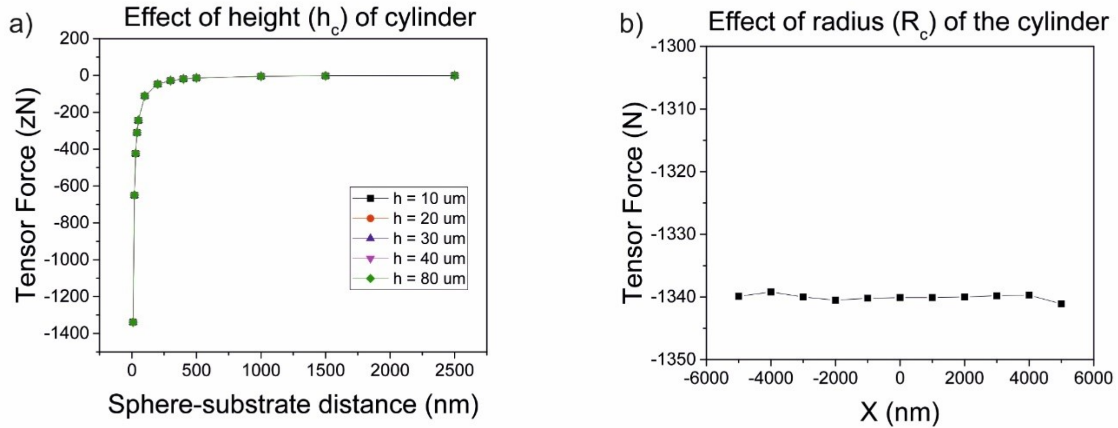

Figure 5.4. (a) Graph portraying the tensor force experienced by the sphere as a function of the sphere-substrate distance when the height of the cylinder simulation domain is varied. As the height (h_c) is changed from the default 10 µm to progressively 20 µm, 30 µm, 40 µm, 80 µm, we can observe no change in the farthest tip-sample distances. This proves that the height of the cylinder is farther than the sphere to exert any force or influence its capacitance. (b) The radius (R_c) 10 µm shows to play no role in influencing the force on the sphere for a comfortably large range of lateral distances traveled by the sphere.

Exact analytical solution for a sphere over a conductive substrate:

To check the sensitivity and effectiveness of the simulated model, the results are compared with the analytical formula to verify the obtained results through simulations. For example, the exact analytical solution[112] to find the capacitance of a sphere over an infinitely conductive substrate is,

$$\text{Capacitance, C} = 4\pi R\varepsilon \sum_{n=0}^{50} \frac{\left[2\sqrt{z\left(\frac{2+\frac{z}{R}}{R}\right)}\right]}{e^{(1+2n)*(a\cosh(1+\frac{z}{R}))}-1} \tag{5.2}$$

If the values of tip-sample distance (z) and radius of the probe used (R) are known, the capacitance can be analytically deduced with the help of Eq. (5.2) .

Then, the capacitance gradient (dC/dz) can be computed using the discrete derivative (finite difference)

$$\text{Capacitive gradient}\left(\frac{dC}{dz}\right)=\frac{C(z+\Delta z)-C(z)}{\Delta z} \tag{5.3}$$

Effect of tip-sample distance on the capacitance gradient for different radii of the sphere:

The capacitance gradient (dC/dz) changes with the variation of distance from the sphere to the surface, (which is completely analogous to experimental tip-sample distance, z). To provide a sense of the change in capacitance gradient when key parameters are varied, Fig 5.5 shows an example of change in the radius of the sphere (R) and tip-sample distance (z) calculated computationally. It can be seen from Fig 5.5(a) that when the sphere of R=500 nm is increased till R=1000 nm, the capacitance gradient increases as well. This calculation was carried with fixed tip-sample distance z=10 nm. In Fig 5.5(b), when the tip sample distance is varied, high gradient signal is obtained when the sphere is closer to the substrate and saturates to a constant value when the sphere is far away. This graph is similar to the experimental EFM approach curve (2ω oscillation force curve) with probe R=500 nm, when the probe approaches the sample.

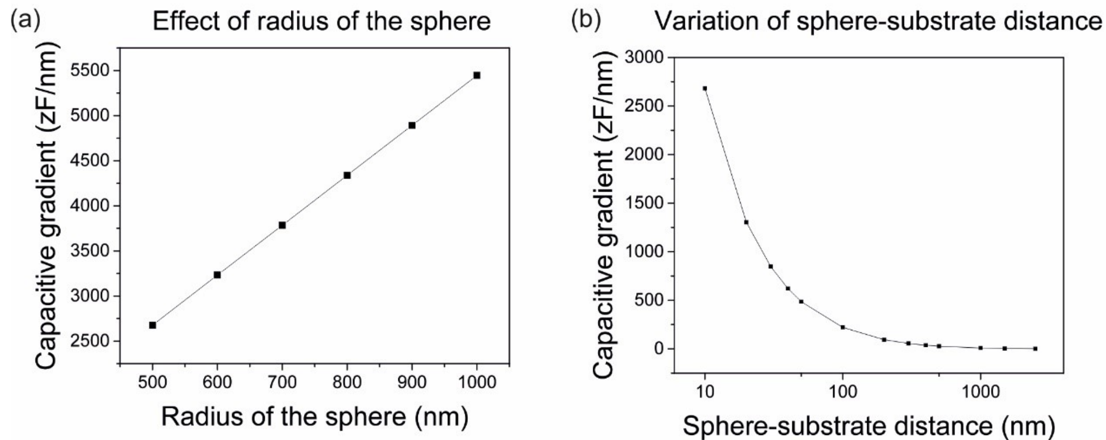

Figure 5.5. (a) Theoretical modelling results shown in a graph attributing the effects of change in radius of the sphere (R) to the change of capacitance gradient values for a fixed tip-sample distance of z=10 nm. The capacitance gradient increases relatively as we increase the radius of the sphere due to its increased surface area that in turn increases its electrostatic force interactions. (b) This graph shows the effect of change in tip-sample distance on capacitance gradient with the radius of sphere as R=500nm. As the sphere (probe) moves further away from the substrate, the capacitance value drops and becomes constant at long distances specifying that no change in capacitance is observed.

How does the capacitance of the sphere change, if we vary tip-sample distance and sphere radius simultaneously? In Fig. 5.6 the continuous lines represented theoretical simulations and the dots represented analytical formula values. These analytical values are calculated from Eq. (5.2) with the same parameters used in the numerical conditions. As we can infer from the graphs in Fig 5.6, both the values are in compliance with each other.

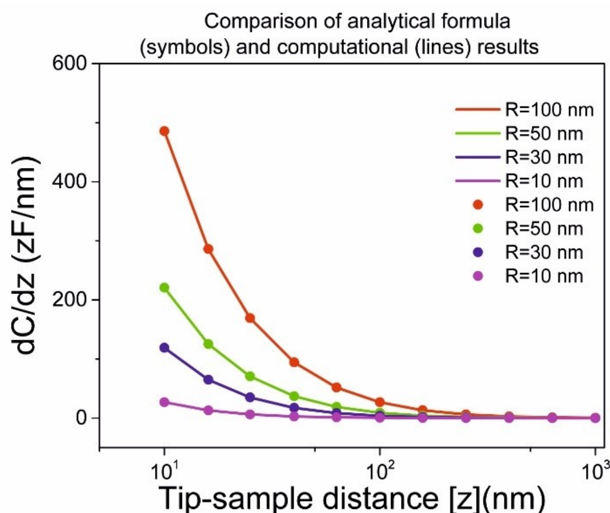

Figure 5.6. Comparison of computational values and analytical values obtained from Eq. (5.2). Graph showing the change in capacitance gradient (dC/dz) as we vary the tip-sample distance (the EFM probe moving toward and away from the sample) and the sphere radius (radius of the EFM probe). The continuous lines indicate the theoretically simulated values, and the symbols pertain to the values calculated from the analytical formula. As we evolve into more complex models, analytical formula ceases to exist or would need further approximations to be precise.

Comparing analytical and computational solutions:

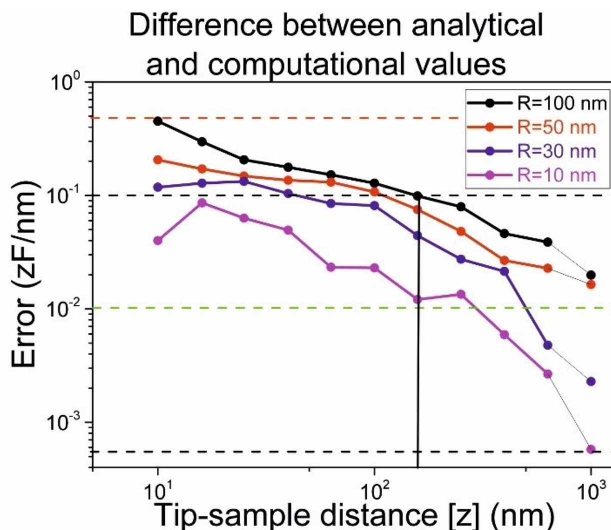

Figure 5.7. The error found by the difference between computational and analytical values is plotted as a function of tip-sample distance. The tip sample distance (z) indicates the distance from 1 nm to 1000 nm in the x axis. The error observed here provides an error of less than 0.5 zF/nm for the radii calculated. Experimentally, the electrostatic force is best achieved in the lowest tip-sample distances and the error less than 0.5 zF/nm requires rigorous precision and invariably low instrumental noises.

Finally, the simulated values are compared with the analytical solution in Eq. 5.1 in Fig 5.7 . The difference between them was observed to be less than 0.5 zF/nm, which affirms the reliability of theoretical modelling for 3D geometries. In the present thesis, the experimental techniques have a noise range of 1-2 zF/nm, below which the obtained signal is harder to be differentiated from the noise.

5.1.2 Sphere over a dielectric film

Geometry:

The design is similar to *Section 5.1*, (Sphere over an infinite conducting substrate) with the addition of a dielectric layer on top of the substrate. This layer with a thickness t (depicted in black in Fig 5.8(a)), is added between the conductive base and the sphere. The three-dimensional geometry with the dielectric layer closer to the bottom substrate layer can be seen in Fig 5.8(b). The meshing has been carried out similar to previous section and the finite elements are observed in Fig 5.8(c).

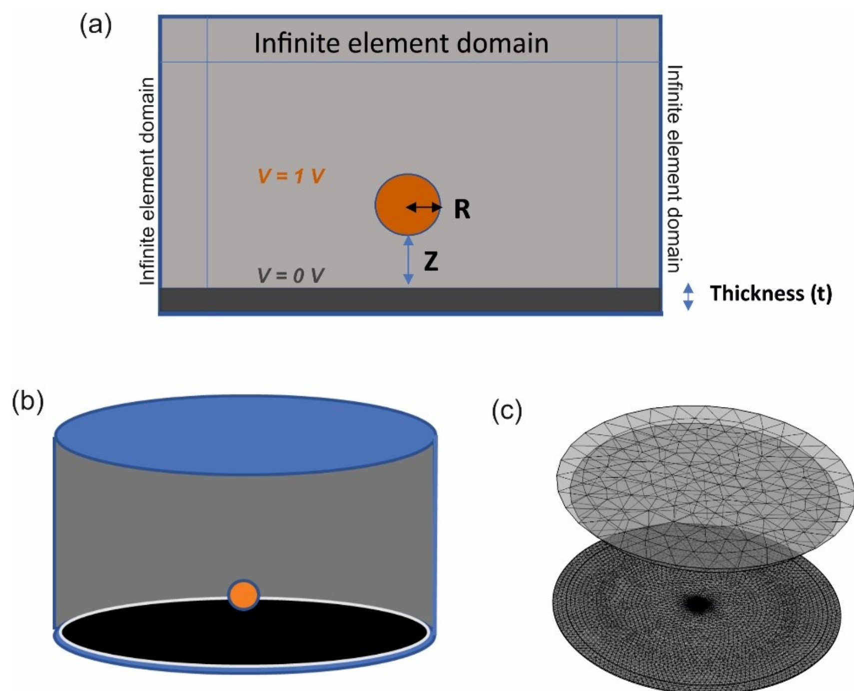

Figure 5.8. (a) The schematic represents the cross-section of the 3-D model of sphere over a dielectric layer shown in (b). As we can observe from the cross-section, the cylinder, similar to previous model, has the top and side layers

set as infinite element domain, which means the cylinder is infinitely long and wide. The black layer represents the dielectric layer with relative permittivity ε_r and a thickness t. The distance between the sphere and the dielectric material (which is similar to EFM tip-sample distance) is denoted as z and R indicates the radius of the sphere. (c) shows the meshing of the designed geometry broken down into numerous finite elements until mesh convergence is achieved.

Convergence:

As seen in *Section 5.1.1*, mesh convergence is calculated by increasing the meshing (thereby increasing the number of domain elements), to check the change in the value of dC/dz, the capacitance gradient. The mesh convergence occurs after a point where changing the number of domain elements will not change the dC/dz significantly (as observed in Fig 5.9). The meshing (number of domain elements/degrees of freedom) where the values are relatively constant is taken for further simulations and the values are found to be in accordance with the analytical values.

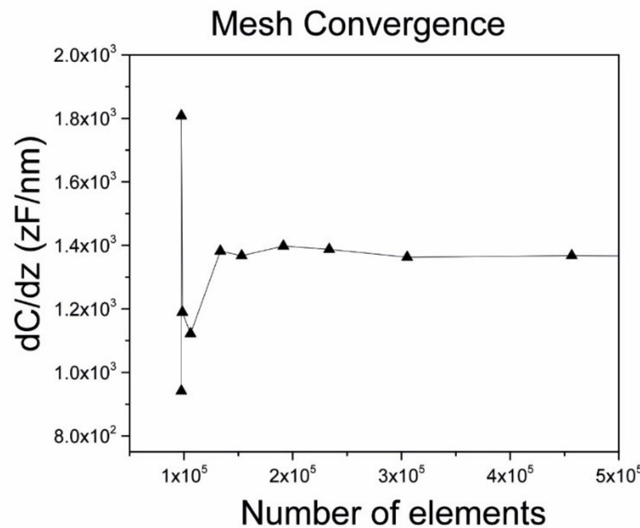

Figure 5.9. Graph depicting an example of the change in capacitance gradient over the variation of the number of domain elements for a sphere over a dielectric film. As the number of finite elements increase in the meshing, we could infer that the change in dC/dz has slowed down and is minimally responsive to any further variations. Mesh convergence is believed to be achieved at this point and those number of elements in meshing are considered for further numerical simulations.

Exact analytical solution for an infinite thick dielectric film

To check the sensitivity and effectiveness of the simulated model, the results are compared with the analytical formula, to verify the obtained results through simulations. In the present case, an analytical formula can only be found in the limit of an infinitely thick dielectric layer[113], provided by

$$C = 4\pi\varepsilon_0 R \sinh(\text{acosh}(1+\frac{z}{R}))*\sum_{n=0}^{\infty}\left[\left(\frac{\varepsilon_r - 1}{\varepsilon_r + 1}\right)^{n-1} * \frac{1}{\sinh\left(n * a\cosh\left(1+\frac{z}{R}\right)\right)}\right] \quad (5.4)$$

which can be used to obtain the capacitance gradient upon its derivative. The analytical formula Eq. (5.4) is only applicable for the cases where the thickness of dielectric (t) tends to be infinite.

If the values of radius of the probe used (R), tip-sample distance (z) and the relative permittivity of the dielectric layer is known, the capacitance can be found from the Eq. (5.4) and thereby deducing the capacitance gradient.

The capacitance gradient (dC/dz) can be computed using the discrete derivative (finite difference), similar to Eq. (5.3)

$$\text{Capacitive gradient}\left(\frac{dC}{dz}\right) = \frac{C(\text{z}+\Delta z) - C(z)}{\Delta z} \quad (5.5)$$

Effect of the thickness of the dielectric layer on the capacitance gradient:

Our final aim of subsurface characterization involves detecting buried entities under a dielectric matrix. In accordance to moving towards our desired trajectory, let us consider the dielectric layer with the value ε_r=2, which in turn belongs to most of the commonly used polymers. As we know from the previous section, increasing the distance between sphere and substrate (probe/tip-sample distance, z) the electric forces acting on the sphere reduces and tends to become constant at large distances. In accordance with that, here the change in capacitance gradient is calculated as a function of the dielectric film thickness for z=150 nm and z=10 nm away from the surface of the dielectric material (Figs. 5.10(a) and (b), respectively). These values are also tested for a dielectric layer with the value ε_r=20 (Fig. 5.11).

The capacitance gradient changes with the thickness of the dielectric layer (t) present in between the sphere and the conducting substrate. In the graph plotted in Fig 5.10(a-b) and Fig 5.11(a-b), the dashes represented the calculations with the analytical formula in Eq. 5.3 (valid for infinite thickness) and the symbols and continuous lines represented numerical calculated values. As we can infer from the graphs, both of the values match at the larger thicknesses corresponding to the infinite limit. The other graph shown in Fig 5.10(c) and 5.11(c) denotes the comparison of analytical and computational values with the difference

between the closest tip distance and the farthest distance. This is termed as intrinsic graph and is carried out in order to cancel out the intrinsic effects of the simulations (like mesh effects, noise etc.). We can also observe the matching of analytical and computational values in them as well.

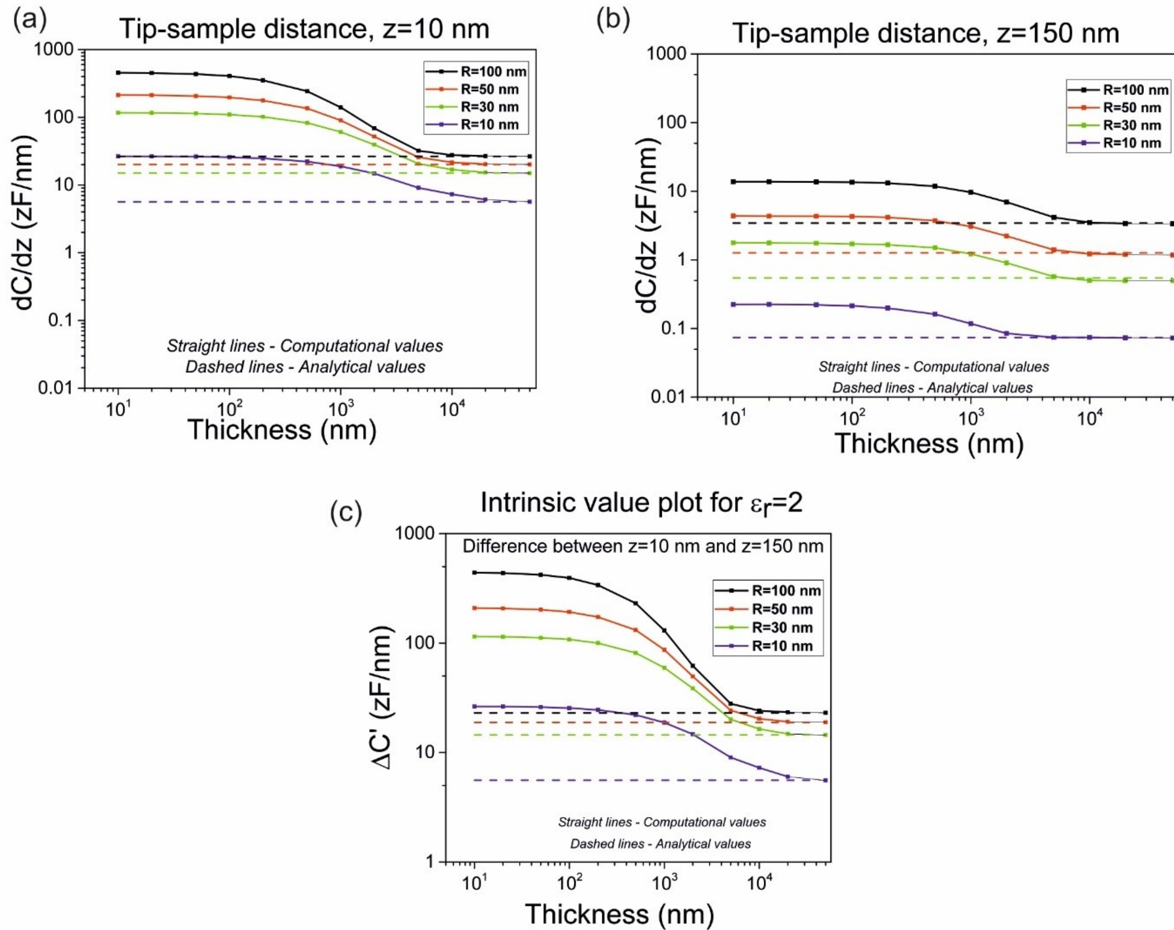

Figure 5.10. Comparison of analytical and computational results for a relative permittivity ε_r = 2, and with tip-sample distances (a) z=10 ,(b) z=150, and (c) the intrinsic value plot subtracting the closest (a) and the farthest (c) tip-sample distances[z]. The radius of the probe [R] is also varied to observe its effect on capacitance gradient when varied along with thickness[t]. The analytical values (dashed) lines are calculated for all varying z and R values. As we observe the analytical formula which holds good for sphere an infinite thickness dielectric film tend to match the computational value at larger thickness (t>5000 nm)

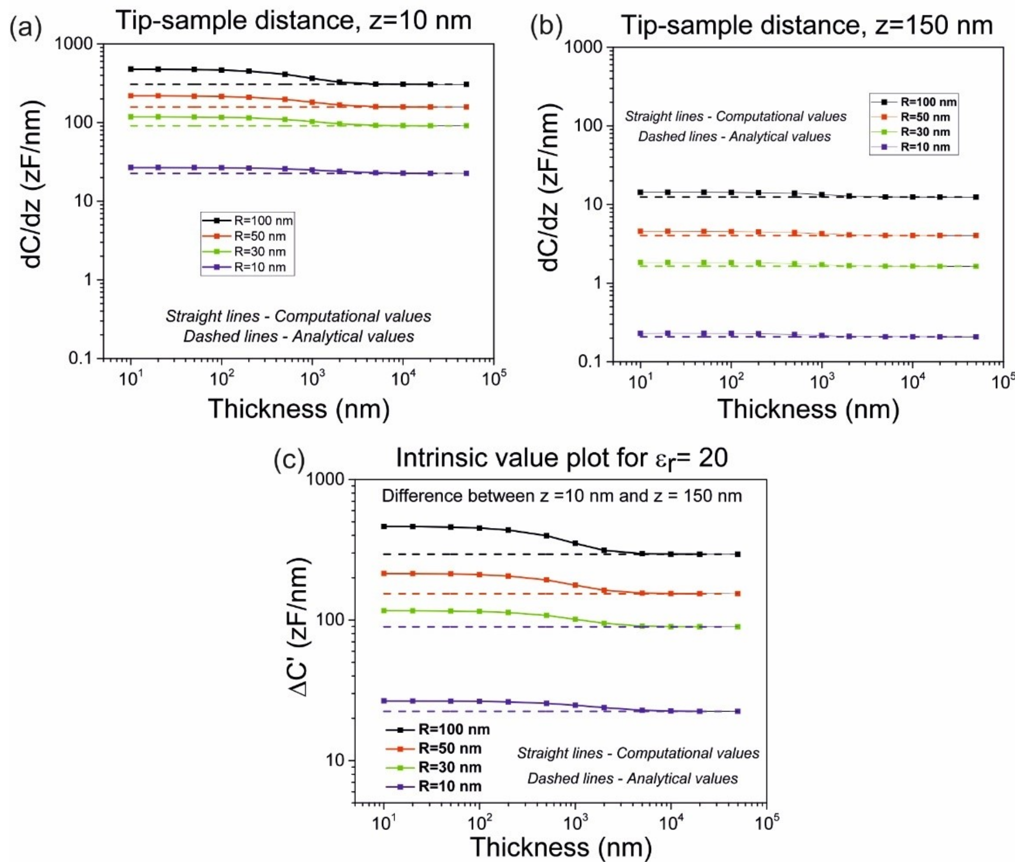

Figure 5.11. Comparison of analytical and computational results for a relative permittivity ε_r = 20, and with tip-sample distances (a) z=10 ,(b) z=150, and (c) the intrinsic value plot subtracting the closest (a) and the farthest (c) tip-sample distances[z]. The radius of the probe [R] is also varied to observe its effect on capacitance gradient when varied along with thickness[t]. The analytical values valid for infinitely thick films (dashed lines) are calculated for all varying z and R values. As we observe the analytical formula which holds good for sphere an infinite thickness dielectric film tend to match the computational value at larger thickness (t>5000 nm). As we can infer from ε_r = 2 values in Fig 5.10 and ε_r = 20 values in Fig 5.11, we can observe that as the ε_r increases the signal/contrast begins to reduce. This is further touched upon in the following topic and also in Section 5.2.

Relative permittivity variation:

The capacitance gradient is observed to be changing with the thickness of the dielectric layer (t) and also, with its relative permittivity. This trend with ε_r is further tested by varying the permittivity with respect to thickness. Again, these values are compared with the analytical formula values which exist for infinite thicknesses.

In the Fig 5.12, the continuous lines with dots represent the numerical theoretical simulations and the hinted dashes represent the analytical formula values. As we can see from the graph, both the values match when the thickness is relatively bigger. There is only one analytical value, because the analytical formula

available holds good for infinite thicknesses. We can clearly observe that the larger the dielectric constant of the dielectric layer, lesser the dependence on the thickness is observed. We can also observe the capacitance gradient (dC/dz) in absolute terms increases when the ε_r is larger, due to the screening of the electrostatic interaction, which makes that most of the potential drops in the air gap between the sphere and the thin film, and therefore the inside of the film is little probed.

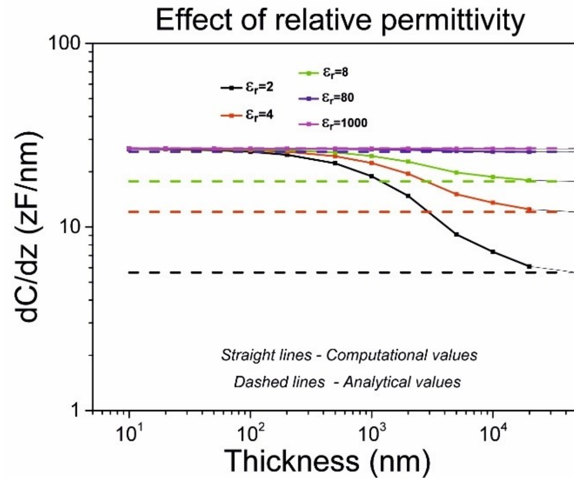

Figure 5.12. Graph showing the nature of capacitance gradient to different relative permittivity of the dielectric layer while the thickness is varied. The value of the relative permittivity of the layer is varied with a wide range of material possibilities. For example, ε_r=2 represents a low dielectric nature similar to polymers while the highest ε_r=1000 represents a conductive nature of the material. As we can see from the graph, both the analytical and computational values match when the thickness is very large since the analytical formula available only holds good for infinite thicknesses.

Comparing analytical and computational solutions :

This comparison is carried out in the large thickness range (thickness over 5000 nm) where the analytical formula approximation is available to compare with our computational results.

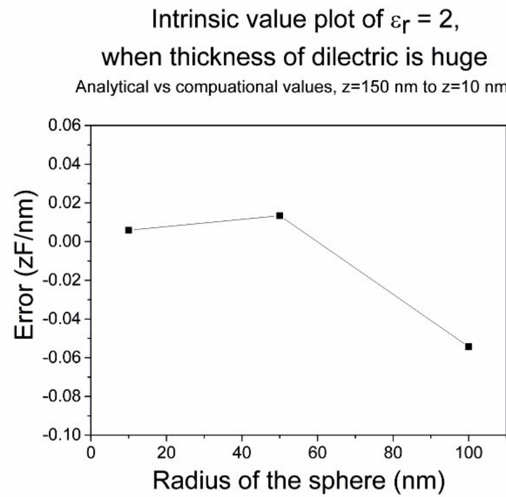

Figure 5.13. The error found by the difference between computational and analytical values is plotted as a function of radius of the probe (R) which is varied from 10 to 100 nm. The error observed here provides an error of ~ 0.06 zF/nm for the radii calculated. Experimentally, the electrostatic force is best achieved in the lowest tip-sample distances and the error less than 0.5 zF/nm requires rigorous precision and invariably low instrumental noises.

The sphere over an infinite dielectric substrate has been simulated and the resultant values are compared with the analytical solution. The difference was observed to be less than 0.06 zF/nm compared to numerical calculations (as seen in Fig 5.13) which shows the reliability of our theoretical modelling studies. As we have noted before, the experimental techniques used in the present thesis have a noise range of 1-2 zF/nm, below which the obtained signal is harder to be differentiated from the noise.

Conclusion:

In this initial study, we have carried the numerical analysis of a sphere over an infinitely long conductive material (EFM probe on top of the metal substrate) and a sphere over a dielectric layer (EFM probe on top of dielectric material) by using a 3D numerical approach. The values from our finite numerical element analysis have been compared with the analytical exact solutions, when available. In both cases, the results match each other within the set sensitivity (~0.5 zF/nm) substantiating the accuracy of our preliminary numerical analysis. This study has served to optimize meshing levels and for dimensions of simulation domains.

5.2. Modelling of EFM applied to single buried nanowires

Following the initial modelling studies in *Section 5.1*, in this section, we extend the analysis performed in the previous section to the realistic case of an EFM tip imaging a buried nanowire in a dielectric matrix. A comprehensive study of the role played by the different system parameters on the capacitance gradient is investigated.

Before heading into the extensive analysis of a subsurface system, let us discuss the importance of theoretical analysis. *Why such comprehensive numerical analysis is necessary in subsurface characterization*? In these tomography experiments several parameters like the tip radius, R, half cone angle, θ, dielectric thickness, t, tip sample distance, z, dielectric constant of the nanowire, ε_w, and of the matrix ε_m, and dimensions of the nanowire, can play a role in influencing the capacitance gradient individually or in combination with other parameters. To find the best parameters for effective dC/dz signal detection from the sub-surface nanowires among the parameters (and also from the numerous possible combinations of parameters), theoretical modelling is indispensable. This theoretical modelling study in addition to providing us the best possible sample and imaging protocols, allow us to be efficient with our time, money, and resources.

For this numerical analysis, similar to the earlier works of the group, a conical tip with a tangent sphere is used.[33,34,75]. The probe consists of a conical tip of half angle θ and height H, ended by a tangent sphere of radius R and capped at the top with a disc cantilever of thickness W and radius (H tanθ+L). Finally, the tip is located at a distance z from the matrix surface. All calculations have been done by using the electrostatic module of COMSOL Multiphysics 5.4 following similar methods to the ones described in *Section 5.1* and in Refs.[38,78,114] . The nanowire is assumed to be metallic (ε_w=1000) with circular geometry with diameter D_w=50 nm. The nanowire is buried at a depth h=10 nm in a matrix of thickness t_m=60 nm. The matrix is set as dielectric with a dielectric constant ε_m =4. The conical probe tip has a radius of R=100 nm with a half cone angle θ=25°. The tip-sample distance (z=20 nm) is considered to be from the top gelatin layer to the probe tip. The entire modelling, similar to models in previous *section 5.1*, follows the schematic represented in Fig 5.14(a). Fig 5.14(b) shows the meshed geometry where it is broken down into numerous finite elements for analysis. The electric potential distribution is represented in Fig 5.14(c), in the presence of the applied voltage. The inset shows the behavior of potential distribution on top of the buried wire.

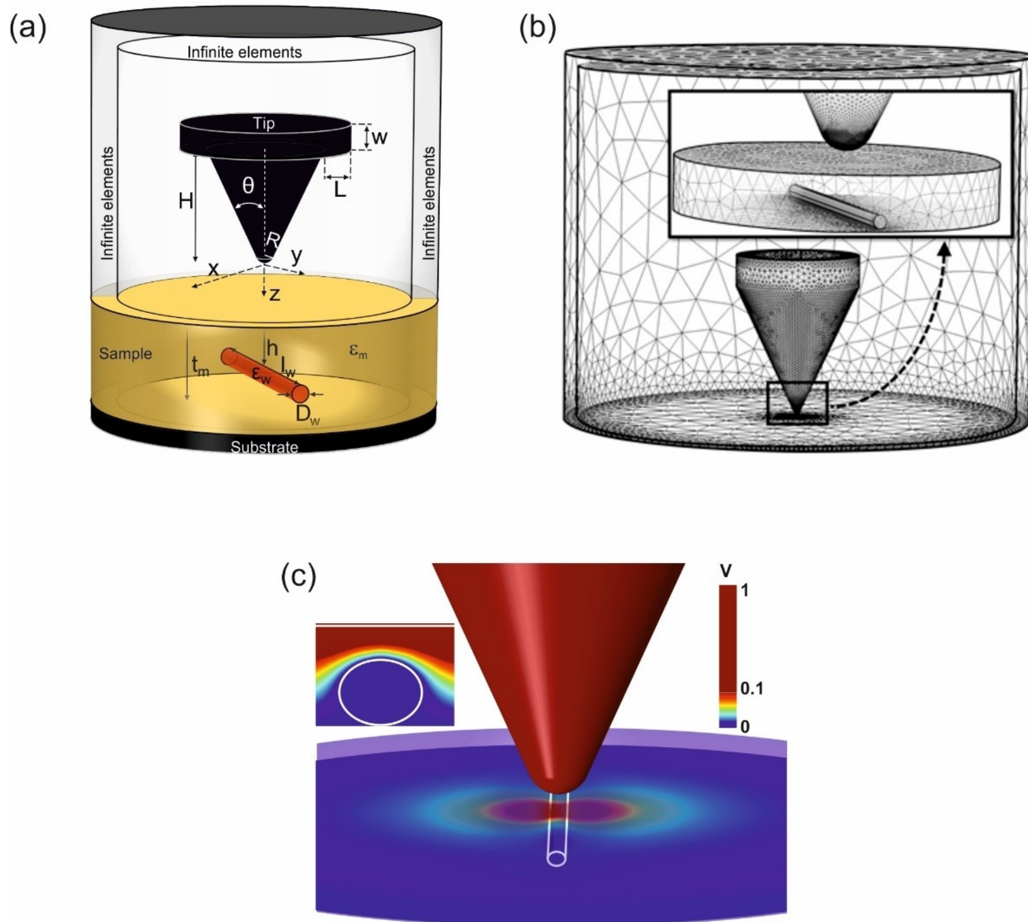

Figure 5.14. (a) Schematic diagram of the geometry of simulation of a nanowire buired in dielectric layer. The probe consists of a conical tip of half angle θ and height H, ended by a tangent sphere of radius R and capped at the top with a disc cantilever of thickness W and radius (H tanq+L). Finally, the tip is located at a distance z from the matrix surface. The nanowire is assumed to be metallic (ε_w=1000) with diameter D_w=50 nm. The nanowire is buried at a depth h=10 nm in a matrix of thickness t_m=60 nm. The matrix is set as dielectric with a dielectric constant ε_m=4. The conical probe tip has a radius of R=100 nm with a half cone angle θ=25°. The tip-sample distance (z=20 nm) is considered to be from the top gelatin layer to the probe tip. These parameters are fixed throughout the experiment unless otherwise stated. (b) Meshing of the entire geometry showing the numerous finite elements for numerical calculations; inset, meshing of the probe and the buried wire separated by distance z (c) Electric potential diagram of the simulation and its distribution when the voltage is applied.

Variation of tip-sample distance (z):

An approach curve similar to an experiemental EFM approach curve (2ω oscillation curve) is simulated. The probe approaches the sample from farther distances to closer, until it is in contact with the sample. In Fig 5.15(a), the approach curves taken on the dielectric film part on top of the buried nanowire and the one taken on the dielectric film part with no wire (bulk film) are represented. The difference between their capacitance gradient values is termed as ΔC' and is represented in the graph inset. It represent the contrast that would be measured in a constant height EFM image. The pink rectangle in Fig 5.15(a) represents

the non-distingushable area between two approach curves. The red dashed line in the inset figure denotes the noise level of the instrument, which is 1 zF/nm. Any changes beneath this 1 zF/nm cannot be differentiated from noise experimentally and so this sets the minimum measurable range of capacitance gradient contrast detectable. The electrical potential distribution when the tip is on top of the wire is shown in Fig 5.15(b) ,

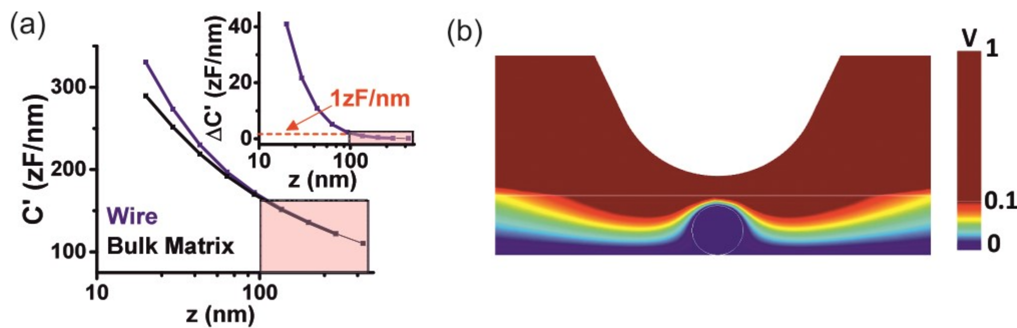

Figure 5.15. (a) Approach curves (approaching the tip towards the sample, thereby changing tip-sample distance[z]) simulated theoretically on top of the thin dielectric film above the buried nanowire and the bare thin film at different places without buried subsurface features; Inset: ΔC' contrast of the wire obtained by subtracting the two curves in (a). The dahsed red line represents the experimental noise level below which the signal and noise could not be differentiated. The pink rectangle represents the non-distinguishable range of distances. (b) Electric potential diagram at z=20 nm

Variation of radius of the probe/tip (R):

In all the electrical force measurement signals obtained by SPM, the radius of the probe (R) plays an important factor. This goes hand-in-hand with the understanding that, higher the tip-radius, the higher its the electrical signal. This might theoretically encourage us to use higher radius probes, to procure the most information about the sub-surface entities, always looking a good balance with the achievable spatial resolution. This property can be visible from the simulated data of various radii signal obtained when a capacitance gradient profile is obtained at a tip-sample distance z=20 nm in Fig 5.16(a). The nanowires are 50 nm long and when imaged with R greater than 50 nm, we are risking the loss of spatial resolution. Higher the radius of probe than the width of the wire, higher the loss of the spatial resolution. This loss is experienced experimentally due to the fact that the decaying of the contrast expands further from the wire when the R is bigger (see Chapter 7 for a specific analysis of this point). The best possible method to choose the R should be by achieving a proper balance between the amount of electrical signal/contrast obtained and resolving the wires spatially. The noise limit is considered at 1 zF/nm (represented by red dashed line in Fig 5.16 (b)) below which the signal and noise could be complicated to differentiate them (as mentioned before).

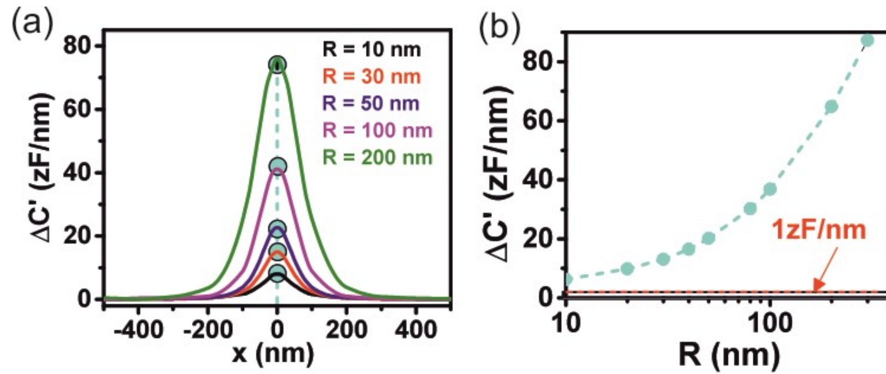

Figure 5.16. (a) Capacitance gradient profiles of the sub-surface wire obtained during capacitance gradient imaging taken at tip-sample distance z=20 nm with probes of different radii from R=10 nm to 200 nm; (b) Change in capacitance gradient ΔC' (Contrast of the experimental image) is represented with respect to radius of the probe (R) by plotting the maximum contrast values denoted with circles in (a). The red dashed line at the bottom shows us the experimental noise level 1 zF/nm below which the signal and noise could not be differentiated. There is a trade-off to be achieved when considering the radius of the probe (R) for subsurface characterization since higher radius provides higher signal/contrast but also decreases the resolution.

Variation of thickness of the gelatin matrix (t_m):

The subsurface imaging faces the most challenging parameter in the form of the depth at which the entities are below the surface. This inturn is directly dependent on the thickness of the burying matrix (t_m). For example, above the nanowire was buried at a depth of h=10 nm [Thickness of gelatin matrix (t_m=60 nm) – Diameter of the nanowire (D_w=50 nm)]. Increasing the thickness of the gelatin matrix influences the electric force felt by the tip. Fig 5.17(a) shows the simulated data obtained during a capacitance gradient profile taken at tip-sample distance z=20 nm when the thickness is varied, with the nanowire being always on the substrate (hence an increase of thickness means here an increase of the buried depth also). We can figure out that the higher the thickness of the dielectric film, the lower the electric force influencing the tip. This result shows us that if the sub-surface entities are buried much deeper in the matrix, the signal can be lower than the instrumental noise range (<1 zF/nm) and the charcterization is experimentally complex. The contrast (difference between the capacitance gradient on the bare film and on the nanowire) depends on the thickness of film and it can be visualized from the graph Fig 5.17(b), which shows the change in capacitance gradient as a function of thickness of the burying matrix. It is imperative to remind that the position of the nanowire is not changed throughout the calculations (on the substrate) and the depth of the buried wire (h) at any point can be obtained by subtracting the value of thickness of the matrix with diameter of nanowire [$h=t_m-D_w$].

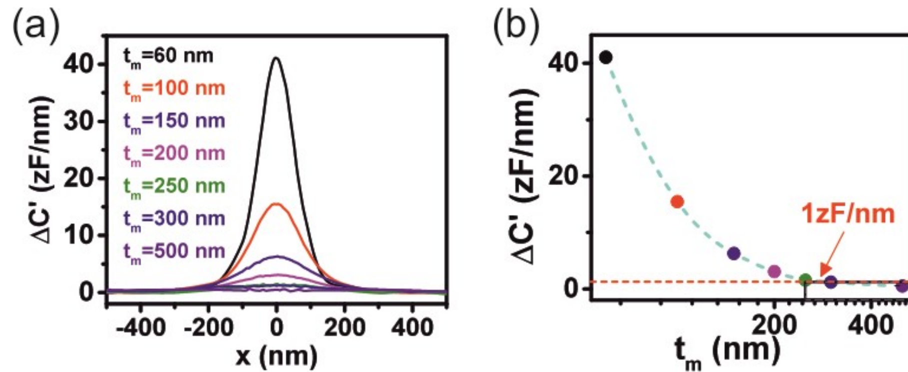

Figure 5.17. (a) Capacitance gradient profiles of the sub-surface wire obtained during capacitance gradient imaging taken at tip-sample distance z=20 nm with different thickness of the gelatin matrix(t_m). (b) Change in capacitance gradient (Contrast of the experimental image) as a function of the thickness of gelatin matrix obtained from the maximum of the profiles obtained from (a). The depth of the buried wire (h) at any point can be obtained by subtracting the value of the diameter of the nanowire from the thickness of the matrix [$h=t_m-D_w$]. These graphs shows that when the thickness of the matrix is increased, the experimental signal/contrast decreases falling into the experimentally inditinguishable noise range when <1 zF/nm.

Variation of the buried depth of the nanowire (h):

Similar to the experiment of increasing the thickness of the surrounding matrix (shown in Fig 5.17) the numerical study has also been carried out about increasing the depth of the nanowire inside the matrix, while the thickness is maintained constant (as shown in the schematics in Fig 5.18). The thickness has been fixed at t_m=160 nm and the depth of the nanowire is varied from h=10 nm to h=150 nm. As iterated before, the depth of the nanowire is calculated from the top layer of the matrix to the top of the nanowire.

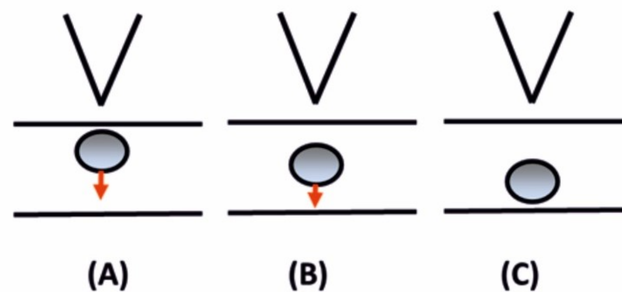

Figure 5.18 Schematic diagram of increasing the depth of the nanowire (h) inside the matrix while maintaining the thickness of the matrix (t_m=160 nm) constant. The measurements are carried out by varying the depth of the nanowire from h=10 nm to h=150 nm. The depth of the nanowire is calculated from the top layer of the matrix to the top of the nanowire. The depth of the nanowires increases from (A) to (C).

In addition to increasing the depth, the relative permittivity of the wire (ε_w) is also varied for each depth. This calculation is carried out to check the behavior of different materials in influencing the electrical force felt by the tip/probe. As we can see from the Fig 5.19, deeper the nanowire is present, the lesser the capacitance gradient obtained. This in congruence with our other obtained data of increasing the thickness of the matrix in Fig 5.17(a). Also, this graph shows that, in a dielectric matrix, the conductive materials (represented by very high dielectric constants here) are easily detectable subsurface as they provide high signal/contrast. The behavior of the change in capacitance gradient in response to different relative permittivities can be seen in the next topic. As mentioned before, the red dashed line indicates the instrumental noise of 1 zF/nm sets the minimum characterizable signal from sub-surface entities.

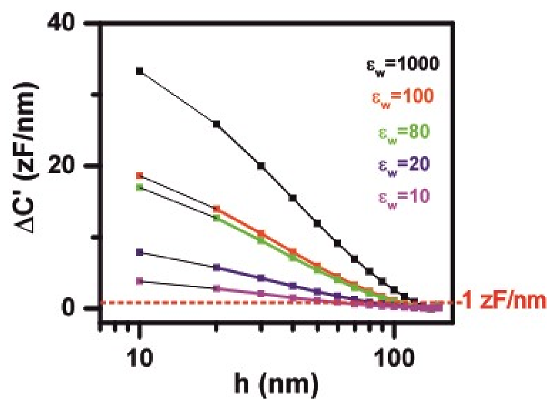

Figure 5.19. The difference in the capacitance gradient (contrast) is represented here with respect to the buried depth of the nanowire (h). This graph shows that deeper the nanowire is buried, lesser the signal this making it harder for us to identify them or differentiate them from the buried matrix. The relative permittivity of the wires is also varied to study its contrast variation with the buried depth, showing that higher the relative permittivity of wire (ε_w), higher the signal in a dielectric matrix.

Variation of dielectric constant/relative permittivities

a) Varying the nanowire dielectric constant ε_w

The dielectric constant of a material determines its polarizability. The relative permittivity is ε_r=1 for air, ε_r ~ 4 for a silicon dioxide, ~ 2 to 3 for polymeric materials and ε_r very large for a conductive material. In this current study, since we are using a metallic nanowire, we use a ε_r very large (~ 10^3). The variation of the capacitance gradient contrast with the relative permittiviy of the wire (ε_w) is shown in Fig 5.20(a). The results reiterates the importance of the relative permittivity of the buried substance for the subsurface characterization (especially, in providing contrast). When the dielectric constant of the wire matches with dielectric constant of the matrix (ε_w=ε_m=4), we see no contrast. As the ε_w increases, the increase in

capacitance gradient can be noted. When the ε_w is increased to be conductive (higher the ε_w), the highest the electric force felt by the tip. This force or capacitance gradient saturates for very large values. When the ε_w is smaller than that of the matrix ($\varepsilon_w < \varepsilon_m$), a negative contrast obtained (as seen in green line in Fig 5.20(a)). This might be an example of presence of air bubble inside the polymer matrix formed during sample preparation.

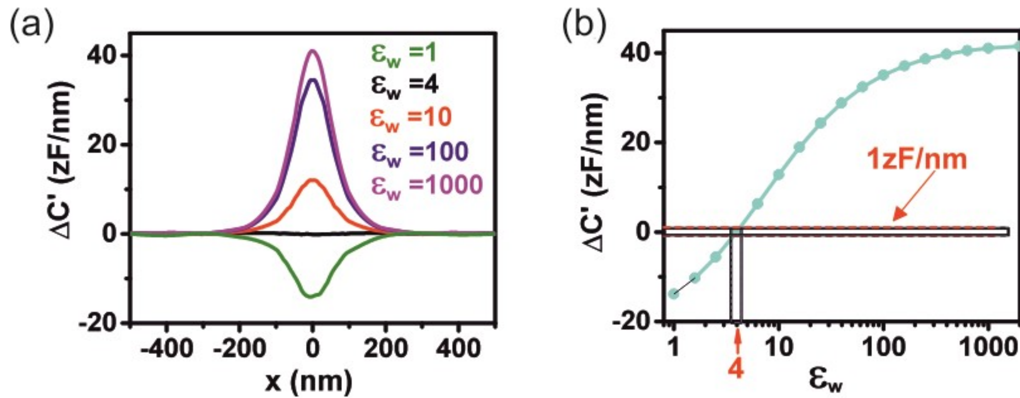

Figure 5.20. (a) Capacitance gradient profiles taken at a tip-sample distance z=20 nm for different ε_w (relative permittivity of the buried wire) while imaging the sub-surface wire in constant height. As we can observe higher permittivities of the wire produce higher signal thereby making it easier for subsurface characterization. (b) Change in capacitance (contrast of the experimental image) as a function of the relative permittivity of the wire. The straight lines in the graph represents when the permittivity of the wire matches with that of matrix providing no signal. The graph also marks the experimental noise range above which the signals are easily detected.

b) Varying the matrix dielectric constant ε_m

Similar to the experiment of changing the relative permittivity of the wire (ε_w), the dielectric constant of the matrix (ε_m) plays an influential role in determining the contrast in sub-surface imaging. The capacitance gradient contrast decreases as the matrix permittivity increases, as seen in Fig 5.21 for a metallic nanowire. As the ε_m increases and reaches high values (>100) the contrast decreases and drops below the exeperimental noise range. This proves that metallic nanowires are hard to be detected in materials with high dielectric constants, due to the screening of the electric fields.

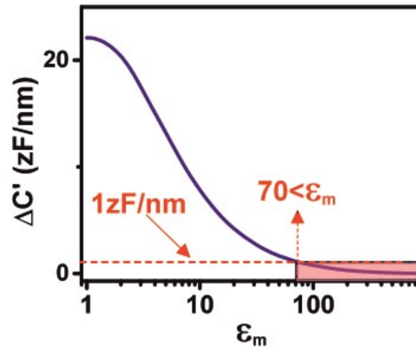

Figure 5.21. Capacitance gradient contrast maximum as a function of the relative permittivity of the matrix (ε_m) for a metallic nanowire ($\varepsilon_w=10^3$). As the ε_m is increased the contrast decreases and drops below the experiemtnal noise range. For the parameters used in this study, it is found that for a matrix permittivy higher than $\varepsilon_m=70$ it is harder to achieve contrast in subsurface imaging (pink rectangle). The red dashed line denotes the instrumental noise below which the signal cannot be interpreted experimentally.

Conclusion :

The numerical study of EFM applied to a single nanowire buried inside a dielectric matrix provided us with the best possible parametric relationships required for effective subsurface imaging. For example,

a) *The smallest tip-sample distance (z) gives the best electrical signal (provided the tip does not interact with the sample)*
b) *The radius of the probe (R) must be chosen such that it has a perfect balance between amount of electrical signal obtained and its ability to spatially resolve the buried entities.*
c) *There must be a difference in relative permittivity of the buried substance (here, ε_w) and the surrounding matrix (ε_m), in order to obtain the contrast. For metallic nanowires, the best contrast is achieved for low dielectric constant matrices.*

These obtained results should be translated during the experimental imaging to obtain the best possible characterization of sub-surface domains/entities.

Further numerical theoretical analysis closer to practical applications and their results can be found in the Chapter 7.

Chapter 6

Materials and Methods II: Silver nanowire gelatin nanocomposite preparation

This chapter contains the materials and methods followed in the preparation of the silver nanowire gelatin nanocomposite sample for experimental subsurface characterization. The sample preparation protocol, literature survey, the optimization procedures, and its characterization have been laid out in this chapter. I have carried out the sample preparation procedures along with profilometer and AFM characterization. The spin coating process and profilometer studies have been carried out in cleanroom to ensure non-contamination. The clean room facility and instruments have been provided and supported by the Nanotechnology platform of IBEC. I would also like to thank Dr. Adrica Kyndiah for consultation during the sample preparation procedures.

Introduction:

The preparation of the silver nanowire gelatin nanocomposite samples for subsurface characterization needs to satisfy some conditions as we have seen from the results of Chapter 5. Some of them include a) controlling the depth at which the entities are buried, b) minimizing topographical interference due to surface topographic variations, c) Controlling the change in relative permittivity and chemical composition of the materials during sample preparation and imaging, etc. Initially, dip coating was used for sample preparation, but the need for surface homogeneity kept us looking for better methods available. Since subsurface imaging is at its infancy, there have been relatively few publications, out of which some of them served as our starting point. Optimization and improvisation of existing methods have been carried out to attain our desired subsurface sample.

Literature survey:

We have surveyed few significant subsurface publications over the years[1,3,5,15–17,23,43,52,55, 62–67,69,115–117,5,118–121] in order to design the appropriate sample preparation method. The results of the survey have been tabulated in appendix Table (6.1). Out of these available methods, the methods that matched our requirements were spin coating. The spin coating has been sought as the most convenient technique, as it provides us the ability to control the matrix thickness. The optimization of the coating method concerning the concentration of the coating material, speed and acceleration of the coating, type of substrate for coating, time and temperature of coating has been carried and it is described in the following sections.

Spin coating sample preparation:

The spin coating process has been carried out in the cleanroom to ensure the maintenance of clean quality standards during the nanometric sample preparation. The instruments used in this sample preparation include Spin coater [Laurell Tech., WS-650MZ23NPP/LTE], Profilometer [Vecco Instruments, DEKTAK 6M], Hotplate [PSelecta, Platronic] and Vacuum chambers [Kartell Pvt. Ltd.]. The Graphite and Silicon substrates have been commercially obtained from MikroMash USA and Amo GmBH Nanofabrication, Germany, respectively. The Gelatin [Gelatin from Porcine Skin - Type A] has been procured from Sigma Aldrich. Silver nanowires (A50 Research Grade, 0.5g dissolved in 50 ml IsoPropyl Alcohol) are obtained from Novarials [Novawire-Ag-A50]. Various chemicals like Acetone (PanReac, Applichem) & 2- Propanol (Sigma Aldrich, ACS reagent) were also used in the course of the study. All the water used is MilliQ purified water by MilliPak Express 40. Nitrogen gas was used sporadically for drying purposes. The cleanroom facility and few of required instruments have been provided and supported by Nanotechnology platform at my research institute IBEC.

Optimization of parameters:

As mentioned above, the parameters to be optimized involves the substrate, concentration of the material to be buried (in this case, silver nanowires), method of drying of the first layer (nanowires), the primary method of coating the burying matrix (gelatin), the concentration of the burying matrix , speed of coating the second layer-matrix, temperature of the coating solution, mode of drying of the second layer and its effects. They are addressed in the following steps.

Step 1: Effect of substrate

Substrates for EFM characterization should be electrically conductive, to form a capacitor structure with the probe. Extending from the earlier works of the group [33,70], HOPG (Graphite) substrate was initially chosen for this experiment. Graphite substrate has the ability to be reused by cleaving the top layer, thus allowing it to be cleaned easily. This, somehow, proved to be a demerit when the thickness of the burying matrix had to be determined. The thickness or height determination is normally carried out by scratching the matrix thin film to measure by AFM or by piercing the top layer to be measured by a profilometer (similar to Fig 6.3 below). The problems associated with both the techniques included the cut/scratch reaching beneath the bottom layer. This led us to look for an alternative option that overcame this characteristic but also has the properties of substrate required for EFM imaging.

We selected highly doped silicon substrates (Si) that served as a perfect base for our requirements and from the following sections we could notice its compatibility and efficiency in our materials used in subsurface sample preparation.

Step 2: Effect of modes of drying of the first layer:

The first layer casted on the bare silicon substrate (Si) is our silver nanowires (AgNWs). Proper care should be taken to ensure that AgNWs are dried completely before coating the burying matrix. Overnight drying was considered initially inside a vacuum chamber. The 16 hours of overnight drying, when compared with the results of 4 hours drying, provided the same amount of drying. It was also found that the 4-hour drying can also even be improved when a combined effort of 2-hour drying and post-treatment with nitrogen gas. This nitrogen gas is considered as it can also help in cleaning the substrate with the first layer before taking them for matrix deposition.

Step 3: Effect of coating methods:

Initially, dip coating was one of the most convenient methods for the preparation of buried samples. The matrix material is the gelatin solution which is made by mixing gelatin powder in 90°C MilliQ at desired concentrations. The powder is dissolved by stirring and letting it cool down. The solution is reheated at 60-70 °C for coating purposes. The dried Si substrate, after being coated with nanowires, is dipped into the solution for ~2-3 seconds and they are vertically dried in such a way that there is no excess gelatin on the surface of Si substrate. The coated substrates are further dried under vacuum chamber for overnight before taken for characterization. When these substrates were analyzed with the help of a profilometer for the matrix thickness, it was observed that the inhomogeneity was of a higher degree (Fig 6.1). The surface thickness ranged from 600 nm to 20 nm, which is unfit for quantification.

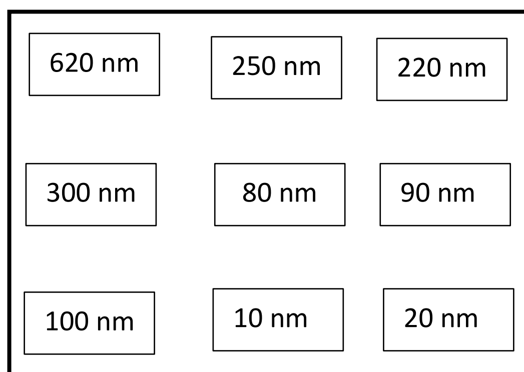

Figure 6.1. Schematic representation of the inhomogeneity in thickness of a sample prepared by dip coating. The thickness of the burying matrix ranges from 600 nm to 20 nm which is unfavorable for our quantification studies.

Based on the dip coating results and literature surveyed in appendix Table (6.1), the spin coating was chosen for sample preparation. Different speeds (please refer to step 5) and different concentrations of the matrix were tested (please refer to step 4) to also achieve this phenomenon. It was observed that spin coating could help in our required sample preparation. This provides sample homogeneity relative to the previous method with a smaller error range (Fig 6.2). By controlling the solvent concentration and speed, it was possible to achieve the required thickness of the burying matrix. Gelatin was chosen as the burying matrix as it provided us with the versatility of exploring different relative permittivities by considering both dry and humid states, for which it ranges from ε_r~5 to ε_r~14 (this can be further seen in Chapter 8). Gelatin also had the additional advantage since it is a material of biological origin, so it can help us in extrapolating this current work to application in different fields such as drug delivery, nanotoxicology and nanomedicine.

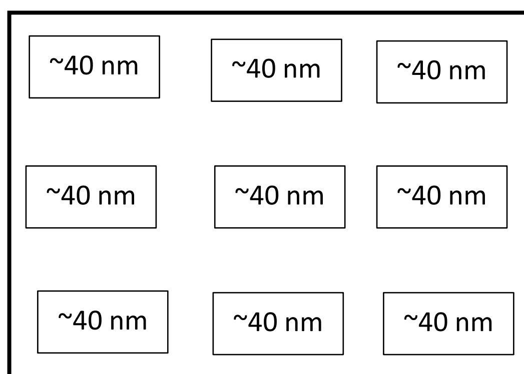

Figure 6.2. Schematic representation of the homogeneity in thickness of a sample prepared by spin coating.

Step 4: Effect of matrix concentration:

Changing the concentration of the solvent observed to cause a huge shift in the thickness of the matrix layer. The different concentrations used were ranging from 0.5g/100 ml to 10g/100 ml. When spin coated, different concentrations produced different results of matrix thickness. Understandably, increasing the concentration increases the thickness of the layer due to its change in viscosity. The nanowire coated highly doped Si substrate after coated with different concentration of gelatin is sharply cut perpendicularly after annealing like shown in the schematic Fig 6.3, in order to determine its thickness with the use of a profilometer.

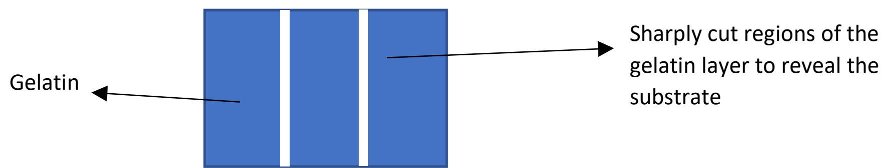

Figure 6.3. Samples prepared are cut in the schematic shown above in order to study the thickness by profilometer.

The profilometer consists of a sharp tip with radius 2.5 µm, which scans the cut surface perpendicularly and provides a profile which can be used to indicate the thickness of a thin layer. The profilometer provides the profile (or changes in the profile) while scanning the surface with the help of its probe. The profilometer snap shots of each concentration have been provided in Fig 6.4, which represents its thickness.

(a) 0.5g/100 ml Gelatin ~ 20-30 nm

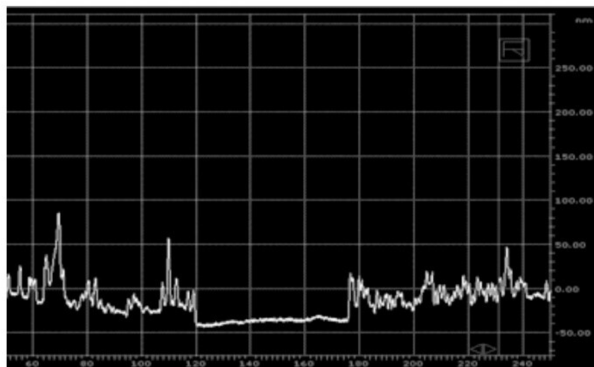

(b) 0.75g/100 ml Gelatin ~ 30-40 nm

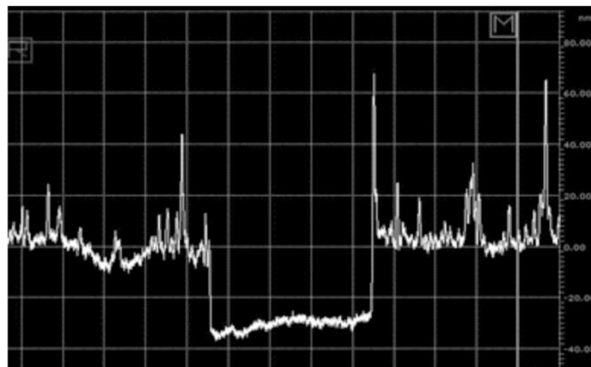

(c) 1g/100 ml Gelatin ~ 40-50 nm

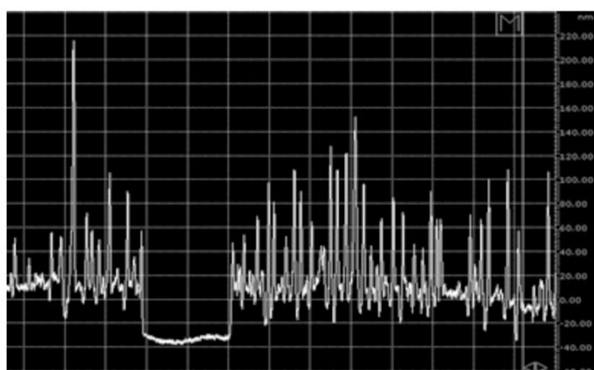

(d) 2g/100 ml Gelatin ~ 80-100 nm

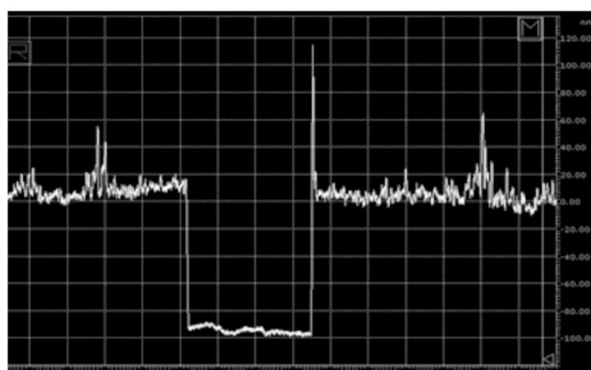

(e) 3g/100 ml Gelatin ~ 120-150 nm

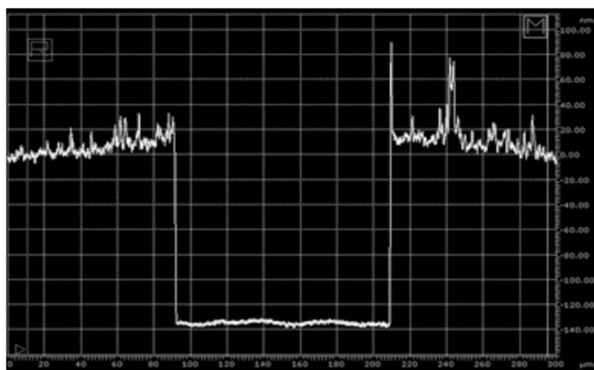

(f) 4g/100 ml Gelatin ~ 250 ± 50 nm

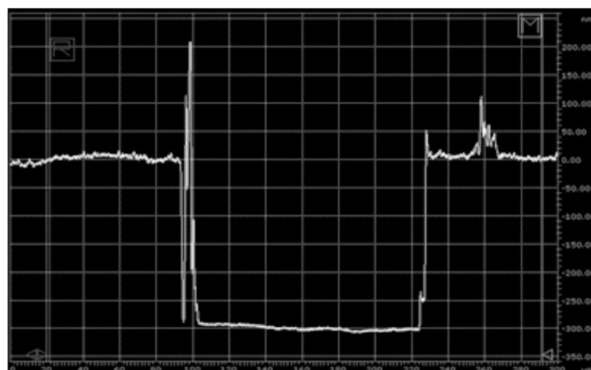

(g) 6g/100 ml Gelatin ~ 350 ± 50 nm

(h) 8g/100 ml Gelatin ~ 750 ± 70 nm

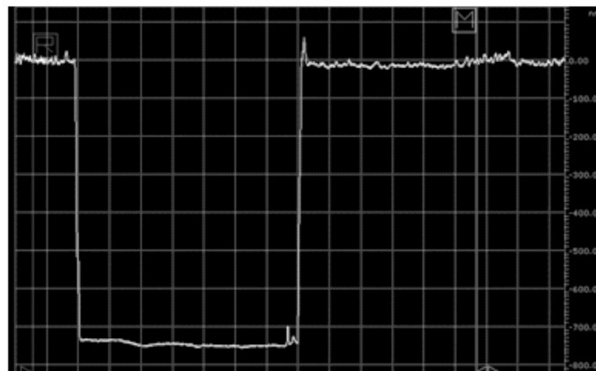

(i) 10g/100 ml Gelatin ~ 950 ± 70 nm

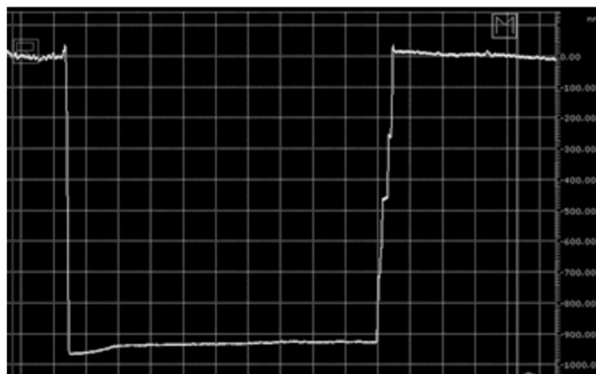

Figure 6.4. (a-i) Measurements from the profilometer estimating the thickness of the coated gelatin layer in varying concentrations from 0.5 g/100ml to 10 g/100 ml.

The thickness studies have been carried out for different concentration at a constant speed of 2000 RPM (please refer step 5) from 0.5 g/100 ml to 10 g/100 ml, which provided us with a database of varied thicknesses. These have been plotted with thickness respect to the concentration used in the optimization graph below (Fig 6.5). The advantage of this graph is that when we require a desired thickness, we could match it with the concentration of the matrix solution to prepare it.

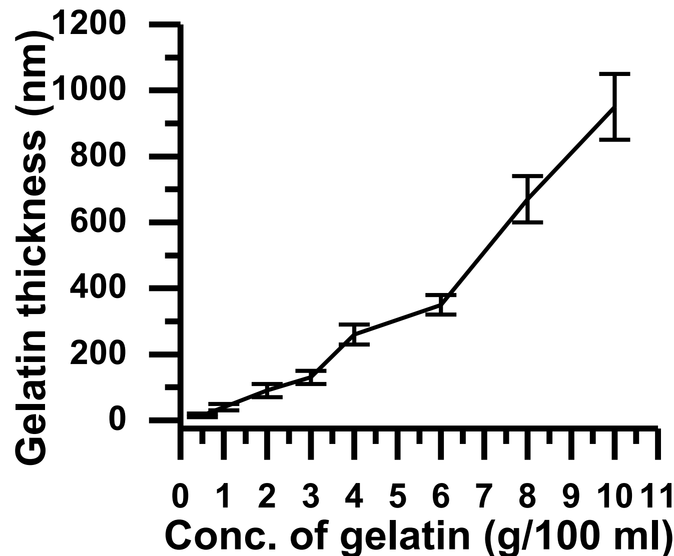

Figure 6.5. Graph showing the relationship between the concentration of gelatin and thickness of gelatin layer obtained on top of the substrate, determined with the profilometer.

Step 5: Effect of speed in spin coating

The thickness by spin coating is dependent on the speed and the concentration of the solvent (which can be observed from the previous section). The speed of the spin coating follows two steps:

a) Initial step:

When the solution is dropped in the middle of the substrate, the initial acceleration serves to spread the solution throughout the substrate and also to warm up the spinner for the next step with higher rotation velocities (RPMs). Normally this step is of low timeframe and in this case, it has been set as 1000 RPM for 10 seconds with 500 RPM acceleration.

b) Final step:

After initial spreading, this step is longer depending on the required thickness that follows the centrifugal motion to achieve the thinning of the films. This step has been studied with three different RPMs (1000, 2000, 3000) and the results are shown in profilometer snap shots in Fig 6.6.

i) 1000 RPM – Even though this speed helped to achieve the desired thickness, it was observed that the speed of 1000 RPM was not quite enough to spread the solution which is equal to acceleration RPM. This trait compromised the homogeneity of the layer at the edges of the substrate.

ii) 2000 RPM – This speed provided the perfect spreading and thinning of the gelatin solution, thereby helping us achieve the perfect balance and desired thickness of matrix layer.

ii) 3000 RPM – The higher speed of 3000 RPM provided ultra-thin layer due to high centrifugal force occurrence, which did not entirely bury the underlying nanowires.

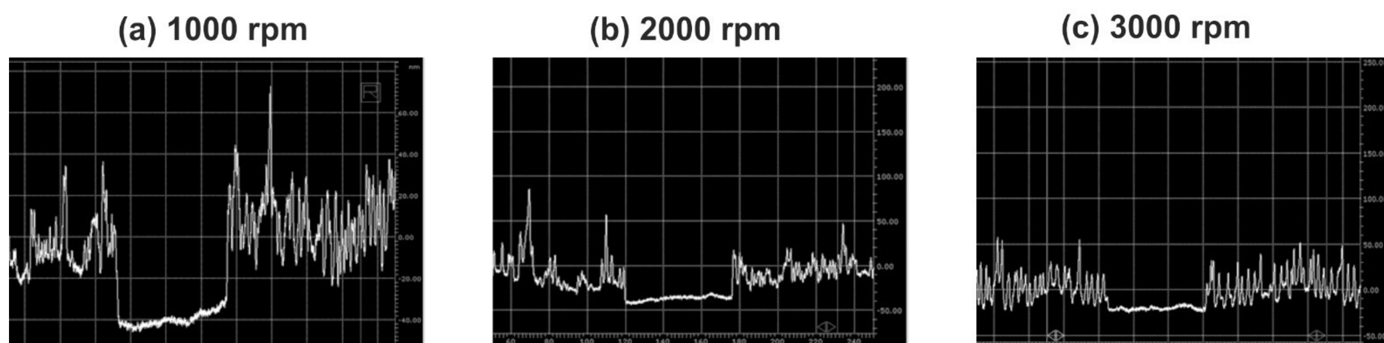

Figure 6.6. (a-c) Measurements from profilometer estimating the thickness with relation to varying speeds[rpm].

In conclusion, the speed of 2000 RPMs for 1 min with 1000 RPM acceleration for 30 seconds has been chosen for further experiments since it provided the thin film with required thickness.

Step 6: Effect of temperature

The temperature is also a significant player in the thickness of the matrix after coating. It is found that when the temperature increases, the gelatin adheres better on the doped Si substrate with nanowires. This characterstic can be attributed to the helix-coil transition temperature[122] property of gelatin, which exists in different forms with respect to the temperature. Below helix-coil transition temperature, the gelatin exists as a viscous solution that resembles a semi-solidified viscous gel. Above helix-coil transition temperature, the gelatin solution form transforms itself into liquid form which is easier for coating.

To test this theory, spin coating have been carried out with gelatin at room temperature (25-37 °C) and with gelatin at 60-70 °C. The profilometer results are shown in Fig 6.7 which indicates a) very little adhesion of gelatin at room tempature and b) better adhesion using the 'hot-cast' films of gelatin by showing a prominent profile when they are sharply cut perpendicular to the axis.

(a) Gelatin coated at room temperature

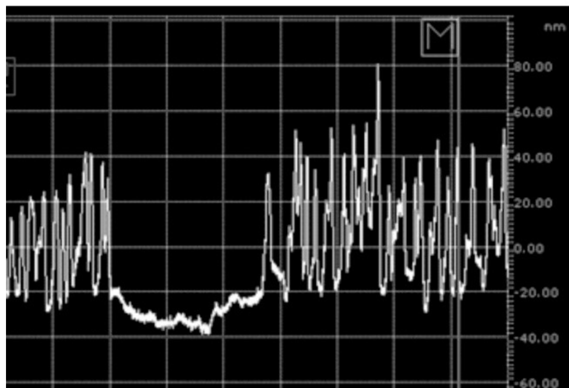

(b) Gelatin coated at 60-70°C

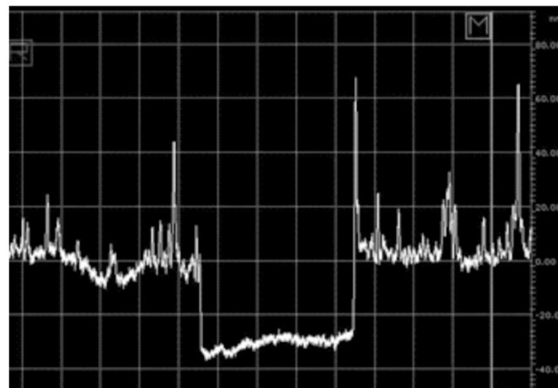

Figure 6.7. Measurements of profilometer estimating the thickness in relation to the tempature of the gelatin coated (a) at room temperature, (b) at 60-70 °C.

Step 7: Effect of drying methods of matrix:

Previously, for drying the matrix (gelatin) the substrates after coating the second layer are kept under a vacuum chamber for overnight. This, in turn, provided us less control over the homogeneity of the matrix during the process of drying. So, this process has been replaced by annealing the highly doped silicon substrates after spin coating. Annealing consists of heating the freshly coating Si substrates on a hotplate at 90-100 °C for 10 minutes. Annealing is believed to evaporate the solvent from the matrix solution (in this case, water) uniformly from the top layer of the substrate, thus resulting in homogenous layer with minimal error range.

To check the role of annealing in the thickness of the matrix layer, Si substrates were also prepared with and without annealing (not shown here). The non-annealed (drying by the older vacuum method after spin coating) and the annealed (drying in hotplate) provided the same thickness, showing that annealing does not play a role in influencing the thickness, rather has an effect of uniformity/homogeneity of the matrix layer.

Best sub-surface sample preparation method:

a) **Substrate**: Highly doped Silica substrate (Si)
b) **Cleaning**: Ultrasound cleansing using- Acetone (10 min), 2-Propanol (10 min) and MilliQ water.
Nitrogen air treatment for surface cleaning
c) **NW drying**: 2 hours drying in a vacuum chamber after coating,
Followed by Nitrogen air blown to dry and clean the sample.

d) **Gelatin**: 2g/4g in 100 ml of water, added at 60-70 °C and dissolved

e) **Coating Method**: Spin coating

f) **Coating speed**: a) 2000 RPM, 1 min, 1000 acc. [For coating]

b) 1000 RPM, 10 sec, 500 acc. [For spreading]

g) **Temperature**: Before coating, heating up to 60-70 °C

h) **Drying of gelatin**: Annealing at 90-100 °C for 10 minutes

Sample characterization

The characterization of the optimized sample preparation method is carried out. The silver nanowires are coated on a conductive Si-doped substrate. To observe their spread and distribution on the substrate, Scanning Electron Microscopy (SEM) imaging have been carried out. These images, shown in Fig. 6.9, are carried out in Nova NanoSEM FEI SEM using the detector LVD. Images have been obtained by applying a voltage of 10 kV, a current of 80 pA and a working distance of 4.7 mm. SEM images have been performed on AgNW samples prepared on a AFM/EFM/SEM custom-made finder grids[78].

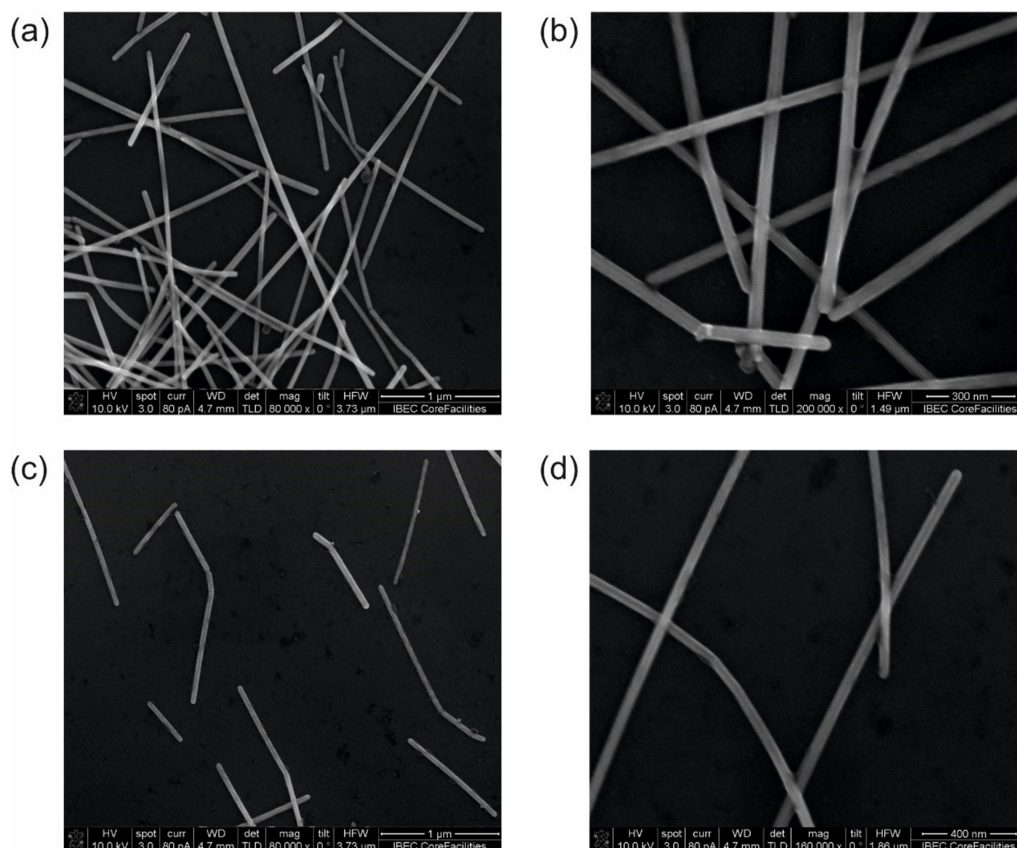

Figure 6.9 (a-d) SEM images of silver nanowires on a highly doped silicon substrate before gelatin coating. The SEM images were captured with *Nova NanoSEM FEI SEM using the detector LVD. Images have been obtained by applying a voltage of 10 kV, a current of 80 pA and a working distance of 4.7 mm.*

These AgNW coated Si-doped substrate have also been characterized by Atomic Force Microscopy (AFM) before the coating of the Gelatin. The AFM images can be seen in Fig 6.10, showing the distribution of the nanowires.

The custom-made grid finder (developed by Dr. H. Lozano and R. Millan from our research group[78]) helps us in identifying the nanowires and their location both before and after coating. In Fig 6.11, we can observe the grid made with Si-doped material and it is coated with AgNWs as per our optimized parameters. This grid can also help during cross characterization when a same position in the sample should be imaged in different instruments like SEM, AFM, and EFM. To demonstrate this, SEM with colored rectangles is seen in the image above, and they correspond to the images taken below in the AFM at the same position after gelatin coating. This also shows that there is minimal movement of nanowires before and after coating of the gelatin layer.

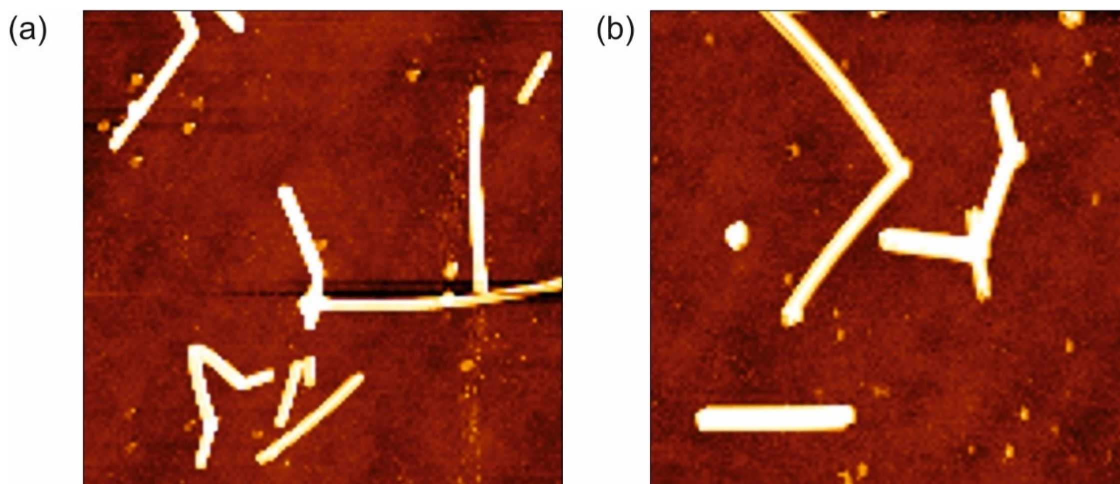

Fig 6.10. Topography images of silver nanowires on a highly doped silicon substrate before gelatin coating. The AFM used to image is Nanowizard 4 BioAFM from JPK and these images were taken in SDFVM mode as explained in Chapter 3.

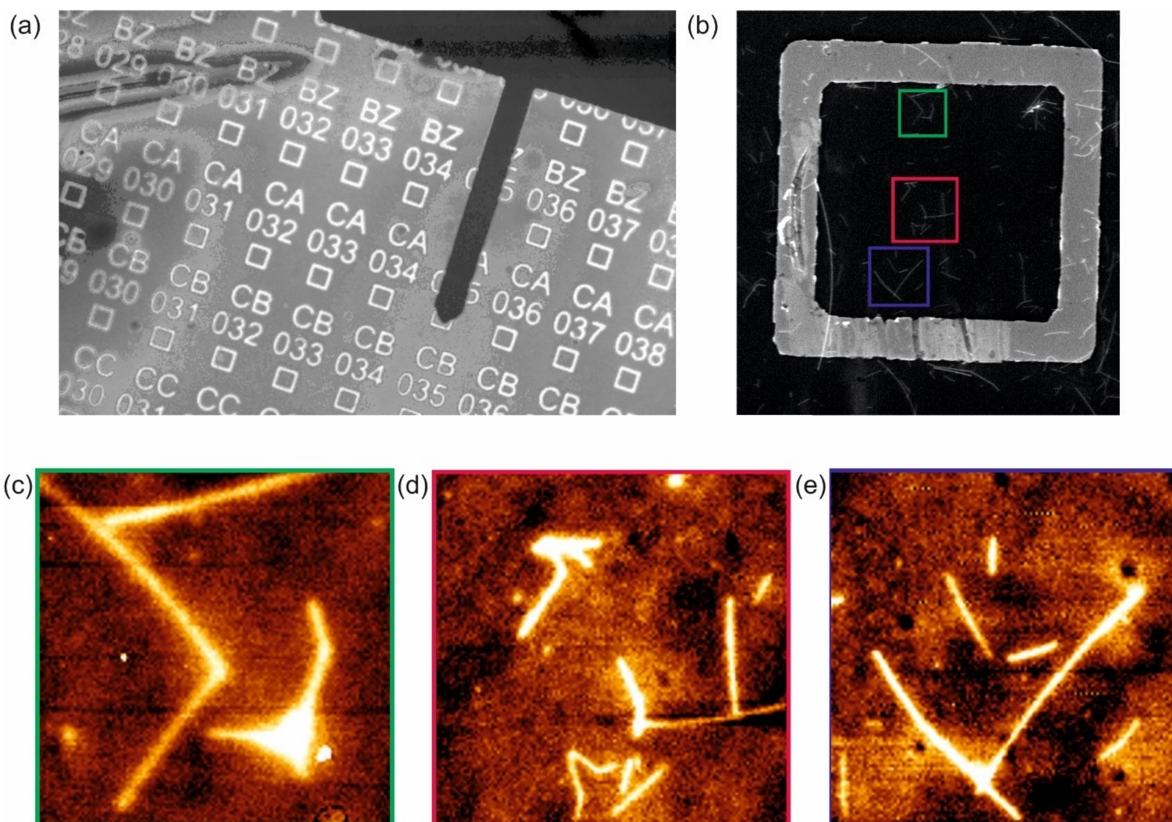

Fig 6.11. (a) Photograph of an AFM cantilever on the customized grid for easier characterization of nanowires before and after gelatin coating. (b) SEM image of one of the squares observed in (a). The colored squares in the (b) correspond to the color bordered AFM topography images taken after coating in the same location as shown in SEM image (c-e).This shows that there is no or minimal lateral movement of nanowires before and after gelatin coating.

The AFM used to image is Nanowizard 4 BioAFM from JPK and these images were taken in SDFVM mode as explained in Chapter 3.

Additionally, to ensure the coating of gelatin and burial of nanowires, AFM topography have been carried out in the same location before and after coating. In Fig 6.12, we can observe the respective AFM images and the topography profile graph showing the peaks. The peaks after coating are less prominent in the topography which confirms that the nanowires are buried. The observed peaks are protrusions of the wire buried inside the gelatin matrix that are visible in topography (this will be further discussed in Chapter 8).

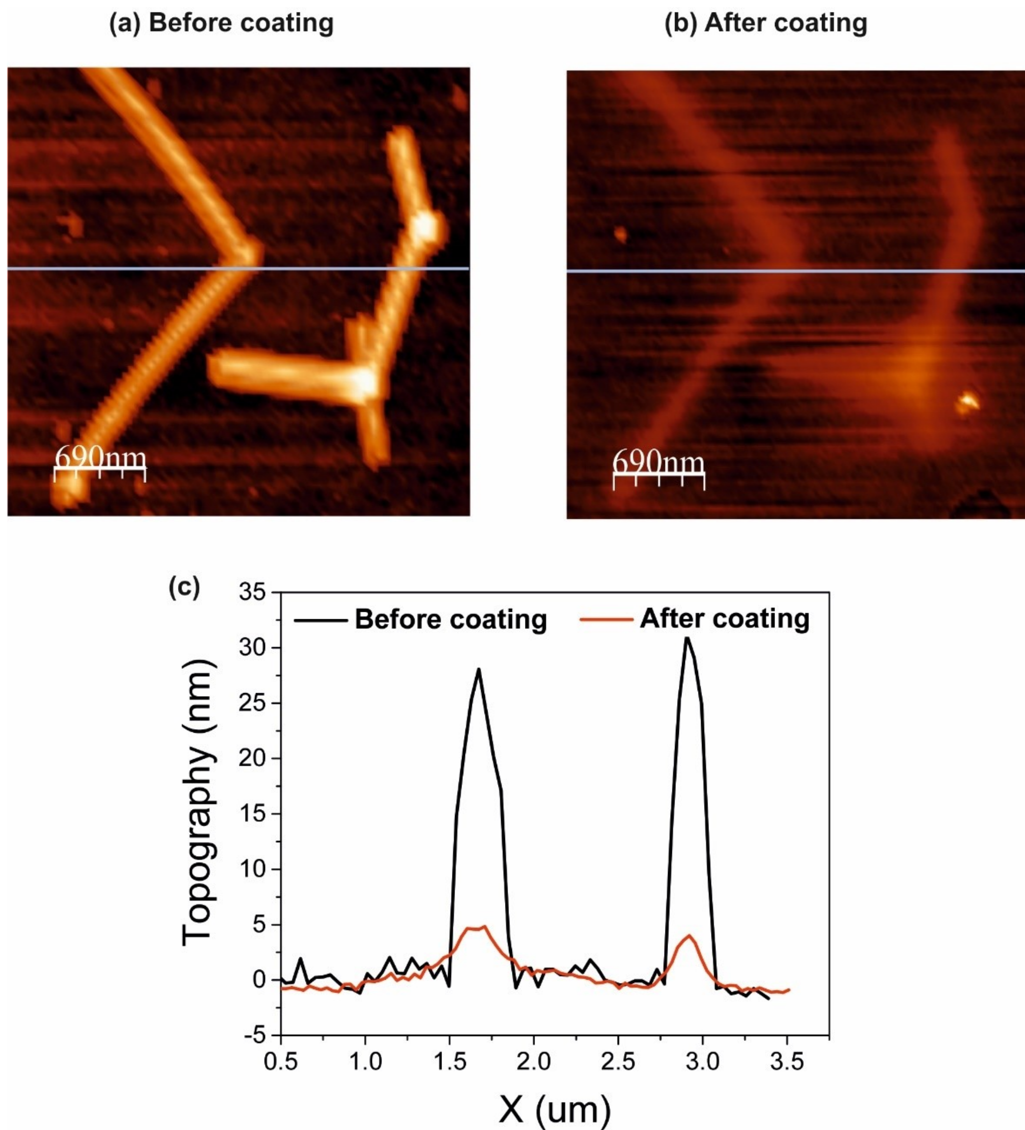

Fig 6.12. Topography AFM images of silver nanowires taken (a) before and (b) after coating of gelatin and (c) their respective topographical profiles in the graph plotted. The AFM used to image is Nanowizard 4 BioAFM from JPK and these images were taken in SDFVM mode as explained in Chapter 3.

Conclusion:

The silver nanowire gelatin sample preparation method has been implemented and optimized by following the spin coating for subsurface characterization. Through this process, the matrix thickness can be varied depending on our requirements. The long conventional process has been optimized to prepare homogenous layers of required thickness using this process rapidly. The optimized properties of the prepared samples have been verified before and after gelatin coating using SEM and AFM characterization, thus providing us with definite results of obtaining nanoscale samples for subsurface characterization.

Appendix:

Table 6.1. Methods of subsurface sample preparation in literature

S.No.	Title of the paper	Sample	Sample preparation
1.	Nanoscale Imaging of Buried Structures via Scanning Near-Field Ultrasound Holography - G. S. Shekhawat et al.	a) Polymer-nanoparticle composite b) Malaria parasites in RBC	Colloidal dispersion In vitro culture
2.	New modes for subsurface atomic force microscopy through nanomechanical coupling - L. Tetard et. al.	Fresh poplar wood	Microtoming
3.	Subsurface imaging of silicon nanowire circuits and iron oxide nanoparticles with sub-10 nm spatial resolution - A. P. Perrino et. al.	Silicon nanowire devices buried under an ultrathin polymer PDMS film	Drop casting Spin coating (30 nm to 60 nm)
4.	Subsurface Imaging of Soft Polymeric Materials with Nanoscale Resolution - E.C. Spitzer et. al.	Polystyrene cylinders, which are aligned parallel to the Si substrate surface and embedded in a polybutadiene matrix	Spin coating on silicon substrate
5.	Mapping the subsurface composition of organic films by electric force microscopy - H. Takano et. al.	Patterned thiolate monolayer on gold	Microcontact printing, Solution deposition of thiol

6.	Mapping of individual carbon nanotubes in polymer/nanotube composites using electrostatic force microscopy - T. S. Jespersen et. al.	poly-methylmethacrylate/SWCNT composite	Spin coating
7.	Batch-fabricated cantilever probes with electrical shielding for nanoscale dielectric and conductivity imaging - Y. Yang et. al.	Selectively doped Si sample, Polished Al_2O_3/SiO_2 sample	Sputtering, Mechanical polishing
8.	Quantitative sub-surface and non-contact imaging using scanning microwave microscopy - G. Gramse et. al	Flat doped silicon (Si) sample, epitaxially grown multilayer Si	PECVD (Plasma enhanced chemical vapour deposition)
9.	Seeing through Walls at the Nanoscale: Microwave Microscopy of Enclosed Objects and Processes in Liquids - A. Tselev et.al	Dry active Saccharomyces cerevisiae yeasts cells	Drop-casting on substrate
10.	Recovery of permittivity and depth from near-field data as a step toward infrared nanotomography - A. A. Govyadinov et.al.	PMMA was spin-coated onto a standard Si substrate	Spin coating, E-Beam lithography
11.	Subsurface characterization of carbon nanotubes in polymer composites via quantitative electric force	Single-wall carbon nanotube (SWCNT)–polyimide nanocomposite films	In-situ polymerization

	microscopy – M. Zhao et.al.		
12.	Sub-surface imaging of carbon nanotube-polymer composites using dynamic AFM methods – M.J.Cadena et. al	PI–SWNT nanocomposites	In-situ polymerization (Cast on glass plates and thermally imidized)
13.	Sub-surface imaging of carbon nanotube networks in polymers with DC-biased multifrequency dynamic atomic force microscopy – H.T.Thompson et.al	Polymer–CNT composite	CVD, Spin Coating
14.	Depth sensitive sub-surface imaging of polymer nanocomposites using second harmonic kelvin probe force microscopy – O.A.Castañeda-Uribe	SWCNT/Polyimide (PI) nanocomposite films	Spin coating
15.	Imaging latex-carbon nanotube composites by subsurface electrostatic force microscopy – S.Patel et.al.	CNT/PVDF composite	Latex blend
16.	High resolution subsurface imaging using resonance-enhanced detection in 2nd-harmonic KPFM – M.Cadena et.al.	Polymer- Nanoparticle composite	Electrophoresis, chemical reduction, Polymer blend coating

17.	Local organization of graphene network inside Graphene/polymer composites - A. Alekseev et. al	Graphene/PS Composite	Latex technology
18.	Monitoring chemical transformations at buried organic interfaces by electrostatic force microscopy - H. Takano et.al	Polystyrene/BASED/gold composite	Thiol mediated binding and spin coating
19.	Quantitative subsurface contact resonance force microscopy of model polumer nanocomposites - J. P. Killgore et.al.	Si NPs sandwiched between polymer(PS) layer sandwich	Spin coating and annealing
20.	Local Dielectric Property Detection of the Interface between Nanoparticle and Polymer in Nanocomposite Dielectrics – S. Peng et.al.	TiO_2 nanoparticles in Polyethylene matrix	Compression molding
21.	Imaging nanoparticles in cells by nanomechanical holography – L.Tetard et.al.	Mice cells with Single Walled Carbon Nanohorns	Centrifuged and fixed with methanol
22.	Subsurface imaging of silicon nanowire circuits and iron oxide nanoparticles with sub-10 nm spatial resolution – A. P. Perrino et.al.	Silicon nanowire devices buried under an ultrathin polymer film	Pattern transfer by dry etching processing. Spin coating of PDMS on Si NWs.

23.	Nondestructive imaging of atomically thin nanostructures buried in silicon – G.Gramse et.al.	Buried phosphorus nanostructures formed by incorporation and encapsulation of substitutional P atoms within multiple layers in a Si crystal	Surface hydrogen passivation
24.	Subsurface imaging of metal lines embedded in a dielectric with a scanning microwave microscope - L. You et.al.	Al–Si–Cu metal lines embedded in silicon dioxide film	Plasma deposition, chemical-mechanical polishing, etch back process
25.	Anomalously low dielectric constant of confined water – L. Fumagalli et.al.	Si substrate, hBN layer	E-beam lithography, Reactive ion etching, Annealing

Chapter 7

Spatial Resolution and Capacitive Coupling in Nanowire Nanocomposites Characterized by Scanning Dielectric Microscopy

Once the numerical calculations methodology has been optimized (as seen in Chapter 5), we proceed to present its application to study of buried nanowires in thin film dielectric matrices by Scanning Dielectric Microscopy. In particular, we address one problem that has not been discussed in the current literature, namely, the spatial resolution achievable in the sub-surface characterization of nanowire-based nanocomposites with scanning dielectric microscopy. The results presented in this chapter reproduce almost entirely the article entitled "Spatial Resolution and Capacitive Coupling in Nanowire Nanocomposites Characterized by Scanning Dielectric Microscopy" by Harishankar Balakrishnan, Rene Fabregas Ruben Millan-Solsona, Laura Fumagalli and Gabriel Gomila, submitted for publication. In this work, Dr. R. Fabregas and myself built the COMSOL models. Numerical calculations have been carried out by me and the results have been analyzed by me and Dr. Fabregas in collaboration with Dr. G. Gomila. The article has been written in collaboration with Dr. G. Gomila and the rest of authors.

Abstract:

As we have mentioned in Chapter 4, nanocomposite materials composed of nanowires are being developed for their use as transparent and flexible electrodes, or as stretchable conductors and dielectrics for biosensing. Here we investigate the use of Scanning Dielectric Microscopy (SDM) to characterize these materials in a non-destructive way, with a special focus on the achievable spatial resolution and the possibility to detect the capacitive coupling between neighbouring nanowires. We initially demonstrated that the nanowires spread function consists of a modified Lorentzian with a cubic decay. Following that, we have shown that the spatial resolution can be defined with the help of this function and noted how it depends on the different system parameters. For nanowires with diameter 50 nm, a spatial resolution below 100 nm is easily achievable when the nanowires are shallow buried. In this case, the spatial resolution increases when a system parameter either decreases the maximum of the nanowire spread function or increases its width. These results are validated with multiple nanowire numerical calculations. These same calculations are also used to demonstrate that SDM is sensitive to the capacitive coupling between nearby nanowires, which happens for separations below the diameter of the nanowires. This latter result is of utmost relevance since the electric interaction between nanowires largely determine the macroscopic electrical properties of nanowire nanocomposites. Present results show that SDM can be a valuable non-destructive subsurface

characterization technique for nanowire nanocomposites, which could impact the development of novel materials for applications in fields such wearable electronics, solar cell technologies and photonics.

Introduction:

We have already seen in Chapter 4, that the use of nanowires as fillers in polymer nanocomposites can lead to materials with exceptional optical, electrical, mechanical, and thermal properties. Due to the high aspect-ratio of the nanowires, small amounts of nanowires can largely modify some physical properties of the polymeric matrix (e.g. conductivity[80], dielectric constant[82] or thermal conductivity[83]), while retaining others almost intact (e.g. transparency, flexibility or stretchability). This property enables developing new materials possessing combined properties (e.g., high dielectric constant and stretchability, conductivity, and transparency, etc.) that are not available in single-component materials. Applications of these novel materials include transparent electrodes for solar cell applications[100,101] , flexible electrodes for wearable electronics[98,99], and high dielectric constant or conductive stretchable materials for pressure and motion sensors[97,102]. Nanowire nanocomposite materials also offer the advantage of being solution processable[103,104] or printable[105,106].

We have also mentioned that the macroscopic physical properties of nanowire nanocomposites depend critically on the distribution of the nanowires within the polymer matrix, and, specifically, on their relative distance. In order to determine these properties nanoscale tomographic techniques, such as those based on Electron Microscopy or X-Ray Microscopy, are necessary[12,14,123]. In practice, not many reports exists on the application of these nanotomographic techniques on nanowire composite materials[124], due to their inherent difficulty when applied to polymeric materials. For this reason, alternative nanotomographic techniques are under investigation, mostly based on sub-surface sensitive Scanning Probe Microscopy (SPM) techniques[8,125]. Techniques such as Scanning Near Field Ultrasound Holography[4,23], Mode Synthesizing Atomic Force Microscopy[55] , Multimodal AFM[52], Amplitude Modulated AFM[117] , Electrostatic Force Microscopy[62,119], Scanning Microwave Impedance Microscopy[3,118,121] or Scanning Near Field Optical Microscopy[115] , have all shown sub-surface nanoscale imaging capabilities in polymeric nanocomposite materials.

As described in *Section 3.3*, Electrostatic Force Microscopy (EFM) is one of the sub-surface SPM techniques that has experienced more progress towards its implementation as a nanotomographic technique

for polymeric nanocomposite materials[38,62,63,67,69]. We remind that sub-surface EFM imaging is based on the long-range nature of the electric forces, which can sense the presence and position of nanoscale objects buried within a polymeric material. Examples of EFM sub-surface imaging includes the detection of carbon nanotubes[15–17,62,63,65,67] , graphene networks[64] and nanoparticles[66] in polymer nanocomposites, or of buried water channels in 2D materials heterostructures[69]. The nanotomographic capabilities of EFM applied to nanowire nanocomposites have not been specifically analyzed. Some theoretical studies have been reported for the case of nanoparticle, carbon nanotube and thin-film nanocomposites[38,62,63,126,127] , but they have not addressed some key aspects relevant for nanowires nanocomposites, such as the achievable spatial resolution or the possibility to detect the capacitive coupling between nearby nanowires. Here, we develop a numerical approach to specifically investigate these aspects and demonstrate that EFM can be a valuable nanotechnique for the non-destructive characterization of nanowire nanocomposites.

Results

7.1. Nanowires capacitance gradient spread function:

As already noted in Chapter 3, EFM consists of an ac potential applied between a conducting AFM probe and the sample, and the ac electric force acting on the tip is measured. To analyze the electric force acting on the tip due to its interaction with an isolated buried nanowire we have considered the same model as the one described in chapter 5, shown in Fig. 7.1(a) for easier reference (not to scale). The nanowire is assumed to be cylindrical with diameter D_w and length l_w and be made of a lossless dielectric material with dielectric constant ε_w (metallic nanowires are modelled by setting $\varepsilon_w > 10^4$).

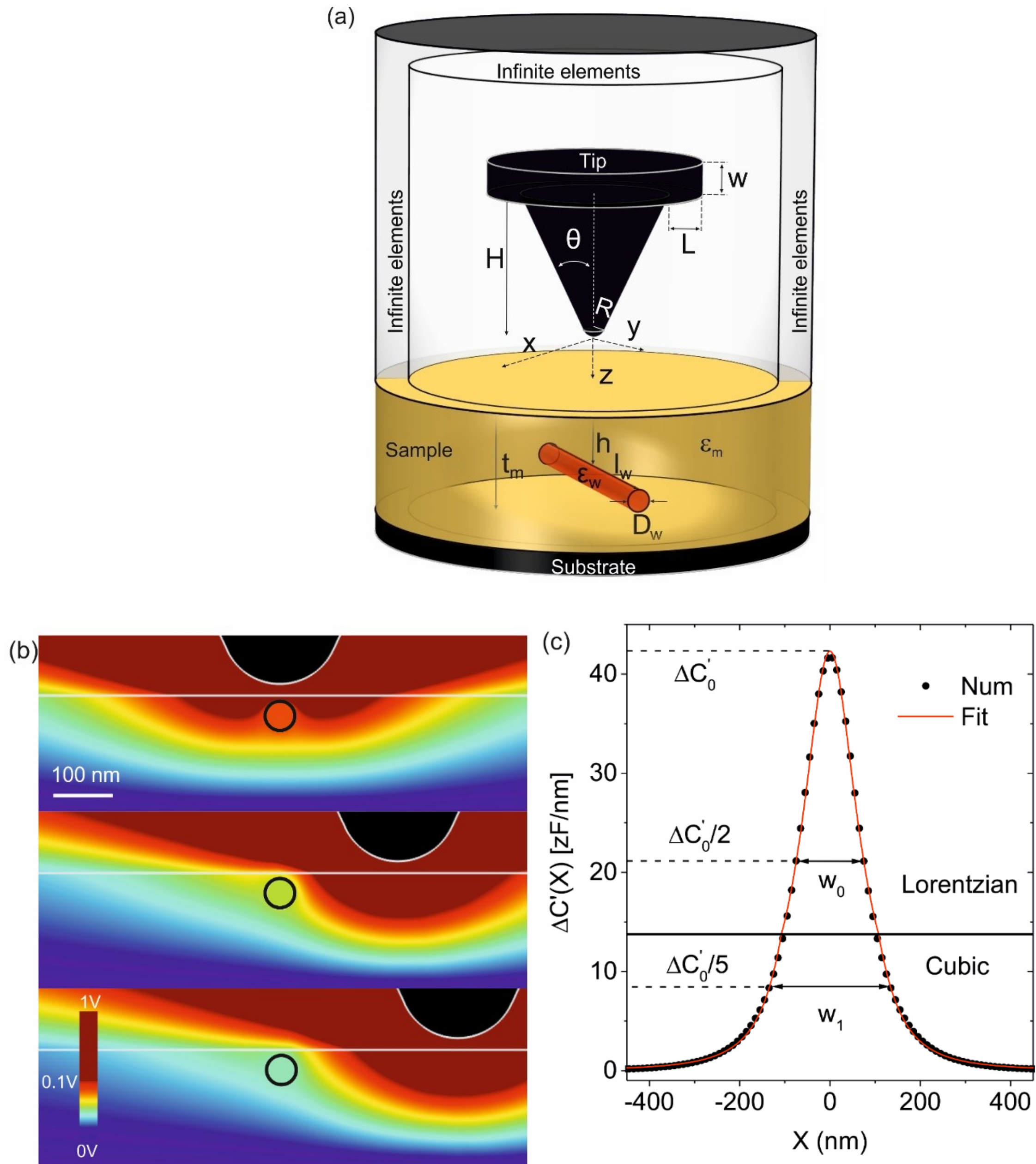

Figure 7.1. (a) Schematic representation of the isolated buried nanowire model, with the relevant parameters indicated. (b) Electric potential distribution across a cross-section of the sample for the tip at three different positions, X=0 nm, 100 nm, and 200 nm. Parameters of the calculations: D_w=50 nm, l_w=1 mm, $\varepsilon_w=10^4$ (metallic), h=10 nm, t_m=210 nm, ε_m=4, R=100 nm, θ=25º, H=12.5 mm, W=3 mm, L=0 mm, z=20 nm. (c) (symbols) Capacitance gradient (electric force) contrast profile ΔC'(X) at z=20 nm. (continuous red line) Fit to the numerically calculated profile with the modified Lorentzian function in Eq. (7.1). The fitted parameters are here $\Delta C'_0$=42.3±0.1 zF/nm, w_0=149.5±0.8 nm and w_2=268±1 nm.

The matrix of the nanocomposite material has thickness t_m and dielectric constant ε_m. The nanowire is located at a depth h measured from the matrix surface to the upper surface of the nanowire. As described in chapter 5 and earlier works[33,34,75] the probe consists of a conical tip of half angle θ and height H, ended

by a tangent sphere of radius R and capped at the top with a disc cantilever of thickness W and radius (H $\tan\theta$+L). Finally, the tip is located at a distance z from the matrix surface. Figure 7.1(b) shows the electric potential distribution along a cross-section of the sample for three positions of the tip during a scan over the nanowire (X = 0 nm, 100 nm, and 200 nm). All calculations have been done by using the electrostatic module of COMSOL MULTIPHYSICS 5.4 following similar methods to the ones described in chapter 5 and in Refs.[38,78,114] . The nanowire is assumed to be metallic with diameter D_w=50 nm buried at a depth h=10 nm in a matrix of thickness t_m=210 nm and with dielectric constant ε_m=4. The tip-sample distance and the tip radius are z=20 nm and R=100 nm, respectively (for the rest of tip parameters see Fig. 7.1 caption). The electric potential distribution changes significantly when the tip passes over the nanowire. So will the electric force acting on the tip, thus indicating that the tip can feel the presence of the buried nanowire. Figure 7.1c (symbols) shows the calculated electrical force acting on the tip (represented by the tip-sample capacitance gradient, dC/dz[33]) as a function of the lateral position of the tip. The upper part of the capacitance gradient contrast profile, ΔC'(X), shows a Lorentzian shape, like for carbon nanotubes[128], but the lower part decays faster (cubic decay). To account for these two behaviors the nanowire spread function has been defined by a modified Lorentzian function with a cubic decay:

$$\Delta C'(\mathrm{x}) = \begin{cases} \dfrac{\Delta C'_0}{4\left[\dfrac{X}{w_0}\right]^2+1} ; 0 \le |X| \le \dfrac{w_1^3}{8w_0^2} \\ \dfrac{\Delta C'_0}{4\left[\dfrac{2|X|}{w_1}\right]^3+1} ; \dfrac{w_1^3}{8w_0^2} \le |X| \end{cases} \tag{7.1}$$

Here, $\Delta C'_0$ is the maximum contrast of the ΔC'(X) profile, w_0 the full width at half maximum and w_1 the full width at one-fifth of the maximum. The red line in Fig. 7.1(c) corresponds to a least square fitting of Eq. (7.1) to the numerically calculated profile, giving ,in this case $\Delta C'_0$=42.3 ± 0.1 zF/nm, w_0=149.5 ± 0.8 nm and w_2=268 ± 1 nm. The agreement between Eq. (7.1) and the numerically calculated profile is almost perfect. Therefore, Eq. (7.1) can be used to simply parametrize the electrostatic interaction between the tip and a buried nanowire in SDM.

Figure 7.2(a-e) (symbols) show calculated ΔC'(X) profiles corresponding to varying, respectively, the tip sample distance, z, the tip radius, R, the dielectric constant of the matrix, ε_m, the depth of the nanowire,

h, and dielectric constant of the nanowire, ε_w. The continuous lines in Figs. 7.2(a-e) represent fitted curves by using Eq. (7.1). The agreement is excellent in all situations. Figure 7.2(e-h) show the dependence of the fitted parameters of the nanowire spread function ($\Delta C'_0$, w_0 and w_1) as a function of the corresponding system parameter. The maximum contrast, $\Delta C'_0$, is observed to decrease as a function of both the tip-sample distance and depth position of the nanowire following a rational function of the form $\Delta C'_0(x) = a(1+bx)/(1+cx+dx^2)$ (continuous lines in Fig. 7.2(f-g), although with different coefficients. This type of decaying is similar to that observed for (non-buried) nanoparticles[33]. At distances $z > 100$ nm or depths $h > 150$ nm the tip practically does not sense the presence of the nanowire anymore. Moreover, $\Delta C'_0$ increases linearly with the tip radius, ~R (Fig. 7.2(h)); it shows a maximum as a function of the matrix dielectric constant at $\varepsilon_m \sim 4$ and then decreases nearly logarithmically with ε_m, $\sim \log(\varepsilon_m)$, until it approaches ~ 0 for $\varepsilon_m > 100$ (Fig. 7.2(i)). It increases logarithmically with ε_w, $\sim \log(\varepsilon_w)$ for $\varepsilon_w < 10$ and then saturates to a constant value for $\varepsilon_w > 10^4$, which corresponds to the "metallic" limit (Fig. 7.2(j)). Concerning the widths w_0 and w_1, they present a similar behavior. First, they increase (profile broadening) as the tip sample distance or depth increase (Fig. 7.2(f-g)). Moreover, they increase as the tip radius increases (tip convolution) (Fig. 7.2(h)). Finally, they are relatively insensitive to the permittivity of the matrix and of the nanowire (Fig. 7.2(i-j)).

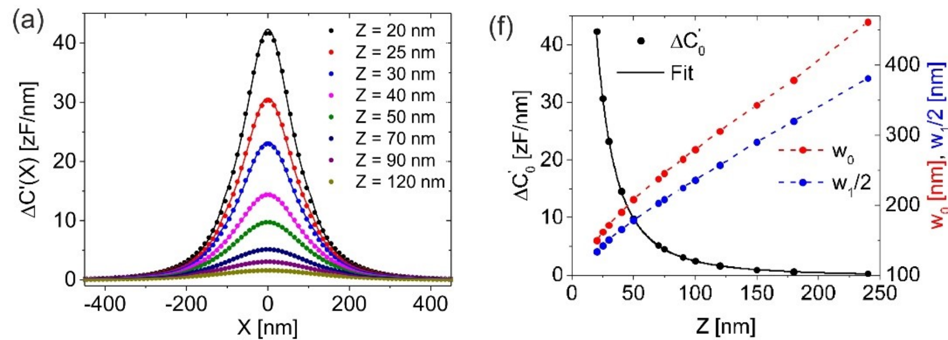

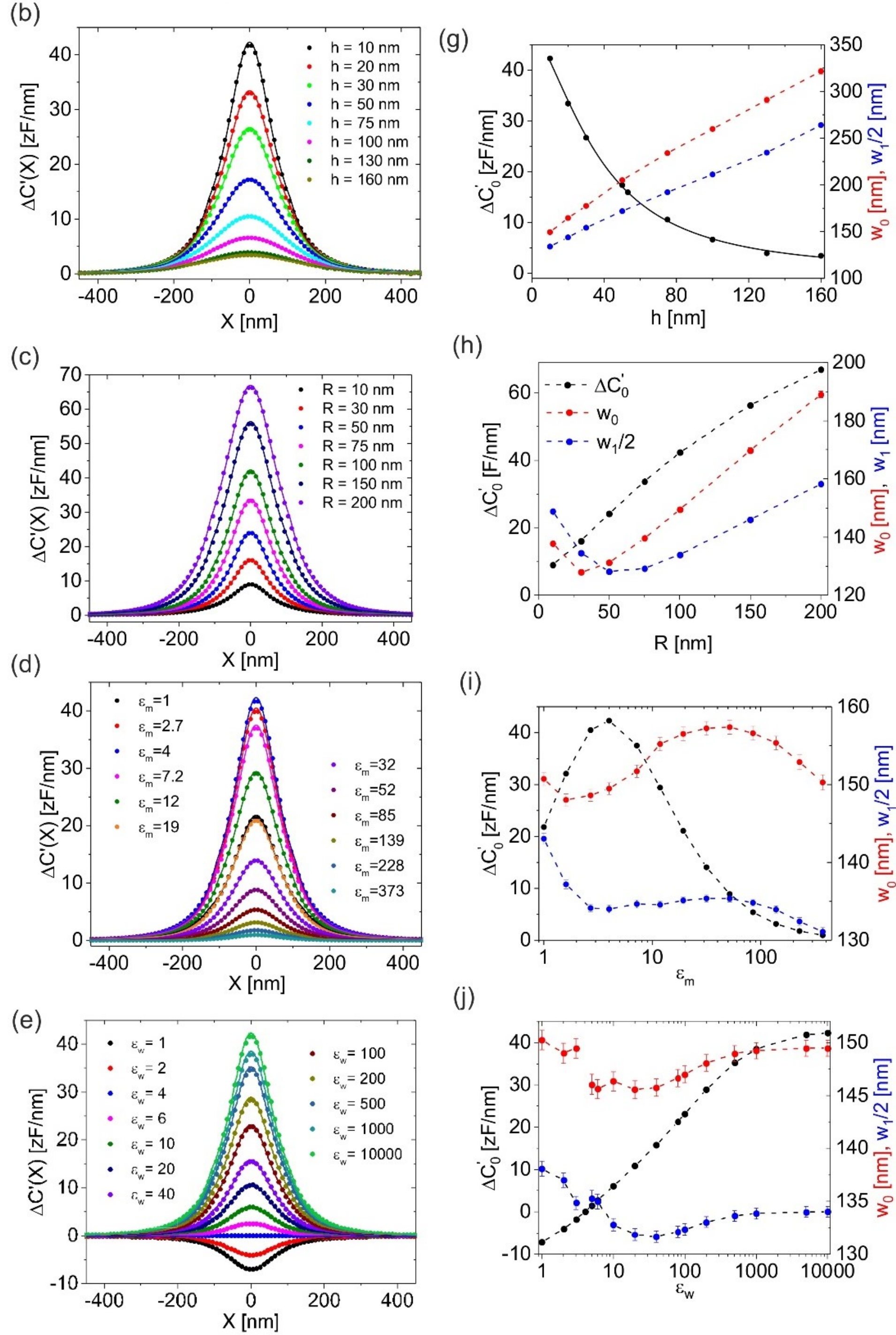

Figure 7.2. (a)-(e) Constant height $\Delta C'(X)$ profiles at a tip-sample distance z=20 nm for different tip-sample distance, z, depth, h, tip radius, R, matrix dielectric constant, ε_m, and nanowire dielectric constant, ε_w, respectively. Symbols correspond to the numerical calculations and the lines to least-square fittings with the nanowire spread function in Eq. (7.1). Parameters of the calculations, if not otherwise stated, same as in Fig. 7.1. (f)-(j) Dependence of the fitted parameters ($\Delta C'_0$, w_0 and w_1) on the tip-sample distance, depth, tip radius, dielectric constant of the matrix and dielectric constant of the nanowire, respectively. The error bars represent the standard deviation of the fitted parameter. In (f) and (g) the continuous lines represent a phenomenological fit with a rational function of the

form $f(x)=a(1+bx)/(1+cx+dx^2)$*. The fitted parameters are a=166 zF/nm, b= -2.4·10⁻³ nm⁻¹, c=48·10⁻³ nm⁻¹ and d=45·10⁻³ nm⁻² in (f) and a=48 zF/nm, b=6.0·10⁻⁴ nm⁻¹, c=11·10⁻³ nm⁻¹, d=0.5·10⁻³ nm⁻², in (g).*

7.2. Spatial resolution for parallel wires :

To investigate the achievable spatial resolution, we have built a model like the one in Fig. 7.1(a) but including two parallel nanowires. Fig. 7.3(a-d) show EFM constant height images calculated for two nanowires buried at a depth $h_1 = h_2 = 10$ nm and separated distances d_w=600 nm, 200 nm, 100 nm, and 40 nm, respectively (the distances are measured from edge to edge). The parameters defining the nanowire, matrix and tip are the same as before, as in Fig. 7.1. For relatively large separations ($d_w > 100$ nm, Figs. 7.3(a-c)) the two nanowires can be well resolved in the images (see also cross-section profiles, symbols, in Fig. 7.3(e-g)). However, at a separation somewhere between ~100 nm and ~40 nm (Fig. 7.3(d) and 7.3(h), symbols) the two nanowires are no longer resolved. In order to determine theoretically the separation at which this happens one could perform calculations at more separations until the critical separation is determined. This approach is time and computationally very expensive. One can design a much less costly approach based on the knowledge of nanowire spread function (Eq. (7.1)). Indeed, the two-nanowire cross-section profiles ΔC'(X) (symbols in Fig. 7.3(e-h)) can be reasonably well approximated by the sum of the two nanowire spread functions (continuous red line in Fig. 7.3(e-h))

$$\Delta C_{2\omega}'(X,d_w) = \Delta C'\left[X - \frac{d_w}{2} - R_w\right] + \Delta C'\left[X + \frac{d_w}{2} + R_w\right] \quad (7.2)$$

The agreement is almost perfect when the nanowires are far apart ($d_w > 200$ nm), and reasonably good until the nanowires are resolvable (for the smallest separations a relevant discrepancy is observed related to the capacitive coupling of the nanowires, as will be discussed later below). Therefore, if we define the spatial resolution as the edge-to-edge nanowire separation for which the difference between the maximum of the signal and the minimum in between the two nanowires, Δ, (see Fig. 7.3f) is at least twice the noise of the measuring instrument $\Delta C'_{noise}$, i.e. $\Delta = 2 \times \Delta C'_{noise}$ (typically $\Delta C'_{noise}$~0.1 zF/nm-1 zF/nm), we can calculate it by just using Eq. (7.2) and the single nanowire spread function in Eq. (7.1).

Indeed, by assuming that one of the maxima is located at the position $X = d_w/2 + R_w$ and the minimum at $X = 0$ one has that,

$$\Delta = \Delta C_{2\omega}'\left[\frac{d_w}{2} + R_w, d_w\right] - \Delta C_{2\omega}'\left[0, d_w\right]$$
$$= \Delta C'(0) + \Delta C'\left(d_w + 2R_w\right) - 2\Delta C'\left[\frac{d_w}{2} + R_w\right] \quad (7.3)$$

where in the second line we used Eq. (7.2). Eq. (7.3) enables calculating the parameter D from the single nanowire spread function parameters ($\Delta C'_0$, w_0 and w_1). Figure 7.4(a) (symbols) shows the dependence of Δ as a function of d_w determined from the two-nanowire profiles numerically calculated ΔC'(X) (some additional separations at close distances have also been included). The solid line in Fig. 7.4(a) shows the prediction from Eq. (7.3). The agreement with the numerical calculated values is very good (this agreement is maintained even if the maximum and minimum values are affected by the capacitive coupling, as discussed below). Therefore, a reasonable estimation of the spatial resolution can be obtained from the single nanowire spread function and its parameters ($\Delta C'_0$, w_0 and w_1), without performing complex and long two nanowire simulations. The spatial resolution is determined as the critical separation of the nanowires d^*_w at which $\Delta = 2 \times \Delta C'_{noise}$ (for instance in Fig. 7.4 the spatial resolution is ~70 nm for a noise of 1 zF/nm, while it decreases to ~60 nm for a noise of 0.1 zF/nm).

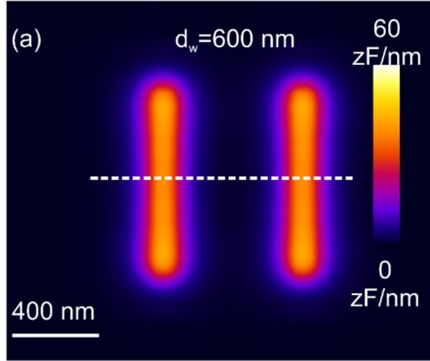

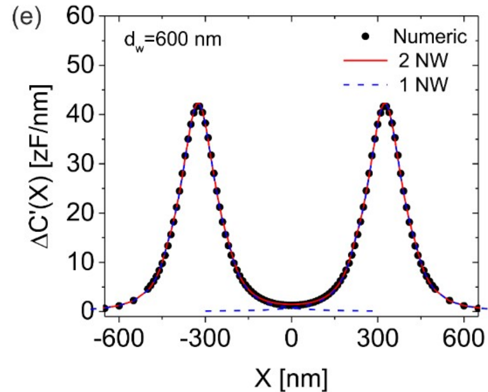

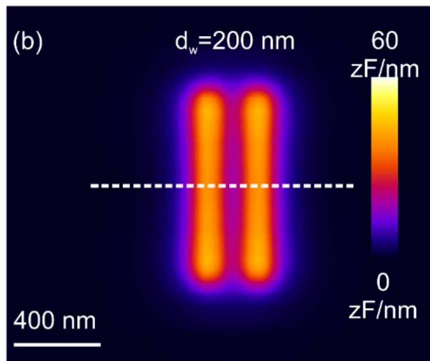

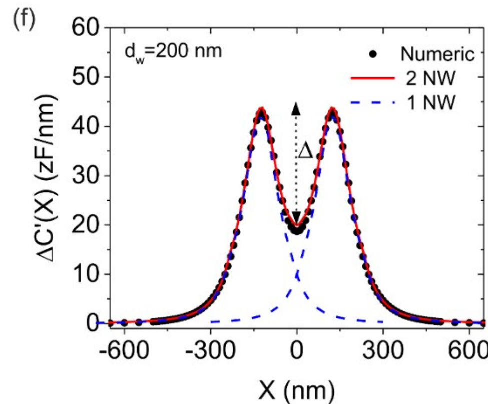

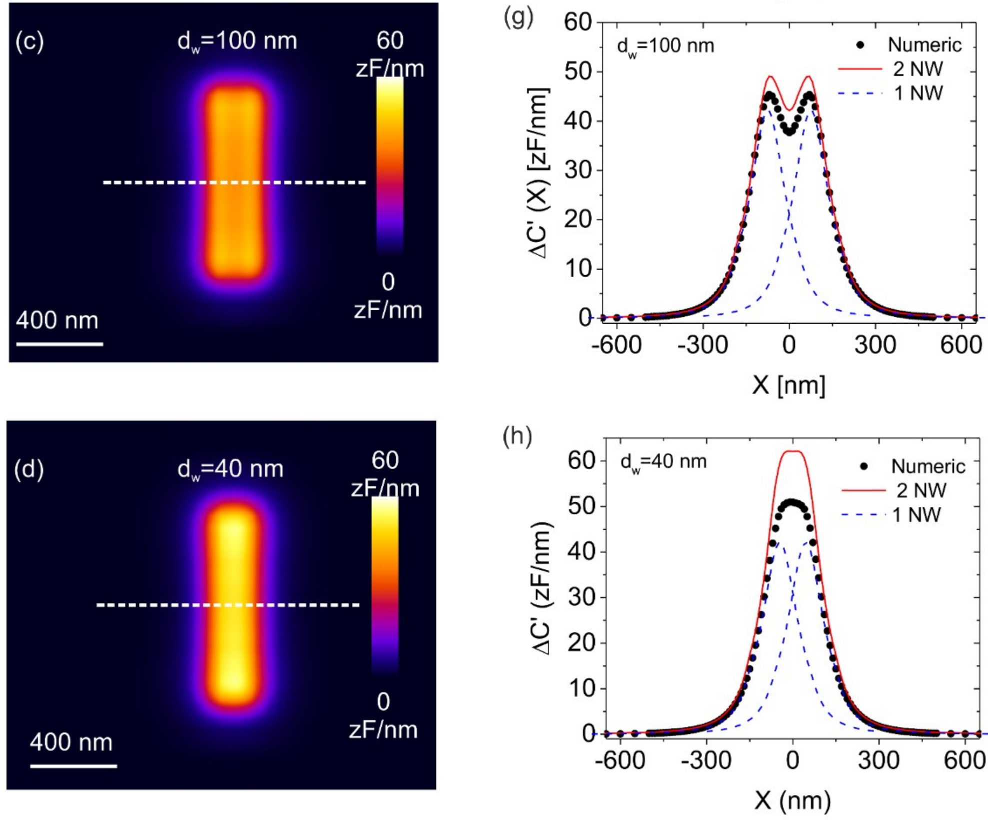

Figure 7.3. (a)-(d) Calculated constant height dC/dz EFM images for two parallel nanowires buried a depth h_1 = h_2=10 nm and separated distances d_w=600 nm, 200 nm, 100 nm, and 40 nm, respectively. The parameters of the calculations are the same as in Fig. 7.1. (e)-(h) (symbols) ΔC'(X) profiles calculated along the dashed lines shown in (a)-(d).

Figure 7.4(b-f) shows the spatial resolution calculated by this method for three instrumental noise values, $\Delta C'_{noise}$=1 zF/nm (blue symbols), 0.1 zF/nm (red symbols), and 0 zF/nm (dashed line, ultimate limit), as a function of the tip-sample distance, depth, tip radius, matrix dielectric constant and nanowire dielectric constant, respectively.

We first note that for shallow buried nanowires (at depths smaller than ~40 nm) sub-100 nm spatial resolution is relatively easily achievable if EFM images are acquired at close distances from the surface of the matrix (closer than ~40 nm). The attainability of specific spatial resolution depends on the system parameters. For instance, in the present case, the optimum spatial resolution can be achieved by considering intermediate tip radius values (here R ~ 40 nm - 50 nm, see Fig. 7.4(d)), rather than considering a minimal tip radius. The reason being that the cone contribution in the imaging of buried nanowires plays a relevant role so that a larger radius makes the cone contribution to be slightly smaller than for small tip radius (since then it will be closer to the surface). When the nanowires are buried deeper than some tens of nanometers,

the spatial resolution decreases roughly linear with the depth (Fig. 7.4(c)), the lower the spatial resolution the larger the instrumental noise. Surprisingly enough the dielectric constant of the matrix does not play a big role in a relatively broad range of values $1 < \varepsilon_m < 20$ (Fig. 7.4(e)), due to the relatively little dependence of the widths of the nanowire spread function on this parameter (Fig. 7.3(i)). For larger ε_m values, the spatial resolution increases due to the screening of the electric potential by the matrix thus reducing the contrast maximum (Fig. 7.3(i)). The dependence on the dielectric constant of the nanowires, ε_w, is similar to that on ε_m, except for values close to the matrix dielectric constant (here $\varepsilon_w = 4$), where it increases largely due to the loss of dielectric contrast (Fig. 7.2(j)). As a rule, any parameter reducing the maximum contrast or increasing the spread function widths will decrease the attainable spatial resolution.

7.3. Nanowire capacitive coupling

We have seen in Fig. 7.3(e-h) that the numerically calculated capacitance gradient contrast profiles, $\Delta C'(X)$, depart at small separations (d_w<100 nm) from the ones calculated by just adding the nanowire spread function of the two nanowires (Eq. (7.3)). As we have mentioned before, this fact is due to the capacitive coupling between the nanowires, which results in a reduction of the electric force acting on the tip. The capacitance per unit of length between two long parallel nanowires in an infinite medium with dielectric constant ε_m is given by Ref[113]

$$C_{2NW} = \frac{\pi \varepsilon_0 \varepsilon_m}{a\cosh\left[1 + \frac{d_w}{D_w}\right]} \tag{7.4}$$

This function increases sharply for $d_w < D_w$, which is in fact the separations for which indeed we found the capacitive coupling is relevant. The presence of the coupling makes that some electrostatic energy of the system is stored in between the nanowires, thus reducing the electrostatic force acting on the tip. This result can also be understood the other way around, i.e., when a significant capacitive coupling is detected in an EFM measurement, it implies that the separation between the nanowires is smaller than its diameter, (i.e.) the nanowires are close together. At such distances, the overall dielectric properties of the nanocomposite are expected to be strongly modified. Also, when the distance becomes small enough for conduction to take place between the nanowires, the conductive properties of the materials are expected to change drastically. For most applications, special interest[128] exist on the separation between different nanowires, since when the separation is large (a few nm) the nanowires can be assumed to be isolated. In contrast, when the separation is short (below a few nm), they can be considered electrically connected (which is relevant to

determine the percolation properties of the material), strongly affecting the conductivity and dielectric response of the nanocomposite material.

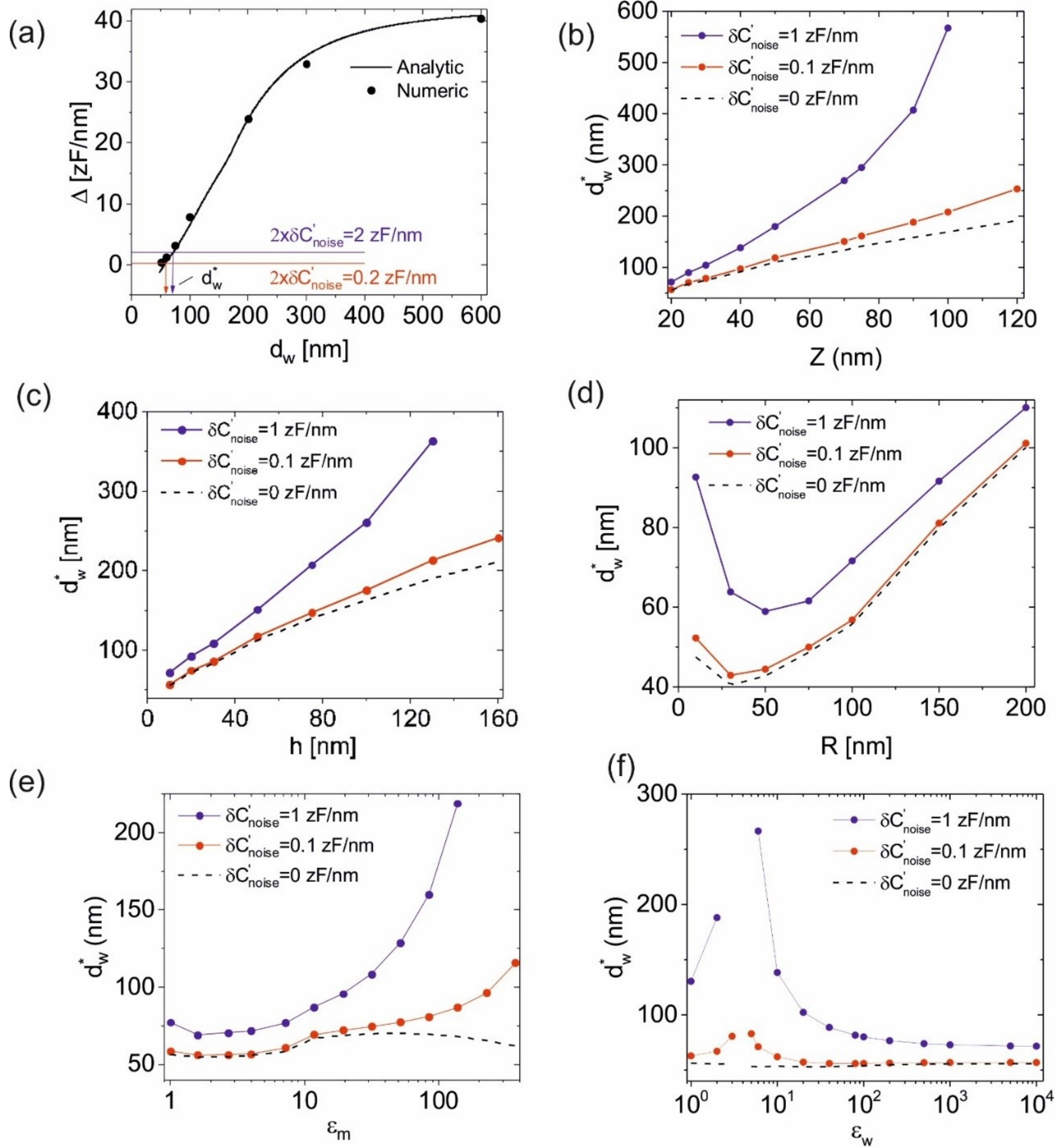

Figure 7.4. (a) Difference between one of the maxima and the minimum, Δ, of the calculated profiles ΔC'(X) in Fig. 7.3(e-h)(symbols), as a function of the separation between the nanowires (two additional separations d_w=60 nm and 70 nm are also considered). Approximation for Δ obtained from Eq. (7.3) (continuous line). The intersection of the curves with twice the noise levels, 2xΔC'_{noise} provide the attainable spatial resolution, d^*_w. (b)-(f) Spatial resolution for three noise levels (ΔC'_{noise}=1 zF/nm, black symbols, 0.1 zF/nm, red symbols, and 0 zF/nm dashed line) as a function of, respectively, the tip sample-distance, z, depth, h, tip radius, R, matrix dielectric constant, ε_m, and nanowire dielectric constant, ε_w. The spatial resolution has been obtained by using Eq. (7.3) with the parameters (ΔC'$_0$, w_0 and w_1) plotted in Figs. 7.2(f-j).

Conclusion:

We have analyzed the spatial resolution achievable in the sub-surface characterization of nanowire nanocomposites by means of EFM. We have initially shown that the nanowire spread function of an isolated nanowire consists of a modified Lorentzian with a cubic decay, which can be parametrized by its maximum and the full widths at the half and one-fifth maximum. Following that, we have derived a simple method to determine the spatial resolution based on the nanowire spread function and validated it by means of multiple nanowire numerical calculations. The dependence of the spatial resolution on several system parameters has been analyzed. We have shown that sub-100 nm spatial resolution is relatively simple to achieve for shallow buried nanowires, while the spatial resolution increases as the nanowires are deep inside the matrix. As a rule, we have demonstrated that any system parameter decreasing the maximum of the nanowire spread function or increasing its widths (or both) will result in a loss of spatial resolution. In addition, with the multiple nanowire simulations, we have shown that the electric force acting on the tip is reduced with respect to the sum of the forces made by individual nanowires when the capacitive coupling between the nanowires becomes relevant. This phenomenon typically happens for separations smaller than the diameter of the nanowires. These results open the possibility to use SDM measurements to detect the capacitive coupling between nanowires in a nanowire nanocomposite, which is relevant from the determination of the overall dielectric properties of the material. Finally, the present results show that EFM can constitute a valuable nanoscopic technique in the non-destructive characterization of nanowire nanocomposite materials.

Chapter 8

Depth Mapping of Silver Nanowires Nanocomposites by Scanning Dielectric Microscopy

In the previous chapters, I have presented the necessary methods concerning nanowire nanocomposite sample preparation (Chapter 6) and for the theoretical modeling of EFM applied to these samples (Chapter 5 &7). In this chapter, I put together these developments to address one of the main objectives of thesis, namely, the depth mapping of silver nanowires in nanocomposite materials by means of Scanning Dielectric Microscopy. This chapter is almost entirely equal to the article "Depth Mapping of Silver Nanowires in Gelatin Nanocomposites by Scanning Dielectric Microscopy" by Harishankar Balakrishnan, Ruben Millan-Solsona, Martí Checa, Rene Fabregas, Laura Fumagalli and Gabriel Gomila, .submitted for publication. In this work I was in charge to prepare and characterize the sample, to acquire the EFM images together with Dr. M. Checa, to analyze the depth distribution together with R. Millan-Solsona, and to analyze theoretically the results together with Dr. R. Fabregas. The article was written in collaboration with Dr. G. Gomila and the rest of the authors.

Abstract:

We have already mentioned that nanocomposite materials based on metallic nanowires are widely investigated as transparent and flexible electrodes or as stretchable conductors and dielectrics for biosensing. Here we show that Scanning Dielectric Microscopy (SDM) can map the depth distribution of the nanowires within the nanocomposites in a non-destructive way. To achieve it we combine the sub-surface imaging capabilities of Electrostatic Force Microscopy with its quantitative analysis by means of finite element numerical calculations. As an application we determined the three-dimensional spatial distribution of ~50 nm diameter silver nanowires in ~100 nm-250 nm thick gelatin films. The characterization is done both in dry ambient conditions, where gelatin presents a relatively low dielectric constant, ε_r~5, as well as, in humid ambient conditions, where its dielectric constant rises up to ε_r~14. Present results show that SDM can be a valuable non-destructive subsurface characterization technique for nanowire-based nanocomposite materials, which can contribute to optimize the properties of these materials for applications in fields such wearable electronics, solar cell technologies or printable electronics.

Introduction:

The macroscopic physical properties of metallic nanowire nanocomposites depend on the dimensions of the nanowires (diameter and length), their concentration (in % weight of the composite) and their spatial distribution within the polymer matrix. Information on the 2D spatial distribution of the nanowires on intact samples can be obtained by optical microscopy on transparent samples (metallic nanowires are usually detectable in transparent samples although with low spatial resolution), Scanning Electron Microscopy (although with some limitations due to the insulating nature of the polymer matrices) and Atomic Force Microscopy (since usually the buried nanowires induce small protrusions on the upper surface). To gain information on the 3D spatial distribution of the nanowires, instead, one should resort to nanoscale tomographic techniques. We have already mentioned that the current gold standard nanoscale tomographic techniques in Materials Sciences based on Electron (EM) and X-Ray microscopies[12,14,123] have not been much applied to metallic nanowire polymer nanocomposites[124], due to the intrinsic limitations of these techniques when applied to polymeric materials. Alternative nanoscale tomographic techniques compatible with the properties of polymeric materials are based on sub-surface sensitive Scanning Probe Microscopies (SPM)[8,125]. Techniques such as Scanning Near Field Ultrasound Holography[4,23], Mode Synthesizing Atomic Force Microscopy[55], Multimodal AFM[52], Amplitude Modulated AFM[1,117], Electrostatic Force Microscopy[62,119] , Scanning Microwave Impedance Microscopy[3,5,116,118,121] or Scanning Near Field Optical Microscopy[115] all have demonstrated the capability to image buried nanostructures within polymeric materials. However, nanotomographic reconstruction methods to retrieve the depth distribution of the nanoscale objects have not been developed in all the cases.

As it has been sustained along this thesis, Electrostatic Force Microscopy (EFM) is among the subsurface SPM techniques that has progressed more towards its implementation as a nanotomographic technique compatible with polymeric materials[38,63,69,126,127].

Here, we combine the sub-surface imaging capabilities of Electrostatic Force Microscopy with its quantitative analysis by means of finite element numerical calculations (which we refer to as Scanning Dielectric Microscopy[33]) to demonstrate that the depth distribution of metallic nanowires in nanocomposites can be determined in a non-destructive way with nanoscale spatial resolution. As compared to similar studies performed in CNT polymer nanocomposites[62,63], we had to deal here with additional challenges imposed by the much larger dimensions of the metallic nanowires (e.g. non-planar surfaces of the nanocomposites or relevance of the capacitive coupling between nanowires). As an application we will consider the case of

gelatin/silver nanowire (AgNW) nanocomposites. These nanocomposites, besides its intrinsic interest for the development of biosensors[102], offer the possibility to simply investigate the effect of varying the matrix dielectric constant with ambient humidity, since gelatin passes from ε_r~4 under dry ambient conditions to ε_r~15 for humid ambient conditions[129]. The demonstration that nanotomographic SDM information can be obtained on nanocomposites with high dielectric constant matrices is another important difference with earlier nanotomographic EFM works, which systematically considered polymeric materials with very low dielectric constants (ε_r ~2-3), which offered optimal conditions for sub-surface EFM characterization.

Results and discussion:

As explained in chapter 6, Gelatin/AgNWs nanocomposites have been prepared by first drop-casting ~50 nm diameter AgNWs on top of a highly doped silicon substrate and then spin-coating gelatin on top of them and letting the sample to dry. Figure 8.1 shows a 60 mm x 60 mm topographic AFM image of one of the samples analyzed. A scratch has been made on purpose to measure the sample thickness, giving, in this case a thickness t_m~254 nm±1 nm (see cross-section profile in Fig. 8.1(b) and histogram analysis in Fig. 8.1(c)). The AgNWs within the gelatin film are clearly visible in the topographic AFM image, where they appear as small protrusions on the, otherwise, very flat gelatin surface (rms roughness ~1 nm). The protrusions have heights in the range ~2 nm-15 nm, most of them in the low value range, and widths in the range ~200 nm-1000 nm (see inset of Fig. 8.1(c) where the height versus width of some characteristic protrusions are shown). The dimensions of the protrusions are completely different from the dimensions of the AgNWs (~50 nm diameter). A rough linear relation between the height and the width of the protrusions seem to exist.

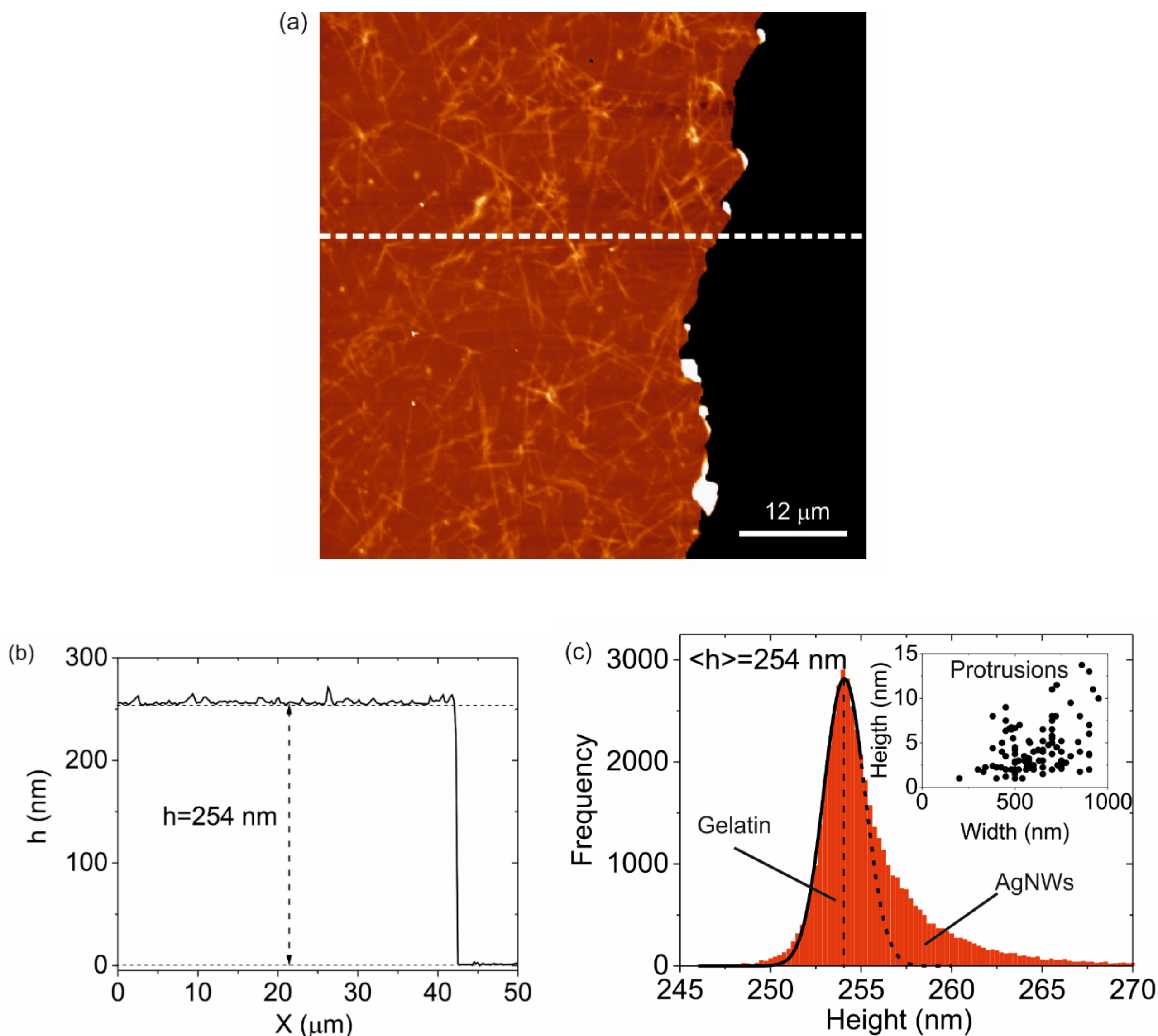

Figure 8.1. (a) Large scale AFM topographic image (60x60 mm²) of a gelatin/AgNW film ~254 nm thick containing ~50 nm diameter silver nanowires on a highly doped silicon substrate. The gelatin film has been scratched on purpose to determine its thickness. (b) Cross-section topographic profile along the dashed line in (a). The small protrusions correspond to the buried nanowires. (c) Histogram analysis of the distribution of heights of the gelatin film. The continuous line is a Gaussian fit to half of the distribution, representing the bare gelatin parts (the dashed line is an extrapolation of the Gaussian fit). The heights outside the Gaussian distribution correspond to the protrusions due to the buried nanowires. Inset: Height vs width of some representative protrusions present in (a).

The AFM topographic image reveals the nanowires buried in the gelatin film and can provide an overview of its 2D distribution. However, it does not provide information on the depth at which the nanowires are buried. In particular, it does not inform the separation among crossing nanowires, which is a parameter of relevance to determine the nanocomposite's overall macroscopic properties.

In order to obtain information on the depth distribution of the nanowires, EFM measurements have been performed. Here we used the force volume acquisition mode presented recently[37] and described in *section 3.1*, in which full ac electric force approach curves are acquired at each pixel of the image. From the force volume data, EFM images can be derived by post-processing in any desired mode and at any desired imaging distance[37]. Fig. 8.2(a-e) and 8.2(f-j) show, respectively, high resolution AFM topographic and constant height EFM images corresponding to selected regions of the sample in Fig. 8.1(a). All the EFM images correspond to a tip-gelatin distance z=36 nm (z=290 nm with respect to the substrate). The EFM images are expressed, as usual[33], in terms of the capacitance gradient, dC/dz, which is related to the ac electric force amplitude at the 2w harmonic by $F_{2w}=1/4\ dC/dz\ v_0^2$, where v_0 is the amplitude of the applied ac voltage. The EFM images, like the topographic AFM ones, clearly reveal the presence of the buried nanowires. At first sight a clear correlation exists between the AFM topographic and EFM images. This correlation is not related to the topographic crosstalk present in lift-mode EFM images[130] . The correlation exists due to the non-planar nature of the sample surface, which makes that the constant height EFM images display higher electric forces at the locations of the topographic protrusions, since they are closer to the tip. However, the measured electric forces do not only contain information on the topographic protrusions, but they also provide information on the electric polarization of the buried nanowires. This fact can be seen directly in the few cases in which the nanowires are only visible in the EFM images and not in the AFM topographic images (for instance in Fig. 8.2(b) the one highlighted with an arrow).

In order to disentangle the contribution to the electric force of the topographic protrusions and of the polarization of the buried nanowires, we have considered the model shown in Fig. 8.2(k) (not to scale), which includes both a surface protrusion and a buried nanowire. Note that in earlier studies on CNTs nanocomposites[62,63], it was not necessary to include the surface protrusions since CNTs are much smaller than AgNWs and hence they perturb much less the surface of the nanocomposites. Figure 8.2(l) shows an example of a calculated electric potential distribution obtained with the model in Fig. 8.2(k), which shows the locality of the electric interaction. In Fig. 8.2(l) the top lines represent the ends of the protrusion centered on the nanowire, which otherwise is imperceptible at the scale of the representation.

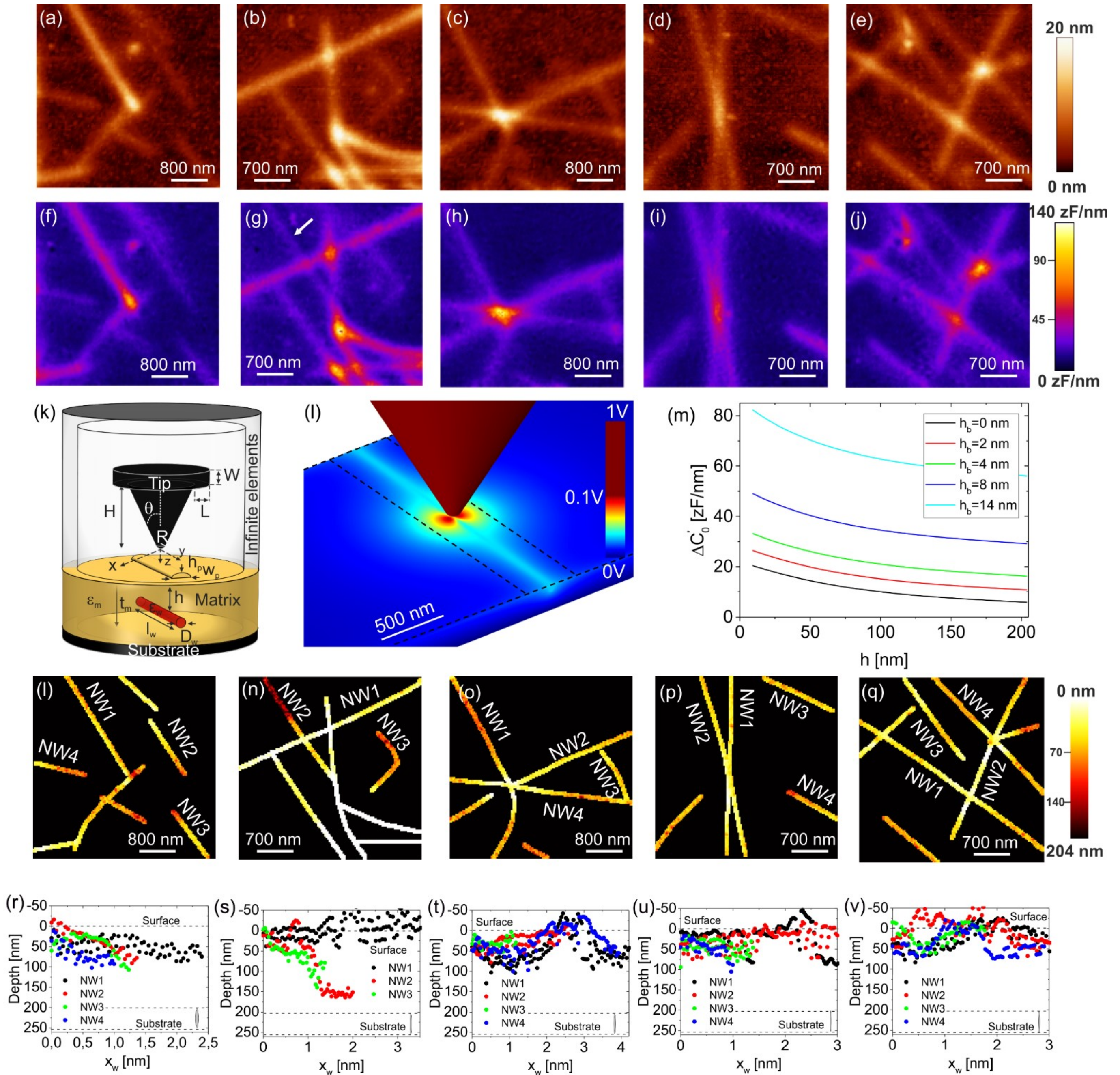

Figure 8.2. (a)-(e) Topographic AFM and (f)-(j) capacitance gradient constant height EFM images (z=36 nm) obtained on five selected regions of Fig. 8.1a. Experimental parameters: Tip spring constant k=0.57 N/m, resonance frequency f_0=17 kHz, voltage frequency f_{el}=2 kHz, voltage amplitude v_0=4 V. (k) Schematic representation of the buried nanowire model with surface protrusion used to quantify the EFM data. (l) Example of a calculated electric potential distribution. Parameters of the calculations: Tip-sample distance z=36 nm, tip radius, R=87 nm, half cone angle, θ=28º, gelatin thickness, t_m=254, gelatin dielectric constant, ε_m=14, nanowire diameter D_w=50 nm, nanowire length, l_w= 8 mm, nanowire dielectric constant ε_w=10^5 (metallic),the width of the protrusion, w_p=620 nm. (m) Calculated maximum capacitance gradient contrast, $\Delta C_0'$, at the center of the nanowire as a function of the depth position of the nanowire for different heights of the surface protrusions. Same parameters as in (l)-(q). Depth maps of the nanowires corresponding to the five regions analyzed were determined with the help of the model in (k). The depths have been determined by fitting calculated full approach curves at each pixel on top of the nanowires. (r)-(v)

Depth profiles along some of the nanowires present in (l)-(q). Negative depths indicate the presence of inter-nanowire capacitive interaction.

Figure 8.2(m) shows the numerically calculated dependence of the capacitance gradient contrast, ΔC', as a function of the depth position of the nanowire, h, for the tip at z=36 nm from the flat part of the sample and for different heights of the surface protrusions, h_p. Since the width of the protrusions, w_p, plays a minor role it has been kept fixed to a representative value of w_p=620 nm. For a given protrusion height, the graph shows that the capacitance gradient contrast ΔC' presents a strong dependence on the depth position of the nanowire, thus enabling to determine the depth from the measured ΔC'[62,63]. The graph also shows that the protrusion height induces an important vertical shift of the capacitance gradient contrast ΔC' curves. This later result explains why there is a correlation between the AFM topographic and EFM images, and indicates that the presence of the protrusions needs to be accounted for explicitly. Finally, we note that, in the present case, the EFM measurements are sensitive to the depth position of the nanowires in the whole thickness of the gelatin film, since the measuring noise is ~1 zF/nm and the minimum contrast generated by a buried nanowire (when at the bottom of the gelatin film) is ~5 zF/nm (see Fig. 8.2(m)). Based on these results, to determine the depth position of the nanowires inside the gelatin film we have proceeded as follows. At a given position on top of a nanowire, we determined the height of the protrusion, h_p, from the topographic image (the width is kept the same for all protrusions, w_p=620 nm, due to its minor effect). Then, for the given protrusion height, we calculated theoretical *dC/dz* approach curves with the model in Fig. 8.2(k) for different depths, h, of the nanowire and fitted them with the experimental *dC/dz* curve acquired at the given position, with the depth, h, as the single fitting parameter. This process is repeated at all points along the nanowires. The rest of the parameters of the model are determined as follows: the thickness of the gelatin film (t_m=254 nm) is obtained from the large-scale topographic image (Fig. 8.1a), the tip radius (R=87nm±2nm), half cone angle (θ=28.3º±0.4º) and capacitance gradient offset (C'_{offset}=107 zF/nm±2 zF/nm) from *dC/dz* approach curves acquired on the bare substrate (see appendix A8.1), and the dielectric constant of gelatin (ε_m=13.8±0.3) from *dC/dz* approach curves acquired on gelatin regions do not containing any nanowire (see appendix A8.1). For the nanowires we took a diameter D_w=50 nm, as a representative value according to manufacturer specifications and to our own earlier characterization[78] (see Appendix A8.2 for the effect of the nanowire diameter in the extracted depth). For the length of the nanowire, we took l_w=8 mm (see appendix A8.3 for the effect of the nanowire length on the results). Finally, we assumed a very large dielectric constant for the nanowire (ε_w=10^5), which corresponds to the metallic limit. Fig 8.2(l-q) show maps of the depth position of the nanowires within the gelatin matrix determined in this way corresponding to the five regions analyzed in Fig. 8.2(a-e). Figures 8.2(r-v) show depth profiles taken along some representative nanowires present in Fig

8.2(l-q). The first relevant aspect noted is that most nanowires seem to be located very close to the gelatin top surface (depths ~10 nm-75 nm). This result is remarkable since when the sample was prepared the nanowires were initially spread on the bottom substrate. Another relevant aspect of Fig 8.2(l-q) and 8.2(r-v) is that the depth maps reveal the inclination of some of the nanowires (e.g., NW2 and NW3 in Fig. 8.2(r) and 8.2(s)). Detecting the inclination of the nanowires with a model like the one in Fig. 8.2(k), which considers a non-inclined nanowire, is possible because of the very local nature of the tip-nanowire interaction, as it is demonstrated in appendix A8.4. Finally, we can identify for crossing nanowires which one is located on the top and which one at the bottom from the depth maps, which is not apparent from the topographic or EFM images. For instance, in Fig. 8.2(n) NW2 is crosses below NW1, while in Fig. 8.2(o) NW2 crosses above NW4.

At the crossing points between different nanowires, the depths tend to show smaller values than for the rest of the nanowire (and even sometimes the values are directly unphysical, e.g., negative). There are two effects responsible for this fact, namely, the fact that the surface protrusion of crossing nanowires is much wider than that of a single nanowire (included in the model of Fig. 8.2(k)), and the fact that multiple nanowires can contribute to the measured electric force (a single nanowire is included in the model of Fig. 8.2(k)). Both effects would lead to larger electric forces, as observed experimentally. The way how multiple nanowires contribute to the measured electric force in SDM merits some comments, since it is not trivial due to the relatively large size of the nanowires and to the strong dependence of the electrostatic force on the depth position. Again, the situation is very different from what would occur on CNTs nanocomposites[62,63] , which are much smaller in diameter. To analyze the electric force generated by crossing nanowires we have considered a model like the one in Fig. 8.2(k) but with two nanowires crossing at an angle, a (see inset in Fig. 8.3(a)). The nanowires are assumed to be parallel to the substrate, and, for simplicity, no surface protrusion is considered (h_p=0 nm).

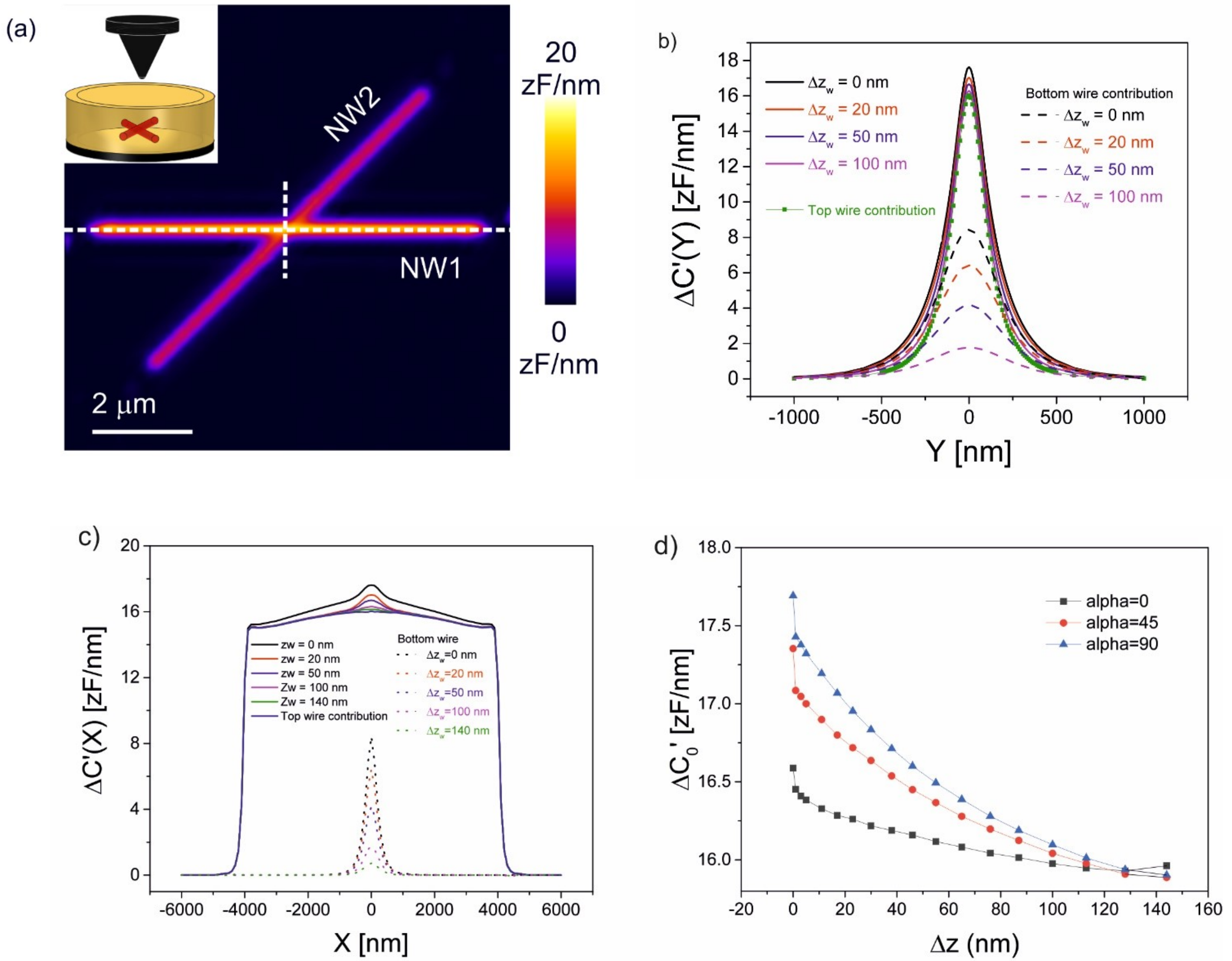

Figure 8.3. (a) Numerically calculated constant height EFM image corresponding to two nanowires parallel to the substrate crossing at an angle a=45º and with a vertical separation Δz_w=0 nm. Parameters of the calculations: same as in Fig. 8.2, z=36 nm, D_{w1}= D_{w2}=50 nm, l_{w1}=l_{w2}=8 mm, ε_{w1}= ε_{w2}=10^5 (metallic), h_1=10 nm, h_2=60 nm, t_m=254 nm, ε_m=13.8, R=87 nm, θ=28º, H=12.5 mm, W=3 mm, L=3 mm. (b) and (c) (continuous lines) $\Delta C'$ profiles across and along the top nanowire (dashed lines in (a)), respectively, for three different depths of the bottom nanowire h_2=60 nm, 80 nm and 160 nm, corresponding to vertical interwire separations Δz_w=0 nm, 20 nm and 100 nm, respectively. For comparison, we have also plotted the profiles corresponding to single nanowires located at the positions of nanowires 1 and 2 (dashed black and green lines, respectively). (d) Capacitance gradient contrast $\Delta C'_0$ at the center of the top nanowire (X=Y=0) as a function of the vertical separation between nanowires, Δz_w, for three crossing angles (a=0º, 45º and 90º). For comparison, the value corresponding to a single nanowire at the position of the top nanowires is shown (dashed lines).

Figure 8.3(a) shows a calculated constant height ΔC' EFM image (z=36 nm) for this model for a crossing angle α=45º and the two nanowires in close contact (interwire vertical separation, from edge to edge, Δz_w= 0 nm). Fig 8.3(b-c) show ΔC' profiles taken along the dashed lines in Fig. 8.3(a) for different interwire vertical separations Δz_w=0 nm (black line), 20 nm (grey line) and 100 nm (red line). For comparison, in Fig 8.3(b-c) we have also plotted the ΔC' profiles corresponding to the two nanowires when alone (dashed

black and green lines, respectively). Clearly, the bottom nanowire contributes to the total calculated capacitance gradient, ΔC', mainly in the crossing region. However, its contribution is much smaller than the one corresponding to an isolated nanowire at the same depth. The reason being that the top nanowire largely screens the electric field below it at the crossing point preventing the polarization of the bottom nanowire in this region. The actual contribution to the total capacitance gradient of the bottom nanowire can be seen in Fig. 8.3(d) by comparing the total capacitance gradient contrast at the center of the top nanowire, $\Delta C'_0$, as a function of the interwire separation and crossing angle (continuous lines), with the signal due to the top nanowire when alone (dashed line). In this case, the contribution of the bottom nanowire is just 1-1.5 zF/nm over a total of 16-18 zF/nm. This small contribution cannot explain alone the artifacts observed in the depth maps at the crossing point, from what we conclude that also the topography of the surface at the crossing point should play a relevant role.

The depth mapping capabilities of SDM have also been demonstrated on gelatin/AgNW nanocomposites under dry ambient conditions, where the dielectric constant of gelatin lowers down to ε_r~4.8, as compared to ε_r~14 in humid ambient conditions (see appendix A8.5). Fig 8.4(a) shows an AFM topographic image of the sample analyzed. The thickness of the nanocomposite film is here t_m~98 nm (see the topographic cross-section profile in Fig. 8.4(b)). Like the sample analyzed in Fig. 8.2, the surface of the gelatin is fairly flat (rms roughness ~1 nm), and it only shows some very small protrusions induced by the buried nanowires (few nanometers high and hundreds of nanometers wide). Figure 8.4(c) shows a constant height EFM image corresponding to a tip-substrate distance z=130 nm (i.e., at ~32 nm from the gelatin surface). Fig 8.4(d) shows a capacitance gradient cross-section profile along the dashed line Fig. 8.4c. The buried nanowires are again clearly seen in the EFM image. Fig 8.4(e) shows the corresponding depth map, while Fig. 8.4(f) shows a cross-section profile taken along the dashed line in Fig. 8.4(e). In the figure, we have drawn the cross-section of the nanowires, according to the scale of the graphical representation. The parameters used in the quantitative analysis to derive the depths are indicated in the caption of Fig. 8.4 caption (see also appendix A8.5). Finally, Fig. 8.4(g) show the depth profiles taken along with some of the nanowires present in Fig. 8.4(e). In Fig. 8.4(g) the dashed lines indicate the values of the depth for which the nanowire will be lying at the surface and at the bottom substrate, respectively. In the present case the nanowires seem to lie nearly on the substrate, and hence, parallel to it. In the region where the nanowires cross each other, significantly lower depths are obtained, for the reasons explained above. The crossing nanowires do not seem to be located at different depths, which would indicate that the nanowires wrap one on top of the other at the crossing points.

In the present case, the contribution of the protrusions to the measured capacitance gradient contrast, $\Delta C'$, is smaller and the sensitivity to the depth higher, since the gelatin in dry ambient conditions has lower dielectric constant. We show it in Fig. 8.4(h) where we plot the variation of capacitance gradient contrast at the center of a nanowires, $\Delta C'_0$, on the depth position of the nanowire for different heights of the gelatin surface protrusions. The continuous lines correspond to the actual measured dielectric constant in this case, ε_m=4.8, while the dashed lines correspond to the values expected in humid conditions with ε_m=13.8. The curves when the height of the protrusions increases shift up much less for the dielectric constant ε_m=4.8 than for ε_m=13.8, meaning that they contribute much less to the capacitance gradient values. Moreover, for a given protrusion height, the capacitance gradient shows a steeper dependence on the depth, meaning a higher sensitivity to the depth position of the nanowire. Figures 8.4(i-l) show a similar analysis to the one performed in Fig. 8.4(a), 8.4(c), 8.4(e) and 8.4(g) but corresponding to another region of the sample. This analysis confirms the main findings described before.

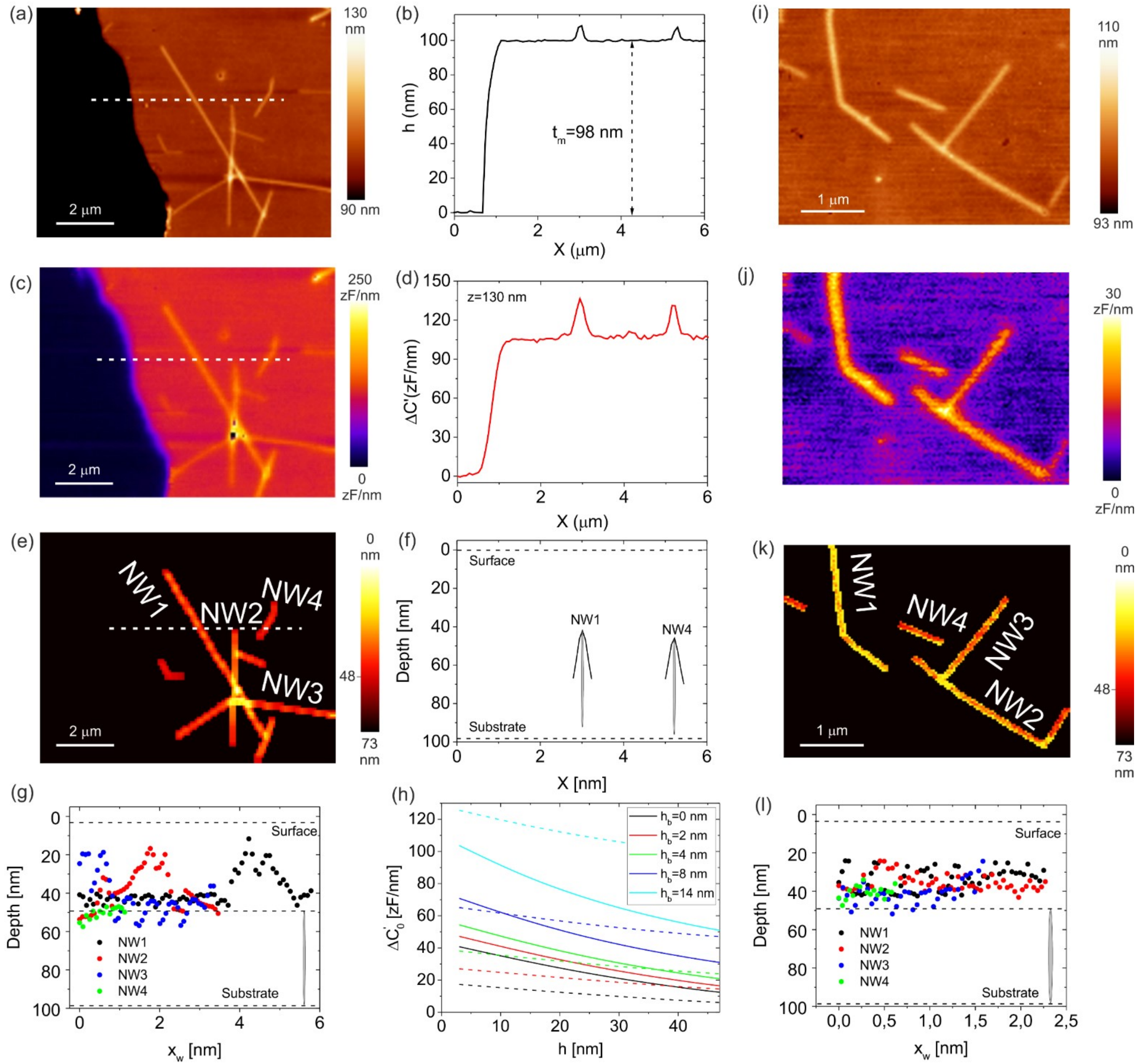

Figure 8.4. (a) Topographic image of a gelatin/AgNW nanocomposite under dry ambient conditions. A scratch has been made on the gelatin nanocomposite to determine its thickness. Experimental parameters: k=0.39 N/m, f_0=17 kHz, f_{el}=2kHz and v_0=4 V. (b) Topography cross-section profile along the dashed line in (a). (c) Constant height EFM image reconstructed at a distance z=130 nm with respect the substrate. The black spots in the image corresponds to regions whose topography is higher than the distance at which the image is reconstructed. (d) Capacitance gradient contrast profile, $\Delta C'(X)$, along the dashed line in (c). (e) Depth map of the nanowires present in the region analyzed in (a). Parameters used in the quantitative analysis: R=136 nm, θ=29.3º, t_m=98 nm, ε_m=4.8, w_p=220 nm, D_w=50 nm, l_w= 8 mm, $\varepsilon_w=10^5$ (metallic). (f) Depth cross-section profile along the dashed line in (e). The cross-section of the nanowires has been drawn to the scale of the figure. (g) Depth profiles along some selected nanowires present in (e). (h) Calculated contrast at the center position of the nanowire for z=32 nm as a function of the depth position for different heights of the surface protrusions. Continuous and dashed lines are for ε_m=4.8 and

13.8, respectively. The rest of parameters are the same as in (e). (i)-(l) Same as (a), (c),(e) and (g) but for a different region of the sample.

Materials and methods:

Gelatin nanocomposite preparation:

The sample was prepared as described in chapter 6. We present it here for easier reference and to include some specific aspects. To prepare the gelatin nanocomposites we use a highly doped silicon substrate. Prior to its use, the substrate was cleaned with the help of Acetone (PanReac, Applichem) & 2-Propanol (Sigma Aldrich, ACS reagent) in an ultrasonic water bath and thoroughly dried. Silver nanowires (A50 Research Grade, 0.5 g dissolved in 50 mL IsoPropyl Alcohol, IPA) were obtained from Novarials (Novawire-Ag-A50). The nanowires (AgNWs) were further diluted in IPA to produce a relatively sparse network of nanowires in the nanocomposites. The AgNWs were drop casted on the Si substrate and let dry in a vacuum chamber for 3 hours. Gelatin from Porcine Skin - Type A was procured from Sigma Aldrich. 100 mL MilliQ water was heated close to 90°C and when it is cooled down to 60 °C-70 °C, gelatin was added to it accompanied with constant stirring. The concentration of 2g/100 mL and 4g/100 mL of gelatin in MilliQ water was used in different experiments depending on the required thickness of the nanocomposites. 150 µL-200 µL of the prepared Gelatin solution was then spin coated (Laurell Tech., WS-650MZ23NPP/LTE) on top of the dried AgNW-Si substrates at (i) 1000 rpm at 500 rpm acceleration for 10 seconds followed by (ii) 2000 rpm at 1000 acceleration for 60 seconds. Once coated, the samples were annealed (Hotplate PSelecta, Platronic) at 100 °C for 10 minutes. The prepared samples were stored in vacuum chambers (Kartell Pvt. Ltd.) its use.

Electrostatic Force Volume Microscopy:

Electrostatic Force Volume Microscopy measurements have been performed using the approach detailed elsewhere[37], by using a Nanowizard 4 BioAFM from JPK (now Bruker). Briefly, an ac voltage of frequency f_{el}=2kHz and amplitude v_0= 4V has been applied between the conductive tip (CDT-CONTR f_0=17 kHz) and the highly doped silicon substrate by means of an external lock in (eLockin 204/2 Anfatec). Force volume data have been acquired using the Advanced Quantitative Imaging (JPK) module. At each pixel, the vertical deflection and the electrical 2ω-oscillation amplitude ($A_{2\omega}$) of the cantilever have been measured as a function of tip sample distance. Typically, images of 128 x128 pixels have been acquired. The length of

the approach curve was set to be D_Z=400 nm and each one contained 300 data points. The electrical 2ω-oscillation amplitude ($A_{2\omega}$) is converted to the capacitance gradient in a post-processing step as explained elsewhere[33]. Constant height EFM images have been retrieved from the force volume data at the desired heights following the procedure described in Ref.[37] . Experiments were performed both at ambient conditions and under dry ambient conditions, with the use of a custom-made environmental chamber.

Finite element numerical calculations:

The numerical calculations have been done as described in Chapter 5 . We present it here for easier reference and to include some specific aspects. The quantitative analysis of the EFM approach curves acquired has been carried out following the methods of Scanning Dielectric Microscopy[33], adapted to deal with force volume data sets[37]. In the quantitative analysis we used the model described in Fig. 8.2(k). In it, the tip is modeled as usual[33,34,75] by a truncated cone with height H and half-angle θ terminated in a tangent sphere of radius R. At the top of the cone a "cantilever" disk of thickness W and radius Lc = L + H tan (θ) is introduced to model local cantilever effects. The lever portion of the probe was not explicitly modeled, and its effects were included via a phenomenological capacitance gradient offset, C'_{offset}. The gelatin has thickness t_m and dielectric constant ε_m, and it presents a spherical cap protrusion of height h_p and width w_p. The nanowire is located at a depth h (measured from the upper nanowire edge to the gelatin surface) and has diameter, D_w, length l_w mm and dielectric constant ε_w. The tip is located to a distance z from the gelatin surface. The electrostatic force acting on the tip was determined by solving the Poisson equation for the model described and integrating the Maxwell stress tensor, using the electrostatic module of COMSOL Multiphysics 5.3 and custom codes written in MATLAB (The MathWorks). The calculated force is converted to capacitance gradient by means of the relation $F=1/2\ dC/dz\ V^2$, where V is the applied potential (note that since the calculations are done with a static potential a 1/2 factor needs to be used here).

Tip geometry calibration and gelatin dielectric constant

The tip radius, half cone angle and capacitance gradient offset used in the theoretical model were determined as detailed elsewhere[33], by calculating numerically capacitance gradient dC/dz approach curves for a tip-on-metal model and fitting them to the experimental dC/dz curves measured on a bare region of the substrate. In the analysis, the microscopic parts of the tip were adjusted to their nominal values H = 12.5 mm, W = 3 mm, and L = 3 mm. N=300 experimental dC/dz curves on the bare substrate were typically analyzed. The value of the gelatin dielectric constant was determined as detailed elsewhere[75,77] by calculating

numerically capacitance gradient dC/dz approach curves for a tip-on-thin film model and fitting them to the experimental dC/dz curves measured on a region of the gelatin not containing nanowires. In the calculations, the tip geometry determined earlier is used. N=300 experimental dC/dz curves on the bare gelatin were typically analyzed.

Depth mapping:

The depth of a nanowire has been determined by considering the model in Fig. 8.2(k) and following a procedure similar to the one detailed in Refs.[62,63] generalized to deal with non-planar surfaces. The tip geometry and dielectric constant of the gelatin used in the calculations were determined as described above, and the thickness of the gelatin and the height of the protrusions, were determined from the AFM topographic images (the protrusion width, w_p, was set to a fixed representative value since it does not play a significant role in the calculated forces). To determine the depth, we have calculated dC/dz approach curves on the center of the nanowires and fitted them to the experimental dC/dz curves with the depth as a single fitting parameter. The nanowires were assumed to have diameter, D_w=50 nm, length l_w=8 mm and dielectric constant $\varepsilon_w=10^5$ to mimic a metallic behavior (see appendix A8.2 and A8.3 for other nanowire parameters). Even though the model considers a nanowire parallel to the substrate it also describes locally correctly the case of inclined nanowires (see appendix A8.4).

Conclusions:

We have shown that the depth distribution of silver nanowires in gelatin nanocomposites can be determined in a non-destructive way by means of Scanning Dielectric Microscopy. To achieved it we have overcome the challenges imposed by the non-planar surface of these nanocomposites and the relatively large dielectric constant of gelatin at ambient conditions. The depth maps can provide useful information to investigate the percolation level of the nanocomposite, which is of outmost relevance in determining the overall macroscopic electrical properties of the composite materials. Present results are expected to contribute to optimize the properties of nanowire nanocomposites and to pushforward their application in solar cell technologies or in wearable electronics.

Appendix

A8.1. Photodiode and tip geometry calibration, and gelatin dielectric constant determination for Fig. 8.2:

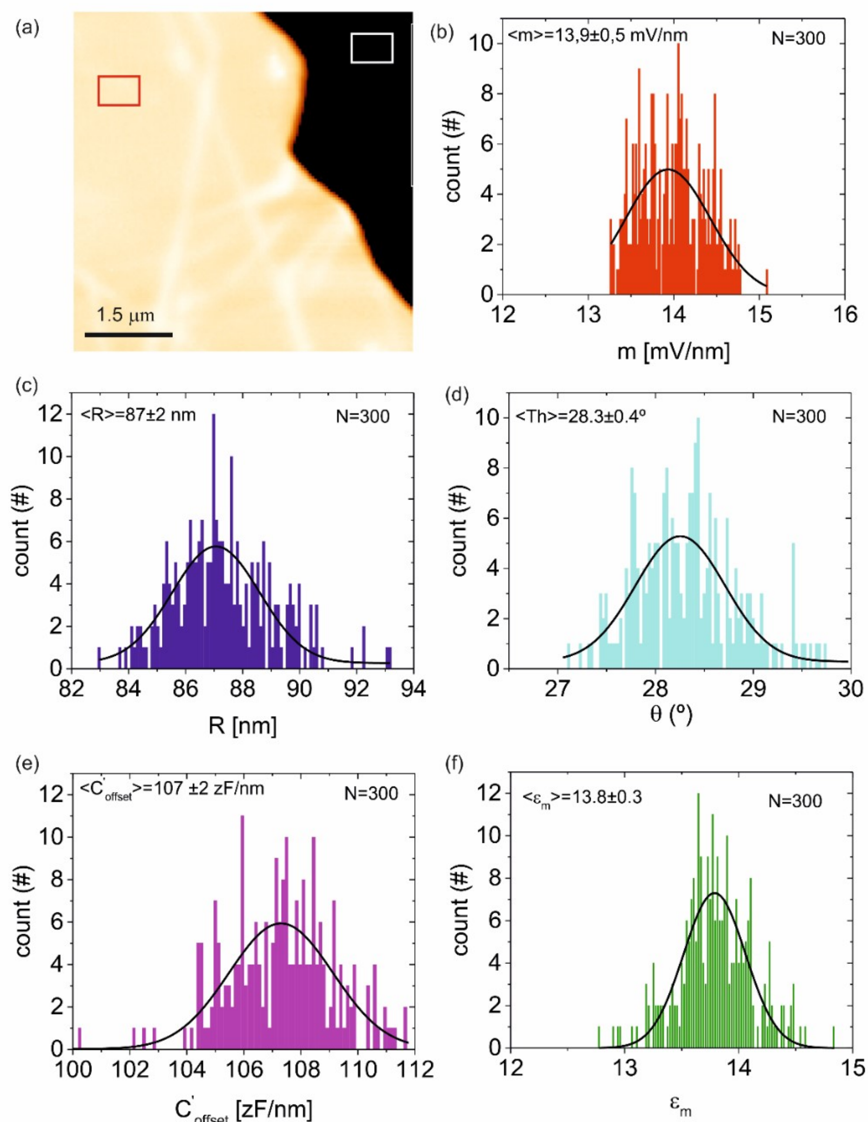

Figure A8.1. (a) AFM topographic image of a small region close to the scratch in Fig. 8.1 of the main text. The white and red rectangles highlight the regions used to calibrate the photodiode sensitivity and tip geometry and to extract the dielectric constant of gelatin, respectively. (b) Distribution of the photodiode sensitivity extracted from the slope of the contact part of the normal deflection approach curves. The mean value (N=300) is 13.9±0.5 mV/nm. (c)-(e) Histogram of the tip radius, half cone angle and capacitance gradient offset obtained by fitting theoretical dC/dz curves generated for a tip-on-metal model to the experimental dC/dz approach curves acquired in the white rectangle region in (a). The mean values (N=300) obtained are R=87±2 nm, θ=28.3±0.4º and C'_{offset}=107±2 zF/nm, respectively. (f) Histogram distribution of the values obtained for the dielectric constant of gelatin obtained by fitting theoretical dC/dz curves generated for a tip-on-thin dielectric film model to the experimental dC/dz approach curves acquired in red rectangle in (a). The mean value (N=300) obtained is ε_m=13.8±0.3.

A8.2. Effect of the nanowire diameter in the estimation of the depths:

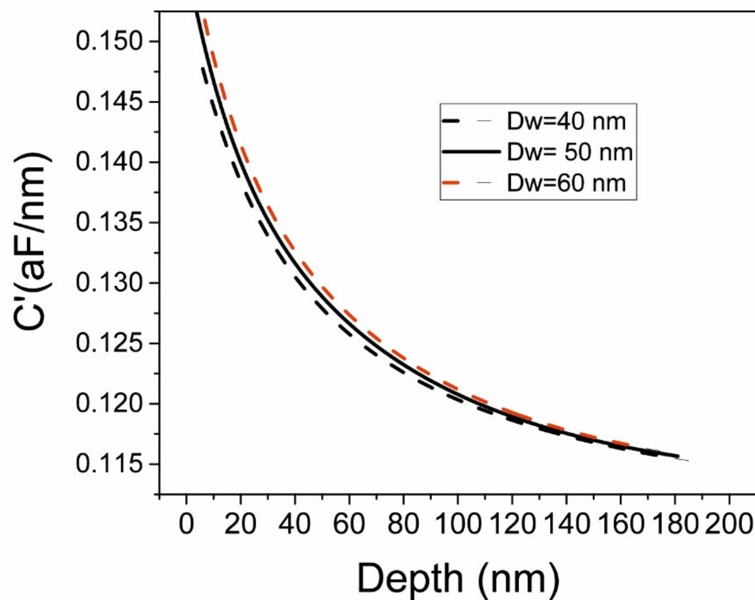

Figure A8.2. Capacitance gradient contrast at the center of the nanowire, $\Delta C'_0$, calculated with the model in Fig. 8.2k of the main text as a function of the depth, for three nanowire diameters D_w=40 nm, 50 nm and 60 nm. From this graph we can estimate that a variation of ±10 nm around the mean diameter of 50 nm assumed in the manuscript induces at most an error of ±5 nm in the estimation of the depth. Parameters: same as those in Fig. 8.2.

A8.3. Effect of the length of the nanowire in the estimation of the depth:

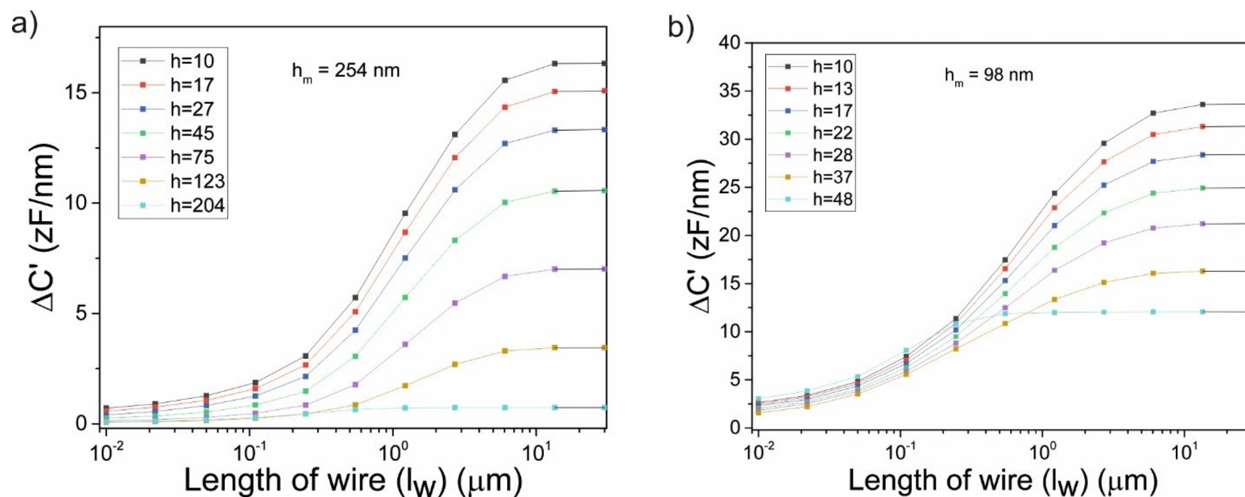

Figure A8.3 (a) Capacitance gradient contrast at the center of a buried nanowire for the tip at a distance z=36 nm from the surface of the gelatin film as a function of the length of the nanowire, for different depths, h. Parameters of the calculations: Same as for Fig. 8.2 of the main text. For lengths larger than l_W~8 mm (the one used in the main text) the results become independent from the length. If a nanowire is shorter, one can estimate the depth as indicated by the arrows in the graph. (b) Idem for the case of parameters corresponding to Fig 8.4 of the main text.

A8.4. Inclined vs non-inclined nanowire models:

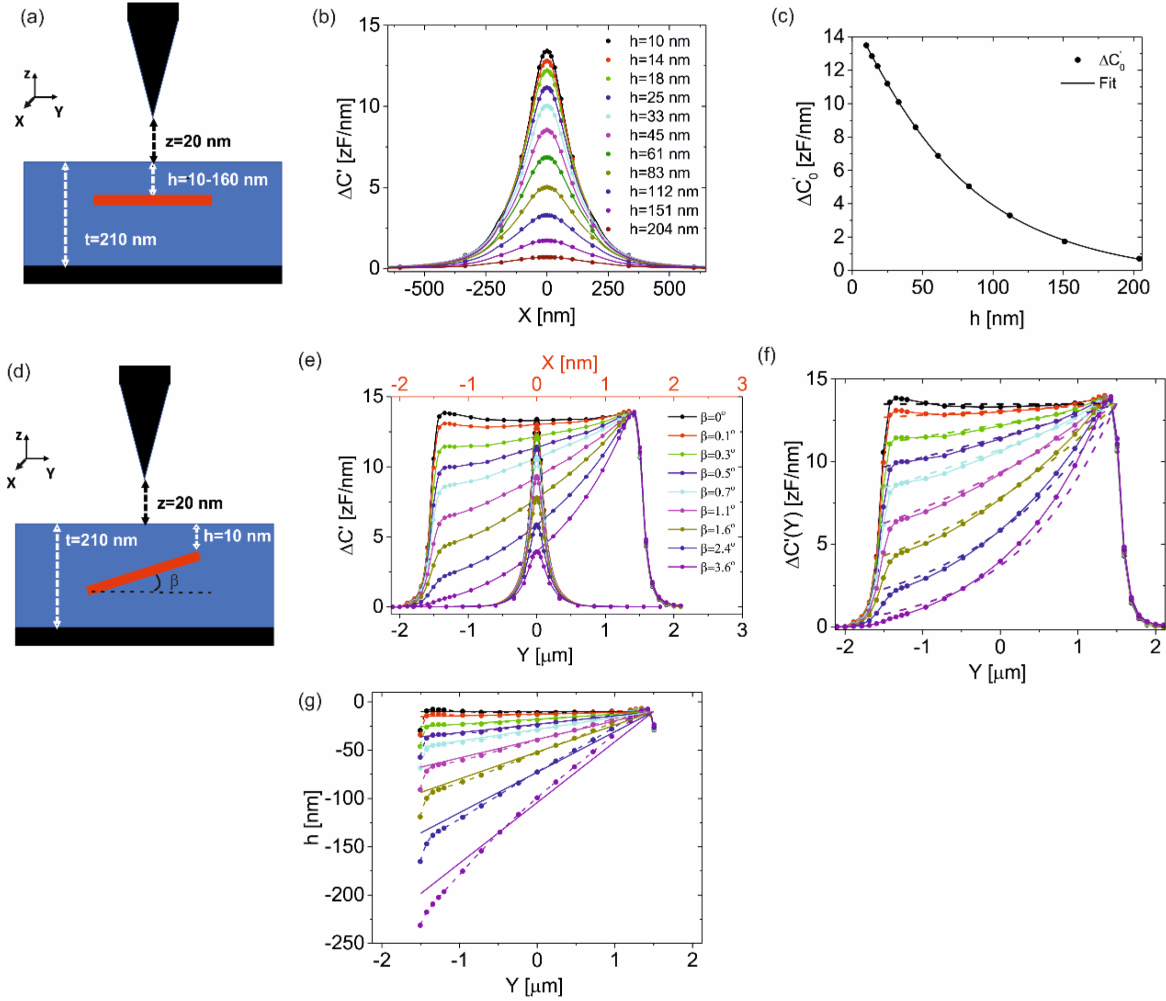

Figure A8.4 .(a) Schematic representation of a model of a buried nanowire parallel to the substrate (same model as the one used in the main text, without the bump). (b) Cross-section capacitance gradient contrast profiles along the transversal direction to the nanowire, ΔC'(X), for different depths. (c) (symbols) Capacitance gradient contrast at the center of the wire, $\Delta C'_0$, as a function of the depth. (continuous line) Least square fitting of the function $\Delta C'_0(h) = a(1+bh)/(1+ch+dh^2)$, with a=15.1 zF/nm, b=-3.7·10^{-3}nm^{-1}, c=7.1·10^{-3}nm^{-1}, d=7.0·10^{-5}nm^{-2}. (d) Schematic representation of a model of a buried nanowire inclined an angle b with respect to the substrate. (e) Capacitance gradient contrast profiles along the transversal, ΔC'(X), (black symbols, left and bottom axes) and longitudinal, ΔC'(Y), (red symbols, right and top axis) directions, respectively. (f) (continuous lines) Capacitance gradient contrast profile along the nanowire, ΔC'(Y), calculated by using the function $\Delta C'_0(h)$ and the depth profile of inclined nanowires, $h(Y) = h_0 + [(L_w/2)\cos(\beta) - Y]\tan(\beta)$. The symbols correspond to the numerically calculated profiles (same as in (e)). (g) (symbols) Local nanowire depths extracted with the function $\Delta C'_0(h)$ applied to the profiles of the inclined nanowires in (e), ΔC'(Y). The extracted depths nicely reproduce the actual nanowire depth profiles (continuous lines). This result demonstrates that the non-inclined nanowire model can be used to predict the

local depth of inclined nanowires, as we did in the manuscript. Parameters used in the calculations: D_w=50 nm, l_w=3 mm, ε_w=10^5 (metallic), h=10 nm, t_m=254 nm, ε_m=13.8, R=87 nm, θ=28º, H=12.5 mm, W=3 mm, L=3 mm.

A8.5. Photodiode and tip geometry calibration, and gelatin dielectric constant determination for Fig. 8.4:

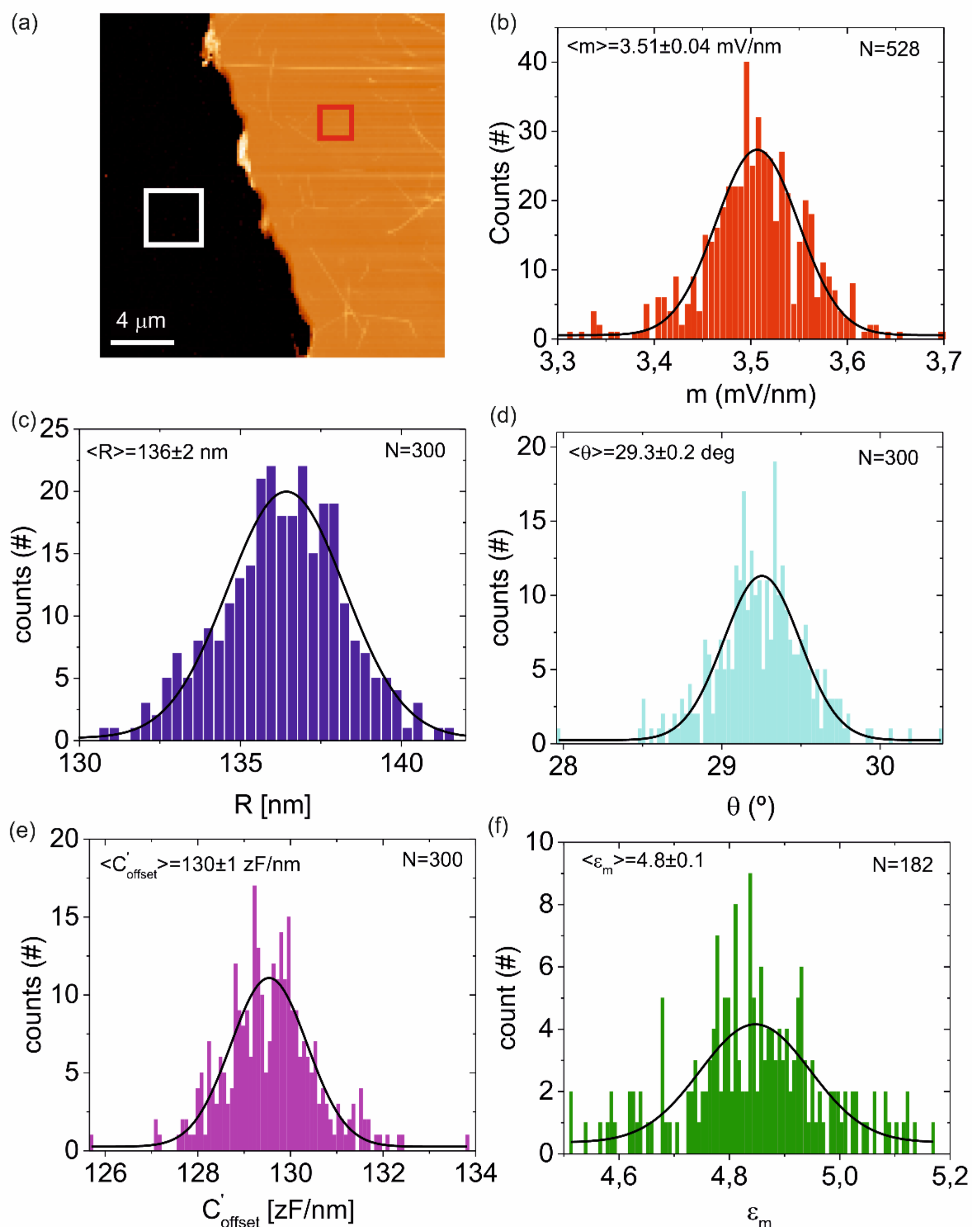

Figure A8.5 (a) AFM topographic image of a larger region corresponding to Fig. 8.4 of the main text. The white and red rectangles highlight the regions used to calibrate the photodiode sensitivity and tip geometry and to extract the dielectric constant of gelatin, respectively. (b) Distribution of the photodiode sensitivity extracted from the slope of the contact part of the normal deflection approach curves. The mean value (N=528) is 3.51±0.04 mV/nm. (c)-(e) Histogram of the tip radius, half cone angle and capacitance gradient offset obtained by fitting theoretical dC/dz

curves generated for a tip-on-metal model to the experimental dC/dz approach curves acquired in the white rectangle region in (a). The mean values (N=300) obtained are R=136±2 nm, θ=29.3±0.2º and C'_{offset}=130±1 zF/nm, respectively. (f) Histogram distribution of the values obtained for the dielectric constant of gelatin obtained by fitting theoretical dC/dz curves generated for a tip-on-thin dielectric film model to the experimental dC/dz approach curves acquired in red rectangle in (a). The mean value (N=300) obtained is ε_m=4.8±0.1

Chapter 9

Conclusions

The subsurface characterization of silver nanowire nanocomposites has been carried out with the help of Electrostatic Force Microscopy (EFM). The Scanning Dielectric Microscopy (SDM), pertaining from the combination of EFM and theoretical analysis, has provided us with the ability to analyze the complex subsurface features as seen in the past chapters. To summarize the efforts of this thesis,

Chapter 2 showed us the need for subsurface characterization in a wide range of fields to address the existing nanotomographical problems in various industries and also to ensure its development.

Chapter 3 outlined the family of Scanning Probe Microscopy (SPM) with special importance provided to AFM and EFM. This chapter showed the advantage of using SPM for subsurface characterization and its prior applications. Finally, this chapter also covered the advent of EFM in subsurface characterization, its merits, and its successful applications.

Chapter 4 discussed the importance of silver nanowire nanocomposites along with its applications in various fields. This chapter also discussed the present characterization methods and the need for subsurface characterization to understand and improve the performance of silver nanowire nanocomposites.

Chapter 5 dealt with the theoretical studies (numerical & analytical) and imbibe us with a basic understanding of the theoretical calculations. The number of unknown parameters present like the instrumental parameters (radius, half cone angle of the tip), experimental parameters (tip-sample distance) and the sample parameters (height and thickness, dielectric constant and chemical properties of the burying matrix and buried elements) were considered and investigated. These numerical analyses provided us the best parameter fit for the experimental analysis among the available numerous permutations and combinations. This analysis in turn saved us a lot of finite factors like time, money and resources consumed. The presence of these theoretical studies moving hand in hand with the experimental technique provided efficient information in subsurface characterization.

Chapter 6 showed us the experimental part of materials and methods in creating the subsurface characterization. Existing significant subsurface sample preparation methods from the literature have been analyzed. The analysis prompted spin coating as the best sample preparation method for the purposes of this thesis. Each parameter affecting the nanometric thickness of the nanocomposite sample including time of

coating, method of coating, temperature and subsequent drying have been optimized. These samples are further characterized with profilometer, AFM and SEM to ensure the required silver nanowire nanocomposite sample for subsurface characterization.

Chapter 7, adding to our analysis on chapter 5, have improved our understanding of the spatial resolution of buried nanowires in nanocomposites during the subsurface characterization by scanning dielectric microscopy thereby helping to interpret the obtained signal and image contrast accordingly. The parameters that influence the spatial resolution have been identified and analyzed enabling predicting the lateral resolution achievable in each situation.

Chapter 8 have shown experimentally that EFM could provide exclusive subsurface data that could not be observed from topographical methods. In particular, we were able to derive nanoscale depth distribution maps of silver nanowires in gelatin nanocomposites. Identifying the depth of the nanowires in the composites could provide with the option of three-dimensional reconstruction of the material. This significant advantage opens the door for far more application in different fields.

These thorough subsurface investigations carried out would make the efforts in this thesis an indispensable valuable part of the advancement of nanoscale tomography studies.

Chapter 10

Outlook and Future works

The future direction of this thesis research could greatly help in the understanding of the properties of nanocomposite materials. This technique could be modified and adapted to the nanoscale subsurface characterization of any industries that requires non-destructive nanotomography characterization with minimal improvements or modifications. For instance, the gelatin matrix used here could be extrapolated to many different matrices used in composites. The same could be said for the buried elements which are in this case silver nanowires, that could be changed into any different material nanowires or even different nanostructures to study similar parameters. In short, we could translate this technique across the spectrum as long as there is a difference between the permittivity of the burying matrix and the buried materials to provide the electrical contrast.

Transferring this technique to a pan-material matrix would also help in not only limiting the technique to the material science applications, but also extend it to biological and medical applications, food industry, packaging industry, electronics, and semiconductor industry etc., as we noted in Chapter 2.

For example, let us consider the nanotoxicology and drug delivery applications where determining the role of nanoparticle entry and its function inside the target cell is imperative in developing new-age drug designing systems (Fig. 9.1). As mentioned before, the advantage of using SPM for this characterization also includes that it could work under local cellular environment and the cells are not damaged as this is a non-destructive technique.

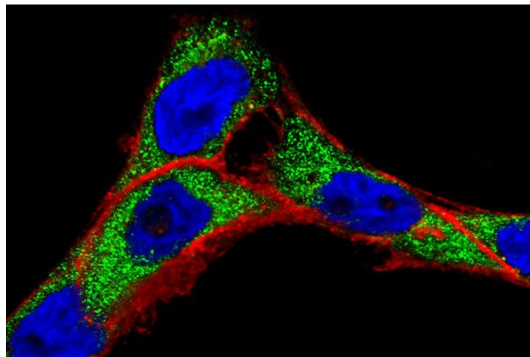

Figure 9.1. Fluorescent image of nanoparticles (shown here in green) and its interaction with the nucleus (blue) [Obtained from https://www.healthfoodis.com/2019/09/how-nanotechnology-can-be-used-to-diagnose-and-treat-cancer.html]

Additionally, it is also often claimed that the electrical properties of tumor cells are different from the electrical properties of normal cells. The tumor cells have the property of Enhanced Permeation and Retainability (EPR)[131] effect where the tissues in that microenvironment have more vascular permeability to the molecules than the normal tissues. This may cause a change in the dielectric nature of the tumor area[132–134], which could be tracked down to one of the differences between the tumor cell and the normal cell. One of the biggest challenges of treating patients affected with cancer is diagnosing the disease at later or more advanced stages. The typical reason being the tumor cells behave the same way the normal cells would, with the exception of apoptosis. This technique could be tested on the tumor cells or their microenvironment to find its cancerous properties even in the initial stages, which makes treating cancer relatively easier.

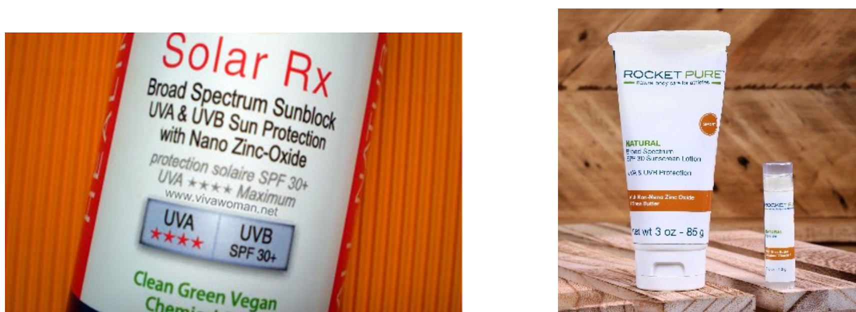

Figure 9.2. Cosmetic commercial products that contain nanoparticles in their soft gel matrices (More products at https://www.nanotechproject.tech/cpi/products/solar-rx-spf-30-nano-zinc-oxide-sunblock/)

In the last decade, the debate about the use of nanoparticles in cosmetic and food sciences have been discussed extensively about its nanotoxicological aspects[27,135–138]. For example, the sunscreen companies have claimed that adding nanoparticles would help in increasing the efficiency of the products (Fig 9.2). The claims have been that nanoparticles from the products could enter the dermis layer which could cause local toxicity. In contrast, it is also claimed that if the nanoparticle does not enter the uppermost pores in the skin, the nanoparticle maybe larger in size, in which case the particles does not have the functional advantage of the nanoparticle. This technique is a perfect fit for soft matrices or lipid and gel matrices as they require no sample preparation in contrast to the requirements of Electron Microscopy, where in many cases the properties of the matrix are altered before it is characterized.

These kind of nanotomography studies could help us understand the properties of both matrices and nanoparticles which helps in tuning and applying them simultaneously.

Abstract of the thesis

The ability to characterize the elements beneath the surface has been a dire necessity in the fields of materials science, polymer technology, biology, and medical sciences. Scanning Probe Microscopies are the family of microscopies that scans the surface using a nanometric probe and the acquired data is used to reconstruct the physical properties of the samples in nanometric resolution (e.g., topography). Since the measurements could be carried out in non-contact mode, the ability to study tomography have made them a better contender. SPM also possess the relative advantage of being non-invasive, non-destructive, requires relatively minimal sample preparation, can be extended into any environment (inert, ambient vacuum), and also be measured in air, water, or any biological medium. Among them, Electrostatic Force Microscopy, has been successfully used in subsurface investigations to study the compositional modifications below the organic layers, imaging below the organic layers, imaging water molecules in confined nanometric channels, imaging of carbon nanotubes, graphene networks and nanoparticles inside the polymeric nanocomposites.

Nanocomposites, which consist of nanostructures in their bulk matrix to improve the matrix efficiency, have been one of the successfully incorporated material science application of the last two decades. Silver nanoparticle especially have a barrage of applications to its credit ranging from solar cell applications, touch screens, LEDs to flexible wearable devices. Understanding the subsurface features or tomography of these nanocomposites could help us in understanding their properties, interpreting them based on their parametric dependence which would later aid us in tuning them for our desired applications.

In this thesis. Individual computational studies have been carried out of nanowires buried in a dielectric matrix to observe the effects of various parameters influencing the subsurface imaging. Spatial resolution is given prime importance as its behavior of two parallel nanowires is studied along with two nanowires overlapped one on top of each other. Also, the analysis of silver nanowire nanocomposites has been investigated with the help of Scanning Dielectric Force Volume Microscopy, a technique proposed recently with EFM. The bulk matrix is composed of gelatin which can offer a range of permittivities depending on the degree of hydration, for e.g., here $\varepsilon_r \sim 5$ to $\varepsilon_r \sim 14$. This sample is experimentally analyzed, imaged and the depth of nanowires in the matrix inside the bulk matrix is mapped with the theoretical analysis.

This thesis research provides us with subsurface information that would help us in understanding and tuning the parameters to achieve desired applications.

Chapter 11

11.1 Summary (Eng)

In various research fields ranging from material sciences, microelectronics to life sciences, there is an increasing need for nanoscale characterization techniques. Achieving detailed 3D maps of the structural properties of materials in a non-destructive and label-free technique is of dire necessity. For example, Nanocomposites, which consist of nanostructures in their bulk matrix to improve the matrix efficiency, have successfully incorporated into material science applications in the last two decades. Silver nanoparticle nanocomposites especially have a barrage of applications to their credit, ranging from solar cell applications, touch screens, and LEDs to flexible wearable devices. Understanding these nanocomposites' subsurface features or tomography could help us understand their properties, interpreting/analyzing them based on their parametric dependence, which would later aid us in tuning them for our desired applications.

The demand for nanoscale tomographic characterization has given rise to the development of different techniques and methods, mainly based on Electron, X-Ray and Optical Microscopies. Each of the techniques can provide us with the sub-surface information required, but all present certain limitations. For example, Electron Microscopy methods require extensive sample preparation, and so the sample is altered or destroyed in the characterization process. Fluorescence microscopy and two-photon microscopy require a fluorescence tag or two-photon dyes to be tagged/attached to identify the dispersed particles in the matrix/composites. For this reason, additional nanotomographic microscopy techniques are still being investigated. Among them, nanotomographic Scanning Probe Microscopy (SPM) techniques have emerged with a great potential in recent years.

Scanning Probe Microscopies is the family of microscopies that scans the surface using a nanometric probe. The acquired data is used to reconstruct the samples' physical properties in nanometric resolution. (e.g., topography). Since the measurements could be carried out in non-contact mode, studying tomography has made them a better contender. SPM also possess numerous advantages compared to the existing techniques like of being a) non-invasive, b) non-destructive, c) requiring relatively minimal sample preparation, d) can be extended into any environment (inert, ambient vacuum) and e) can also be measured in air, water, or any biological medium.

Among them, Electrostatic Force Microscopy is a technique where a voltage bias is applied between the probe and the sample, and the electric force felt by the tip is measured. When the probe/tip is moved

along the surface, the cantilever and probe deflect to the electrical properties of the localized point beneath them. This force exerted on the tip (or) the change in capacitive force is measured and recorded. This capacitive force is a long-range force, (i.e.) the force might not pertain only to the surface but also corresponds to the entities below the surface. This quality has been utilized to study the tomography (sub-surface characteristics), which has been successfully studied in recent investigations such as studying the compositional modifications below the organic layers, imaging below the organic layers, imaging of carbon nanotubes, graphene networks, nanoparticles inside the polymeric nanocomposites. Along with the qualitative analysis of EFM images, recent advances proved that nanotomography quantitative information could be obtained such as the depth of carbon nanotubes in polymeric films, the dielectric properties of buried water in nanochannels. In this study, the best parameters have been identified using numerical methods for experimental analysis.

In the continued efforts to this objective, we theoretically analyze the use of Scanning Dielectric Microscopy (SDM) to non-destructively investigate the nanocomposites. There is a particular focus on the attainable spatial resolution and the possibility to identify the capacitive coupling between neighboring nanowires. The preliminary study demonstrates that the nanowires spread function consists of a modified Lorentzian with a cubic decay. Following that, we have shown that the spatial resolution can be defined with the help of this function and noted how the different system parameters like tip-sample distance, the radius of the probe, depth of the nanowires influences it. We also found that nanowires with a diameter of 50 nm with a spatial resolution below 100 nm are easily achievable for shallowly buried nanowires. The spatial resolution increases when a system parameter decreases the maximum of the nanowire spread function or increases their widths. These results are tested with multiple nanowire numerical and theoretical calculations. These same calculations and procedures are used to demonstrate the sensitivity of the capacitive coupling between neighboring nanowires. This result is especially relevant for separations below the diameter of the nanowires. These findings are of utmost relevance since the electric interaction between nanowires largely determines nanowire nanocomposites' macroscopic electrical properties. Present results prove that that SDM could impact the development of novel materials for applications in fields such as wearable electronics, solar cell technologies, and photonics and can be a valuable non-destructive subsurface characterization technique for nanowire nanocomposites.

We also show that Scanning Dielectric Microscopy (SDM) can image the subsurface nanowires and also map the depth of the nanowires distribution within the nanocomposites non-destructively. To achieve it,

we incorporate the sub-surface imaging capabilities of Electrostatic Force Microscopy(EFM) along with its quantitative analysis with the help of finite element numerical calculations. To test them in an application, the three-dimensional spatial distribution of ~50 nm diameter silver nanowires in ~100 nm-250 nm thick gelatin films is determined. The advantage of using a gelatin matrix presents a relatively low dielectric constant, ε_r~5, as well as, in humid ambient conditions, where its dielectric constant rises up to ε_r ~14, and so characterization is done both in dry ambient conditions. The results show that SDM can optimize these materials' properties for applications in fields such as wearable electronics, solar cell technologies, or printable electronics and can be a valuable non-destructive subsurface characterization technique for nanowire-based nanocomposite materials.

Identifying the nanowires' depth in the composites could provide the option of three-dimensional reconstruction of the material, which opens the door for far more applications in different fields. We believe that the thorough subsurface investigations carried out in this thesis, would play an indispensable part in the advancement of nanoscale tomography studies.

11.2 Resumen (Esp)

En varios campos de investigación que van de los Materiales, y la Microelectrónica a las Ciencias de la Vida, existe un incremento de la necesidad de técnicas de caracterización capaces de proporcionar mapas detallados 3D de las propiedades estructurales de los materiales de una manera no destructiva y sin el uso de marcadores. En particular, las aplicaciones de ciencia de materiales de los nanocompuestos que están formados por nanoobjetos dentro de una matriz. Por ejemplo, los nanocompuestos formados por nanopartículas de plata, tienen un aluvión de aplicaciones que van desde aplicaciones de células solares, pantallas táctiles, LED hasta dispositivos portátiles flexibles. La cuantificación de las propiedades a nivel tomográfico de estos nanomateriales podría contribuir decisivamente al desarrollo de nuevos nanomateriales pioneros para aplicaciones en ciencias de la Salud y Electrónica.

La alta demanda de los estudio tomográficos ha dado lugar a diferentes tipos de microscopía, como el microscopio electrónico (ME) de transmisión (TEM por su sigla en inglés, o MET en español) o el microscopio electrónico de barrido (SEM), la microscopía de fluorescencia, la microscopía de dos fotones, etc.. Sin embargo, las técnicas tomográficas a nanoescala 3D existentes muestran limitaciones fundamentales respecto a su capacidad para mapear las propiedades físicas de los materiales (por ejemplo, mecánicas, eléctricas o magnéticas), que son relevantes en muchas áreas de la ciencia y la tecnología. Por ejemplo, la preparación de las muestras para ser utilizadas por las técnicas de microscopia electrónica requiere un proceso extenso y delicado, en el cual la muestra puede ser destruida. La microscopía de fluorescencia y la de dos fotones requieren una etiqueta de fluorescencia o dos tintes de fotones para etiquetar/adherir, y identificar las partículas enterradas en la matriz. Para hacer frente a estas limitaciones, se están desarrollando enfoques tomográficos a nanoescala alternativos. Una de las alternativas más prometedoras se basa en el uso de técnicas de microscopía de sonda de barrido (SPM)

Los microscopios de sonda de barrido son la familia de microscopios que exploran la superficie mediante una sonda nanométrica y los datos adquiridos se utilizan para reconstruir las propiedades físicas de las muestras en resolución nanométrica. (por ejemplo, topografía). Dado que las mediciones se pueden realizar sin contacto (sin tocar la muestra), potencia su capacidad de estudiar propiedades físicas a nivel subsuperficial, lo cual ha convertido a las técnicas de SPM en candidatas óptimas para los investigadores. Tambien, la preparación de las muestras para ser medidas por SPM no es complicada en comparación con las otras técnicas de microscopía, y puede extenderse a cualquier ambiente (inerte, vacío ambiental), así como medirse en aire, agua o cualquier medio biológico.

Entre ellos, la microscopía de fuerza electrostática, es una técnica en la que se aplica una polarización de voltaje entre la sonda y la muestra, por lo que se crea una capacitancia. Cuando la sonda/punta se mueve a lo largo de la superficie, el voladizo y la sonda se desvían hacia las propiedades eléctricas del punto localizado debajo de ellos. Esta fuerza ejercida sobre la punta o el cambio en la fuerza capacitiva se mide y cuantifica. Esta fuerza capacitiva es una fuerza de largo alcance, es decir la fuerza puede no pertenecer solo a la superficie, sino que también corresponde a las entidades debajo de la superficie. Esta cualidad se ha utilizado para estudiar la tomografía (propiedades del subsuelo) que se ha estudiado con éxito en las investigaciones recientes, como el estudio de las modificaciones de la composición debajo de las capas orgánicas, imágenes debajo de las capas orgánicas, imágenes de nanotubos de carbono, redes de grafeno, nanopartículas. dentro de los nanocompuestos poliméricos. Junto con el análisis cualitativo de imágenes EFM, avances recientes demostraron que se puede obtener información cuantitativa nanotomográfica, como la profundidad de los nanotubos de carbono en películas poliméricas, las propiedades dieléctricas del agua confinada en nanocanales. En este estudio se ha llevado a cabo la identificación de los parámetros óptimos mediante métodos numéricos para el análisis experimental.

En los capítulos preliminares, analizamos teóricamente el uso de la microscopía dieléctrica de barrido (SDM) para investigar de forma no destructiva un nanocompuesto formado por nanocables metálicos enterrados. Centrandonos en la resolución espacial y la posibilidad de identificar el acoplamiento capacitivo entre nanocables vecinos. El estudio principal es la demostración de que la función de dispersión de los nanocables consiste en un Lorentziano modificado con un decaimiento cúbico. A continuación, hemos demostrado que la resolución espacial se puede definir con la ayuda de esta función y hemos observado cómo los diferentes parámetros del sistema como la distancia de la muestra de la punta, el radio de la sonda y la profundidad de los nanocables influyen en ella. También encontramos que los nanocables con un diámetro de 50 nm y una resolución espacial por debajo de 100 nm son fácilmente alcanzables para nanocables enterrados poco profundos. La resolución espacial aumenta cuando un parámetro del sistema disminuye el máximo de la función de dispersión de nanocables o aumenta su ancho. Estos resultados se prueban con múltiples cálculos numéricos y teóricos utilizando el método de elementos. Estos mismos cálculos y procedimientos se utilizan para demostrar la sensibilidad de al acoplamiento capacitivo entre nanocables vecinos. Este resultado es especialmente relevante para separaciones por debajo del diámetro de los nanocables. Estos hallazgos son de suma relevancia ya que la interacción eléctrica entre nanocables determina en gran medida las propiedades eléctricas macroscópicas de los nanocompuestos de nanocables. Los resultados actuales demuestran que SDM podría tener un impacto en el desarrollo de nuevos materiales

para aplicaciones en campos como la electrónica portátil, las tecnologías de células solares y la fotónica, y puede ser una técnica valiosa de caracterización del subsuelo no destructiva para nanocompuestos de nanocables.

También mostramos que la microscopía dieléctrica de barrido (SDM) puede obtener imágenes de los nanocables del subsuelo y también mapear la profundidad de la distribución de los nanocables dentro de los nanocompuestos de forma no destructiva. Para lograrlo, incorporamos las capacidades de obtención de imágenes subterráneas de la Microscopía de Fuerza Electrostática (EFM) junto con su análisis cuantitativo con la ayuda de cálculos numéricos de elementos finitos. Para probarlos en una aplicación, se determina la distribución espacial tridimensional de nanocables de plata de ~ 50 nm de diámetro en películas de gelatina de ~ 100 nm-250 nm de espesor. La ventaja de usar una matriz de gelatina presenta una constante dieléctrica relativamente baja, $\varepsilon_r \sim 5$, así como, en condiciones ambientales húmedas, donde su constante dieléctrica se eleva hasta $\varepsilon_r \sim 14$ y por lo tanto la caracterización se realiza tanto en condiciones ambientales secas. Los resultados muestran que el SDM puede contribuir a optimizar las propiedades de estos materiales para aplicaciones en campos como la electrónica portátil, las tecnologías de células solares o la electrónica imprimible y puede ser una técnica valiosa de caracterización del subsuelo no destructiva para nanocompuestos basados en nanocables.

La identificación de la profundidad de los nanocables en los compuestos podría proporcionar la opción de reconstrucción tridimensional del material, lo que abre la puerta a muchas más aplicaciones en diferentes campos. Estos a través de las investigaciones del subsuelo realizadas harían de esta tesis una pieza valiosa indispensable para el avance de los estudios de tomografía a nanoescala.

Chapter 12

Appendix

12.1. List of publications and congress presentations

The list of publications and congress presentations from the work of this thesis and mentioned below:

Publications:

- **Harishankar Balakrishnan*,** Ruben Millan*, Marti Checa, Rene Fabregas, Laura Fumagalli and Gabriel Gomila, 'Depth Mapping of Silver Nanowires in Gelatin Nanocomposites by Scanning Dielectric Microscopy' *(submitted)*
- **Harishankar Balakrishnan*,** Rene Fabregas*, Ruben Millan, Laura Fumagalli and Gabriel Gomila, 'Spatial Resolution and Capacitive Coupling in Nanowire Nanocomposites Characterized by Scanning Dielectric Microscopy: A Numerical Analysis'. *(submitted)*

Congress Presentations:

- **Harishankar Balakrishnan**, Ruben Millan, Rene Fabregas, Gabriel Gomila (IBEC), Subsurface characterization of buried silver nanowires using Electrostatic Force Microscopy (EFM), Conference: XXI Annual Linz Winter Workshop (Linz, AUSTRIA). 01-04/02/2019.
- **Harishankar Balakrishnan**, Ruben Millan, Rene Fabregas, Gabriel Gomila (IBEC), Characterization of nanowire nanocomposites by sub-surface electrostatic force microscopy (EFM), Conference : Workshop on Advanced Scanning Probe Microscopies (SPM2.0-ITN) (Barcelona, SPAIN). 10-11/12/2020.

Poster Presentations:

- **Harishankar Balakrishnan**, Rene Fabregas, Gabriel Gomila, On the Spatial Resolution in Nanotomography Based on Scanning Dielectric Microscopy: A Numerical Analysis, 13th IBEC Symposium: Bioengineering for Future & Precision Medicine (Barcelona, SPAIN). 27- 28/10/2020.
- **Harishankar Balakrishnan**, Adrica Kyndiah, Marti Checa, Ruben Millan, Rene Fabregas, Gabriel Gomila, Subsurface characterization of buried nanowires in thin gelatin films by Electrostatic Force

Microscopy, 12th IBEC Symposium: Bioengineering for Active ageing (Barcelona, SPAIN). 17/07/2019.

- **Harishankar Balakrishnan**, Ruben Millan, Rene Fabregas, Gabriel Gomila, Subsurface characterization of buried silver nanowires using Electrostatic Force Microscopy (EFM), 11th IBEC Symposium: Bioengineering for Regenerative Therapies (Barcelona, SPAIN). 02/10/2018.

12.2. List of acronyms and abbreviations

AC/ac – Alternating current

AFM – Atomic Force Microscope

Ag - Silver

AgNW – Silver Nanowires

Au - Gold

AM – Amplitude Modulation

BEOL – Back end-of-line

CNTs – Carbon Nanotubes

DC/dc - Direct current

DC'(x) – Capacitance gradient contrast profile

DC'(0) – Maximum contrast of Dc'(x) profile

dC/dz – Capacitance gradient

DNA – Deoxyribonucleic acid

D_w – Diameter of the nanowire

EFM – Electrostatic Force Microscope

EM – Electron Microscopy

FM – Frequency Modulation

ε_r - Relative permittivity (or) Dielectric constant

ε_m - Relative permittivity (or) Dielectric constant of the matrix

ε_w - Relative permittivity (or) Dielectric constant of the nanowire

Gel – Gelatin

HOPG – Highly Oriented Pyrolytic Graphite

ICs – Integrated Circuits

IPA – Isopropanol

ITO – Indium Tin Oxide

KPFM – Kelvin Probe Force Microcopy

LED – Light-Emitting Diodes

l_w – Length of the nanowire

Lockin – Amphatec Lockin Amplifier

μm - Micrometers

NCs – Nanocomposites

nm - nanometers

NW – Nanowire

PI - Polyimide

PMMA – Poly (methyl methacrylate)

PS – Polystyrene

PVDF - Polyvinylidene flouride

R – Radius of the probe/tip

Si – Silicon

Si-doped - Highly doped Silicon substrate

SiO_2 – Silicon dioxide

SDM – Scanning Dielectric Microscope

SDFVM – Scanning Dielectric Force Volume Microscopy

SMM – Scanning Microwave Microscopy

SNOM –Near-field Scanning Optical Microscope

SNFUH - Scanning Near-Field Ultrasound holography

SEM – Scanning Electron Microscope

SPM – Scanning Probe Microscope

STM – Scanning Tunneling Microscope

Th/θ – Half-cone angle of the probe/tip

TEM – Transmission Electron Microscope

TiO_2 – Titanium Dioxide

w_0 - Full width at half maximum

w_1 - Full width at one-fifth of maximum

z – Tip-sample distance

zF – ZeptoFarad

2ω – 2nd Harmonic amplitude

2D – Two-dimensional

3D – Three-dimensional

Chapter 13

References

1. Killgore, J. P., Kelly, J. Y., Stafford, C. M., Fasolka, M. J. & Hurley, D. C. Quantitative subsurface contact resonance force microscopy of model polymer nanocomposites. *Nanotechnology* **22**, (2011).
2. Verbiest, G. J., Simon, J. N., Oosterkamp, T. H. & Rost, M. J. Erratum: Subsurface atomic force microscopy: Towards a quantitative understanding (Nanotechnology (2012) 23 (145704)). *Nanotechnology* **23**, (2012).
3. Tselev, A., Velmurugan, J., Ievlev, A. V, Kalinin, S. V & Kolmakov, A. Seeing through Walls at the Nanoscale: Microwave Microscopy of Enclosed Objects and Processes in Liquids. *ACS Nano* **10**, 3562–3570 (2016).
4. Yamanaka, K., Ogiso, H. & Kolosov, O. Ultrasonic force microscopy for nanometer resolution subsurface imaging. *Appl. Phys. Lett.* **64**, 178–180 (1994).
5. You, L., Ahn, J. J., Obeng, Y. S. & Kopanski, J. J. Subsurface imaging of metal lines embedded in a dielectric with a scanning microwave microscope. *J. Phys. D. Appl. Phys.* **49**, (2015).
6. Kopanski, J. J., You, L., Ahn, J.-J., Hitz, E. & Obeng, Y. S. (Invited) Scanning Probe Microscopes for Subsurface Imaging. *ECS Trans.* **61**, (2014).
7. Gramse, G. *et al.* Nanoscale imaging of mobile carriers and trapped charges in delta doped silicon p–n junctions. *Nat. Electron.* **3**, 531–538 (2020).
8. Soliman, M., Ding, Y. & Tetard, L. Nanoscale subsurface imaging. *J. Phys. Condens. Matter* **29**, (2017).
9. Kübel, C. *et al.* Recent advances in electron tomography: TEM and HAADF-STEM tomography for materials science and semiconductor applications. *Microsc. Microanal.* **11**, 378–400 (2005).
10. Midgley, P. A. & Weyland, M. 3D electron microscopy in the physical sciences: The development of Z-contrast and EFTEM tomography. *Ultramicroscopy* **96**, 413–431 (2003).
11. Möbus, G., Doole, R. C. & Inkson, B. J. Spectroscopic electron tomography. *Ultramicroscopy* **96**, 433–451 (2003).
12. Möbus, G. & Inkson, B. J. Nanoscale tomography in materials science. *Materials Today* **10**, (2007).
13. Dinelli, F., Assender, H. E., Takeda, N., Briggs, G. A. D. & Kolosov, O. V. Elastic mapping of heterogeneous

nanostructures with ultrasonic force microscopy (UFM). *Surf. Interface Anal.* **27**, 562–567 (1999).

14. Midgley, P. A. & Dunin-Borkowski, R. E. Electron tomography and holography in materials science. *Nat. Mater.* **8**, 271–280 (2009).

15. Cadena, M. J. *et al.* Sub-surface imaging of carbon nanotube-polymer composites using dynamic AFM methods. *Nanotechnology* **24**, (2013).

16. Thompson, H. T., Barroso-Bujans, F., Herrero, J. G., Reifenberger, R. & Raman, A. Subsurface imaging of carbon nanotube networks in polymers with DC-biased multifrequency dynamic atomic force microscopy. *Nanotechnology* **24**, (2013).

17. Zhao, M. *et al.* Subsurface characterization of carbon nanotubes in polymer composites via quantitative electric force microscopy. *Nanotechnology* **21**, (2010).

18. Diebold, A. C. Subsurface imaging with scanning ultrasound holography. *Science (80-.).* **310**, 61–62 (2005).

19. Roduit, C. *et al.* Stiffness tomography by atomic force microscopy. *Biophys. J.* **97**, 674–677 (2009).

20. Roduit, C. *et al.* Elastic membrane heterogeneity of living cells revealed by stiff nanoscale membrane domains. *Biophys. J.* **94**, 1521–1532 (2008).

21. Longo, G. *et al.* Force volume and stiffness tomography investigation on the dynamics of stiff material under bacterial membranes. *J. Mol. Recognit.* **25**, 278–284 (2012).

22. Berquand, A. *et al.* Atomic Force Microscopy Imaging of Living Cells. *Micros. Today* **18**, 8–14 (2010).

23. Shekhawat, G. S. & Dravid, V. P. Applied physics: Nanoscale imaging of buried structures via scanning near-field ultrasound holography. *Science (80-.).* **310**, 89–92 (2005).

24. Guerrero, C. R., Garcia, P. D. & Garcia, R. Subsurface Imaging of Cell Organelles by Force Microscopy. *ACS Nano* **13**, 9629–9637 (2019).

25. Tabatabaei, N. & Mandelis, A. Thermal-wave radar: A novel subsurface imaging modality with extended depth-resolution dynamic range. *Rev. Sci. Instrum.* **80**, (2009).

26. Tetard, L., Passian, A., Farahi, R. H. & Thundat, T. Atomic force microscopy of silica nanoparticles and carbon nanohorns in macrophages and red blood cells. *Ultramicroscopy* **110**, 586–591 (2010).

27. Sharma, S. *et al.* Fueling a hot debate on the application of TiO2 nanoparticles in sunscreen. *Materials (Basel).* **12**, (2019).

28. Binnig, G. & Rohrer, H. SCANNING TUNNELING MICROSCOPE. *Sci. Am.* **253**, (1985).

29. Binning, G., Quate, C. . & Gerber, C. Atomic Force Microscope. *Phys. Rev. Lett.* **56**, 930–934 (1986).

30. Asmatulu, R. & Khan, W. S. Characterization of electrospun nanofibers. *Synth. Appl. Electrospun Nanofibers* 257–281 (2019). doi:10.1016/b978-0-12-813914-1.00013-4

31. Dufrêne, Y. F. *et al.* Imaging modes of atomic force microscopy for application in molecular and cell biology. *Nature Nanotechnology* **12**, (2017).

32. Gomila, G., Toset, J. & Fumagalli, L. Nanoscale capacitance microscopy of thin dielectric films. *J. Appl. Phys.* **104**, (2008).

33. Fumagalli, L., Esteban-Ferrer, D., Cuervo, A., Carrascosa, J. L. & Gomila, G. Label-free identification of single dielectric nanoparticles and viruses with ultraweak polarization forces. *Nat. Mater.* **11**, 808–816 (2012).

34. Fumagalli, L., Gramse, G., Esteban-Ferrer, D., Edwards, M. A. & Gomila, G. Quantifying the dielectric constant of thick insulators using electrostatic force microscopy. *Appl. Phys. Lett.* **96**, 2008–2011 (2010).

35. Esteban-Ferrer, D., Edwards, M. A., Fumagalli, L., Juárez, A. & Gomila, G. Electric polarization properties of single bacteria measured with electrostatic force microscopy. *ACS Nano* **8**, 9843–9849 (2014).

36. Cherniavskaya, O., Chen, L., Weng, V., Yuditsky, L. & Brus, L. E. Quantitative noncontact electrostatic force imaging of nanocrystal polarizability. *J. Phys. Chem. B* **107**, 1525–1531 (2003).

37. Checa, M. *et al.* Mapping the dielectric constant of a single bacterial cell at the nanoscale with scanning dielectric force volume microscopy. *Nanoscale* **11**, 20809–20819 (2019).

38. Fabregas, R. & Gomila, G. Dielectric nanotomography based on electrostatic force microscopy: A numerical analysis. *J. Appl. Phys.* **127**, (2020).

39. Yamanaka, K. UFM observation of lattice defects in highly oriented pyrolytic graphite. *Thin Solid Films* **273**, 116–121 (1996).

40. Kay, N. D., Robinson, B. J., Fal'Ko, V. I., Novoselov, K. S. & Kolosov, O. V. Electromechanical sensing of substrate charge hidden under atomic 2D crystals. *Nano Lett.* **14**, 3400–3404 (2014).

41. McGuigan, A. P. *et al.* Measurement of debonding in cracked nanocomposite films by ultrasonic force microscopy. *Appl. Phys. Lett.* **80**, 1180–1182 (2002).

42. Shekhawat, G., Srivastava, A., Avasthy, S. & Dravid, V. Ultrasound holography for noninvasive imaging of buried defects and interfaces for advanced interconnect architectures. *Appl. Phys. Lett.* **95**, 2007–2010 (2009).

43. Tetard, L. *et al.* Imaging nanoparticles in cells by nanomechanical holography. *Nat. Nanotechnol.* **3**, 501–505 (2008).

44. Tetard, L. *et al.* Elastic phase response of silica nanoparticles buried in soft matter. *Appl. Phys. Lett.* **93**, (2008).

45. Kolosov, O. V. *et al.* Imaging the elastic nanostructure of ge islands by ultrasonic force microscopy. *Phys. Rev. Lett.* **81**, 1046–1049 (1998).

46. Yamanaka, K. Ultrasonic force microscopy. *MRS Bull.* **21**, 36–41 (1996).

47. Kolosov, O. & Yamanaka, K. Nonlinear detection of ultrasonic vibrations in an atomic force microscope. *Jpn. J. Appl. Phys.* **32**, L1095–L1098 (1993).

48. Dinelli, F. *et al.* Mapping surface elastic properties of stiff and compliant materials on the nanoscale using ultrasonic force microscopy. *Philos. Mag. A Phys. Condens. Matter, Struct. Defects Mech. Prop.* **80**, 2299–2323 (2000).

49. Dinelli, F., Briggs, G., Kolosov, O. & Biswas, S. Measurements of stiff-material compliance on the nanoscale using ultrasonic force microscopy. *Phys. Rev. B - Condens. Matter Mater. Phys.* **61**, 13995–14006 (2000).

50. Cuberes, M. T., Assender, H. E., Briggs, G. A. D. & Kolosov, O. V. Heterodyne force microscopy of PMMA / rubber nanocomposites : nanomapping of viscoelastic. *J. Phys.D Appl. Phys.* **33**, 2347–2355 (2000).

51. Taubner, T., Keilmann, F. & Hillenbrand, R. Nanoscale-resolved subsurface imaging by scattering-type near-field optical microscopy. *Opt. Express* **13**, 8893 (2005).

52. Perrino, A. P., Ryu, Y. K., Amo, C. A., Morales, M. P. & Garcia, R. Subsurface imaging of silicon nanowire circuits and iron oxide nanoparticles with sub-10 nm spatial resolution. *Nanotechnology* **27**, (2016).

53. Dietz, C. *et al.* Nanotomography with enhanced resolution using bimodal atomic force microscopy. *Appl. Phys. Lett.* **92**, 2006–2009 (2008).

54. Ebeling, D., Eslami, B. & Solares, S. D. J. Visualizing the subsurface of soft matter: Simultaneous topographical imaging, depth modulation, and compositional mapping with triple frequency atomic force microscopy. *ACS Nano* **7**, 10387–10396 (2013).

55. Tetard, L., Passian, A. & Thundat, T. New modes for subsurface atomic force microscopy through nanomechanical coupling. *Nat. Nanotechnol.* **5**, 105–109 (2010).

56. Vitry, P. *et al.* Mode-synthesizing atomic force microscopy for volume characterization of mixed metal nanoparticles. *J. Microsc.* **263**, 307–311 (2016).

57. Vitry, P. *et al.* Mode-synthesizing atomic force microscopy for 3D reconstruction of embedded low-density dielectric nanostructures. *Nano Res.* **8**, 2199–2205 (2015).

58. Vitry, P. *et al.* Advances in quantitative nanoscale subsurface imaging by mode-synthesizing atomic force microscopy. *Appl. Phys. Lett.* **105**, (2014).

59. Optasanu, V. *et al.* High-resolution characterization of the diffusion of light chemical elements in metallic components by scanning microwave microscopy. *Nanoscale* **6**, 14932–14938 (2014).

60. Plassard, C. *et al.* Detection of defects buried in metallic samples by scanning microwave microscopy. *Phys. Rev. B - Condens. Matter Mater. Phys.* **83**, 2–5 (2011).

61. Biagi, M. C. *et al.* Nanoscale electric permittivity of single bacterial cells at gigahertz frequencies by scanning microwave microscopy. *ACS Nano* **10**, 280–288 (2016).

62. Jespersen, T. S. & Nygard, J. Mapping of individual carbon nanotubes in polymer/nanotube composites using electrostatic force microscopy. *Appl. Phys. Lett.* **90**, 58–61 (2007).

63. Castañeda-Uribe, O. A., Reifenberger, R., Raman, A. & Avila, A. Depth-sensitive subsurface imaging of polymer nanocomposites using second harmonic Kelvin probe force microscopy. *ACS Nano* **9**, 2938–2947 (2015).

64. Alekseev, A. *et al.* Local organization of graphene network inside graphene/polymer composites. *Adv. Funct. Mater.* **22**, 1311–1318 (2012).

65. Patel, S. *et al.* Imaging latex-carbon nanotube composites by subsurface electrostatic force microscopy. *Nanotechnology* **27**, (2016).

66. Peng, S. *et al.* Local Dielectric Property Detection of the Interface between Nanoparticle and Polymer in Nanocomposite Dielectrics. *Sci. Rep.* **6**, 1–9 (2016).

67. Cadena, M. J., Reifenberger, R. G. & Raman, A. High resolution subsurface imaging using resonance-enhanced detection in 2nd-harmonic KPFM. *Nanotechnology* **29**, (2018).

68. Van Der Hofstadt, M. *et al.* Internal Hydration Properties of Single Bacterial Endospores Probed by Electrostatic Force Microscopy. *ACS Nano* **10**, 11327–11336 (2016).

69. Fumagalli, L. *et al.* Anomalously low dielectric constant of confined water. *Science (80-.).* **360**, 1339–1342 (2018).

70. Cuervo, A. *et al.* Direct measurement of the dielectric polarization properties of DNA. *Proc. Natl. Acad. Sci. U. S. A.* **111**, (2014).

71. Dols-Perez, A., Gramse, G., Calò, A., Gomila, G. & Fumagalli, L. Nanoscale electric polarizability of ultrathin biolayers on insulating substrates by electrostatic force microscopy. *Nanoscale* **7**, 18327–18336 (2015).

72. Fumagalli, L., Ferrari, G., Sampietro, M. & Gomila, G. Quantitative nanoscale dielectric microscopy of single-layer supported biomembranes. *Nano Lett.* **9**, 1604–1608 (2009).

73. Fumagalli, L., Ferrari, G., Sampietro, M. & Gomila, G. Dielectric-constant measurement of thin insulating films at low frequency by nanoscale capacitance microscopy. *Appl. Phys. Lett.* **91**, (2007).

74. Gomila, G., Esteban-Ferrer, D. & Fumagalli, L. Quantification of the dielectric constant of single non-spherical nanoparticles from polarization forces: Eccentricity effects. *Nanotechnology* **24**, (2013).

75. Gomila, G., Gramse, G. & Fumagalli, L. Finite-size effects and analytical modeling of electrostatic force microscopy applied to dielectric films. *Nanotechnology* **25**, (2014).

76. Gramse, G., Gomila, G. & Fumagalli, L. Quantifying the dielectric constant of thick insulators by electrostatic force microscopy: Effects of the microscopic parts of the probe. *Nanotechnology* **23**, (2012).

77. Fumagalli, L., Edwards, M. A. & Gomila, G. Quantitative electrostatic force microscopy with sharp silicon tips. *Nanotechnology* **25**, (2014).

78. Lozano, H., Millán-Solsona, R., Fabregas, R. & Gomila, G. Sizing single nanoscale objects from polarization forces. *Sci. Rep.* **9**, 1–12 (2019).

79. Din, S. H. Nano-Composites and their Applications: A review. *Charact. Appl. Nanomater.* **2**, 1–9 (2019).

80. White, S. I. *et al.* Electrical percolation behavior in silver nanowire-polystyrene composites: Simulation and experiment. *Adv. Funct. Mater.* **20**, 2709–2716 (2010).

81. Cui, Z., Poblete, F. R. & Zhu, Y. Tailoring the Temperature Coefficient of Resistance of Silver Nanowire Nanocomposites and their Application as Stretchable Temperature Sensors. *ACS Appl. Mater. Interfaces* **11**, 17836–17842 (2019).

82. Liang, X., Zhao, T., Hu, Y. & Sun, R. Dielectric properties of silver nanowires-filled polyvinylidene fluoride composite with low percolation threshold. *J. Nanoparticle Res.* **16**, (2014).

83. Mi, H. Y., Li, Z., Turng, L. S., Sun, Y. & Gong, S. Silver nanowire/thermoplastic polyurethane elastomer nanocomposites: Thermal, mechanical, and dielectric properties. *Mater. Des.* **56**, 398–404 (2014).

84. Wikander, K. *et al.* Incorporation of platinum nanoparticles in ordered mesoporous carbon. *J. Colloid Interface Sci.* **305**, 204–208 (2007).

85. Zhang, Y. X. *et al.* Synergetic Transparent Electrode Architecture for Efficient Non-Fullerene Flexible Organic Solar Cells with >12% Efficiency. *ACS Nano* **13**, 4686–4694 (2019).

86. Guan, T. *et al.* Self-supported ultrathin NiCo-LDH nanosheet array/Ag nanowire binder-free composite electrode for high-performance supercapacitor. *J. Alloys Compd.* **799**, 521–528 (2019).

87. Shin, Y. Bin *et al.* Modified Inverted Layer Processing of Ultrathin Touch Sensor Impregnating Ag Nanowires with Both Enlarged Surface Coverage of Conductive Pathways and Ultralow Roughness. *Electron. Mater. Lett.* **16**, 247–254 (2020).

88. Choi, J. H., Shin, M. G., Jung, Y., Kim, D. H. & Ko, J. S. Fabrication and performance evaluation of highly sensitive flexible strain sensors with aligned silver nanowires. *Micromachines* **11**, (2020).

89. Abbas, S. & Kim, J. All-metal oxide transparent photodetector for broad responses. *Sensors Actuators, A Phys.* **303**, 111835 (2020).

90. Kumar, A., Karadan, P. & Barshilia, H. C. Synthesis of silver nanowires towards the development the ultrasensitive AgNWs/SiNPLs hybrid photodetector and flexible transparent conductor. *Mater. Sci. Semicond. Process.* **75**, 239–246 (2018).

91. Kim, B. S., Kim, M. K., Jo, D. S., Chae, H. & Cho, S. M. Optimal Structure of Color-Conversion Layer for White Organic Light-Emitting Diode on Silver-Nanowire Anode. *ECS J. Solid State Sci. Technol.* **7**, R3176–R3181 (2018).

92. Lee, Y. *et al.* Conjugated polyelectrolyte-assisted vacuum-free transfer-printing of silver nanowire network for top electrode of polymer light-emitting diodes. *Org. Electron.* **43**, 64–69 (2017).

93. Wu, J., Yang, J., Yang, X. & Ding, X. Low-voltage Hf-ZnO thin film transistors with Ag nanowires gate electrode and their application in logic circuit. *IEEE J. Electron Devices Soc.* **8**, 152–156 (2020).

94. Liang, C., Ruan, K., Zhang, Y. & Gu, J. Multifunctional Flexible Electromagnetic Interference Shielding Silver Nanowires/Cellulose Films with Excellent Thermal Management and Joule Heating Performances. *ACS Appl. Mater. Interfaces* **12**, 18023–18031 (2020).

95. Peng, H. *et al.* High-performance and ultraflexible PEDOT/silver nanowires/graphene films for electrochromic applications. *Opt. Lett.* **45**, (2020).

96. Yang, H. *et al.* Facile fabrication of large-scale silver nanowire-PEDOT:PSS composite flexible transparent electrodes for flexible touch panels. *Mater. Res. Express* **6**, (2019).

97. Wang, J. *et al.* A highly sensitive and flexible pressure sensor with electrodes and elastomeric interlayer

containing silver nanowires. *Nanoscale* **7**, 2926–2932 (2015).

98. Langley, D. *et al.* Flexible transparent conductive materials based on silver nanowire networks: A review. *Nanotechnology* **24**, (2013).

99. Li, W. *et al.* Recent progress in silver nanowire networks for flexible organic electronics. *J. Mater. Chem. C* **8**, 4636–4674 (2020).

100. Zhang, R. & Engholm, M. Recent progress on the fabrication and properties of silver nanowire-based transparent electrodes. *Nanomaterials* **8**, 1–17 (2018).

101. Yu, Z., Li, L., Zhang, Q., Hu, W. & Pei, Q. Silver nanowire-polymer composite electrodes for efficient polymer solar cells. *Adv. Mater.* **23**, 4453–4457 (2011).

102. Jing, X., Wang, X. Y., Mi, H. Y. & Turng, L. S. Stretchable gelatin/silver nanowires composite hydrogels for detecting human motion. *Mater. Lett.* **237**, 53–56 (2019).

103. Zeng, X. Y., Zhang, Q. K., Yu, R. M. & Lu, C. Z. A new transparent conductor: Silver nanowire film buried at the surface of a transparent polymer. *Adv. Mater.* **22**, 4484–4488 (2010).

104. Gaynor, W., Lee, J. Y. & Peumans, P. Fully solution-processed inverted polymer solar cells with laminated nanowire electrodes. *ACS Nano* **4**, 30–34 (2010).

105. Nair, N. M. *et al.* Printable Silver Nanowire and PEDOT:PSS Nanocomposite Ink for Flexible Transparent Conducting Applications. *ACS Appl. Electron. Mater.* **2**, 1000–1010 (2020).

106. Wu, X., Zhou, Z., Wang, Y. & Li, J. Syntheses of silver nanowires ink and printable flexible transparent conductive film: A review. *Coatings* **10**, (2020).

107. De, S. *et al.* Silver nanowire networks as flexible, transparent, conducting films: Extremely high DC to optical conductivity ratios. *ACS Nano* **3**, 1767–1774 (2009).

108. Lee, J. Y., Connor, S. T., Cui, Y. & Peumans, P. Solution-processed metal nanowire mesh transparent electrodes. *Nano Lett.* **8**, 689–692 (2008).

109. Azulai, D., Belenkova, T., Gilon, H., Barkay, Z. & Markovich, G. Transparent metal nanowire thin films prepared in mesostructured templates. *Nano Lett.* **9**, 4246–4249 (2009).

110. Kumar, A. & Zhou, C. The race to replace tin-doped indium oxide: Which material will win? *ACS Nano* **4**, 11–14 (2010).

111. Esteban, D. Electric polarization properties of single bacteria measured with electrostatic force microscopy:

Theoretical and practical studies of Dielectric. 0–3 (2014).

112. Crowley, J. Simple Expressions for Force and Capacitance for a Conductive Sphere near a Conductive Wall. *Proc. Electrochem. Soc. Am. Annu. Meet. Electrost.* Paper D1, pp 1–15 (2008).

113. Smythe, W. R. *Static and dynamic electricity*. (McGraw-Hill, 1950).

114. Lozano, H. *et al.* Dielectric constant of flagellin proteins measured by scanning dielectric microscopy. *Nanoscale* **10**, 19188–19194 (2018).

115. Govyadinov, A. A. *et al.* Recovery of permittivity and depth from near-field data as a step toward infrared nanotomography. *ACS Nano* **8**, 6911–6921 (2014).

116. Gramse, G. *et al.* Nondestructive imaging of atomically thin nanostructures buried in silicon. *Sci. Adv.* **3**, 1–9 (2017).

117. Spitzner, E. C., Riesch, C. & Magerle, C. Subsurface imaging of soft polymeric materials with nanoscale resolution. *ACS Nano* **5**, 315–320 (2011).

118. Yang, Y. *et al.* Batch-fabricated cantilever probes with electrical shielding for nanoscale dielectric and conductivity imaging. *J. Micromechanics Microengineering* **22**, (2012).

119. Takano, H., Wong, S. S., Harnisch, J. A. & Porter, M. D. Mapping the subsurface composition of organic films by electric force microscopy. *Langmuir* **16**, 5231–5233 (2000).

120. Takano, H. & Porter, M. D. Monitoring chemical transformations at buried organic interfaces by electric force microscopy [3]. *J. Am. Chem. Soc.* **123**, 8412–8413 (2001).

121. Gramse, G. *et al.* Quantitative sub-surface and non-contact imaging using scanning microwave microscopy. *Nanotechnology* **26**, (2015).

122. Fraga, A. N. & Williams, R. J. J. Thermal properties of gelatin films. *Polymer (Guildf).* **26**, 113–118 (1985).

123. Withers, P. J. X-ray nanotomography. *Mater. Today* **10**, 26–34 (2007).

124. Englisch, S. *et al.* Mechanical Failure of Transparent Flexible Silver Nanowire Networks for Solar Cells using 3D X-Ray Nano Tomography and Electron Microscopy. *Microsc. Microanal.* **24**, 558–559 (2018).

125. Angeloni, L., Reggente, M., Passeri, D., Natali, M. & Rossi, M. Identification of nanoparticles and nanosystems in biological matrices with scanning probe microscopy. *Wiley Interdiscip. Rev. Nanomedicine Nanobiotechnology* **10**, 1–18 (2018).

126. Riedel, C. *et al.* On the use of electrostatic force microscopy as a quantitative subsurface characterization

technique: A numerical study. *Appl. Phys. Lett.* **99**, (2011).

127. Arinero, R., Riedel, C. & Guasch, C. Numerical simulations of electrostatic interactions between an atomic force microscopy tip and a dielectric sample in presence of buried nano-particles. *J. Appl. Phys.* **112**, (2012).

128. Kalinin, S. V., Bonnell, D. A., Freitag, M. & Johnson, A. T. Carbon nanotubes as a tip calibration standard for electrostatic scanning probe microscopies. *Appl. Phys. Lett.* **81**, 754–756 (2002).

129. Shapardanis, S., Hudpeth, M. & Kaya, T. Gelatin as a new humidity sensing material: Characterization and limitations. *AIP Adv.* **4**, (2014).

130. Van Der Hofstadt, M., Fabregas, R., Biagi, M. C., Fumagalli, L. & Gomila, G. Nanoscale dielectric microscopy of non-planar samples by lift-mode electrostatic force microscopy. *Nanotechnology* **27**, 1–13 (2016).

131. Kalyane, D. *et al.* Employment of enhanced permeability and retention effect (EPR): Nanoparticle-based precision tools for targeting of therapeutic and diagnostic agent in cancer. *Mater. Sci. Eng. C* **98**, 1252–1276 (2019).

132. Hussein, M. *et al.* Breast cancer cells exhibits specific dielectric signature in vitro using the open-ended coaxial probe technique from 200 MHz to 13.6 GHz. *Sci. Rep.* **9**, 1–8 (2019).

133. Zhao, Y. *et al.* Single-Cell Electrical Phenotyping Enabling the Classification of Mouse Tumor Samples. *Sci. Rep.* **6**, 1–8 (2016).

134. Wang, K. *et al.* Specific membrane capacitance, cytoplasm conductivity and instantaneous Young's modulus of single tumour cells. *Sci. Data* **4**, 1–8 (2017).

135. Shen, C., Turney, T. W., Piva, T. J., Feltis, B. N. & Wright, P. F. A. Comparison of UVA-induced ROS and sunscreen nanoparticle-generated ROS in human immune cells. *Photochem. Photobiol. Sci.* **13**, 781–788 (2014).

136. Catalano, R. *et al.* Safety evaluation of TiO2 nanoparticle-based sunscreen UV filters on the development and the immunological state of the sea urchin paracentrotus lividus. *Nanomaterials* **10**, 1–15 (2020).

137. Cross, S. E. *et al.* Human skin penetration of sunscreen nanoparticles: In-vitro assessment of a novel micronized zinc oxide formulation. *Skin Pharmacol. Physiol.* **20**, 148–154 (2007).

138. Yamada, M., Mohammed, Y. & Prow, T. W. Advances and controversies in studying sunscreen delivery and toxicity. *Adv. Drug Deliv. Rev.* **153**, 72–86 (2020).